Magnetotransport in quantum Hall systems at high Landau levels

A THESIS
SUBMITTED TO THE FACULTY OF THE GRADUATE SCHOOL
OF THE UNIVERSITY OF MINNESOTA
BY

Qianhui Shi

IN PARTIAL FULFILLMENT OF THE REQUIREMENTS
FOR THE DEGREE OF
Doctor of Philosophy

Advisor: Michael Zudov

Oct, 2017

Acknowledgements

I would like to express my sincere gratitude to, among other people,

- My PhD advisor Michael Zudov, for the training to effectively conducting experiments with "keep thinking and keep moving", for giving me the freedom and challenge to find out what to do, sharing the excitements and confusions, and providing me the opportunities of conference/research travels to interesting places meeting interesting people around the world.

- The team of Loren Pfeiffer from Princeton University and of Mike Manfra from Purdue University for providing the high quality samples. Those little pieces have brought to me lots of surprises, excitements, confusions and maybe a little bit of new knowledge as written in this thesis. I would also like to thank Vladimir Umansky from Weizmann Institute of Science and Maksym Myronov from University of Warwick although the results from the samples are not presented in this thesis.

- Boris Shklovskii for always being a source of insight and encouragement; for explaining to me on many subjects mentioned in this thesis (on many of which he did the original work) in class and his office, for his influence on me to understand and explain physics in simple pictures and words, and for his efforts to keep me on the right track in my career.

- The other two committee members, Paul Crowell and Bharat Jalan for valuable comments on my work.

- Jurgen Smet and his group, especially Joe Falson, Benedikt Friess, Johannes Geurs and Gunther Euchner, for hosting me in the Max-Planck Institute and helping with the experiments. Conducting experiments there was an enjoyable experience.

- Staff in the NHMFL, especially Hongwoo Baek, Scott Hannas, Glover Jones, Tim Murphy, Ju-huyn Park and Dmitry Smirnov, for technical assistance. Thanks also go to Lloyd Engel, for numerous comments on our fresh data, and lending hand to us when needed.

- Maxim Khodas and Ivan Dmitriev for teaching me about non-equilibrium transport.

- Many senior and junior colleagues in the quantum Hall community, for discussions on physics, advices and encouragements, and setting great role models.

- Yilikal Ayino and Vlad Pribiag for giving me the opportunity to do measurements in their lab and all the help during the experiments.

- People who have shared the same lab with me - Peter Martin and Quentin Ebner, for getting me started in the lab; Austin Riedl, for expert help on Labview; Xiaojun Fu, for testing my knowledge by tossing thousands of questions on me and carrying on the work.

- My parents for everything they give that leads me here, for support and patience, trusting my decisions and bearing my absence.

- My husband and best friend Sheng Tian for accompanying my PhD years, being full of magic and bringing me day-to-day happiness.

Dedication

To everyone who hopes this thesis to be of a little bit use

Abstract

Ever since the discovery of integer quantum Hall (QH) state by von Klitzing in 1980 [1], a two-dimensional electron gas (2DEG) subject to a perpendicular magnetic field has been a major playground of condensed matter physics, generating both exotic phases and intriguing concepts. In the quantum limit, or the lowest Landau level (LL), the most famous example is the fractional QH state, an incompressible quantum liquid manifesting quasiparticles of fractional charge [2, 3].

In this thesis, we present experimental magnetotransport studies in the high LL regime, exploiting state-of-art GaAs 2DEGs. For LL index $N \geq 2$, instead of the fractional QH states, the ground state is replaced by charge density waves (CDW) - stripe and bubble phases [4, 5, 6, 7]. At very high LLs where the energy scales are comparable between cyclotron gap and disorder and radiation frequency, a distinct class of non-equilibrium oscillations [8] emerge when the system is driven by microwaves [9, 10].

In the first part of the thesis we provide a general introduction to the fundamentals of the magnetotransport of quantum Hall system, focusing on high Landau levels. In chapter 1, we discuss the vehicle of choice for our experiments, which is a GaAs 2DEG. We discuss how a clean 2DEG is achieved, what the residue disorders are, and the attempt to characterize the "quality" of a 2DEG. The development of the field of quantum Hall systems has been largely driven by experiments, especially on magnetotransport. Nevertheless, rather than going by the experimental phenomena, here we take a approach which separates the problem into two layers. In chapter 2, we discuss the ingredients in the problem, and focus on the question: what is the ground state of the 2DEG in the presence of the magnetic field? In chapter 3, we focus on the magnetotransport properties of a 2DEG in different phases.

The second part of the thesis is devoted to experiments on the stripe and bubble phases. In chapter 4, we present a detailed study of the stripe orientation under in-plane magnetic fields $B_{\|}$ [11, 12]. We establish a rich phase diagram demonstrating that the stripe orientation under $B_{\|}$ is sensitive to a number of parameters, including the spin and LL index, partial filling factor ν^*, and the magnitude of $B_{\|}$ [13, 14, 15]. Our findings highlight that the stripe orientation is a robust reflection of the electron-electron interactions especially screening properties in the high LL regime, and shed new light on the longstanding mystery

of native stripe orientation. In chapter 5, we show that the stripes can be prepared into a metastable orientation [16] and study the relaxation process from one orientation to another. We find sharp jumps of resistance in the relaxation process, similar to the Barkhausen noise in magnetic systems while of much larger amplitudes, as well as telegraph noise, in our macroscopic samples. Our results reveal unambiguously the existence of domain structures in the stripe phase, and suggests large correlation length of the stripe phase. Chapter 6 presents the study of the effect of alloy disorder in stripe and bubble phases. We find that with increasing alloy disorder concentration, the resistance anisotropy in the stripe phase decreases, and stripes decay faster as one moves to high LLs. On the other hand, the melting temperature of stripes and the $B_{\parallel}$-induced reorientation of stripes, has very weak dependence on the concentration of alloy disorder, suggesting that these processes are dominated by the alignment of stripe domains (rather than local stripe order), which is insensitive to alloy disorder. We also find that the addition of alloy disorder stabilizes the bubble phases.

The third part consists of experiments under microwave radiations at very high LLs. In chapter 7 we present the discover of fine structure in microwave-induced resistance oscillations (MIRO) [17]. The fine structures manifest the peculiar feature that the resistance oscillations as a function of the magnetic field have the extrema (in B) not only decided by the radiation frequency, but also the power. We identify the origin of the fine structures as due to multi-photon assisted scatterings with sharp disorder. In chapter 8 [18] we present the detection of magneto-plasmons (MP) extending to order $n = 25$, in the Shubnikov-de Haas oscillation (SdHO) regime. The observed MP modes demonstrate alternating behavior at even and odd order, as well as retardation effects due to light-electron interactions at low orders . Our experiments demonstrate the technique exploiting SdHO as a surprisingly sensitive and elegant means to detect and investigate high-order MP modes.

Contents

List of Tables

List of Figures

Part I

Fundamentals

Chapter 1

Two-dimensional electron systems

1.1 Realizing a clean 2DEG

Starting with Si MOSFET (metal-oxide-semiconductor field-effect-transistor)[1, 19] and now seeing continuous excitement in exfoliated Van der Waals materials such as graphene [20, 21], 2DEGs have been realized in various forms. The most clean system which has been the superior playground for exploring various exotic phases so far, has been a thin layer of GaAs sandwiched by AlGaAs. The GaAs has a smaller band gap and lower conduction band energy than the AlGaAs, therefore, it serves as a quantum well. The possibility to realize a clean 2DEG in this system, in the first place, is based on the nearly identical lattice constant of the two materials and the precise layer control and high purity provided by molecular beam epitaxy (MBE) growth. The mobile carriers in the GaAs channel, are provided by Si doping. To minimize the effect of ionized donors on the carriers, an important method called "modulation doping" was developed, namely, the Si donors are incorporated in AlGaAs, separated from the 2DEG by a spacer of thickness d. The electrons migrate to the GaAs channel because of its low conduction band energy, and experience a weak scattering potential from the ionized donors.

To achieve the cleanest 2DEG with the least scattering events with disorder, the quantum well width w, spacer thickness d and the doping scheme are optimized. At the same time, in most cases, the Fermi level E_F of the 2DEG needs to be lower than the second subband of the quantum well, such that only one subband is populated. The quantum well needs to be narrow enough such that the second subband of the quantum well lies high,

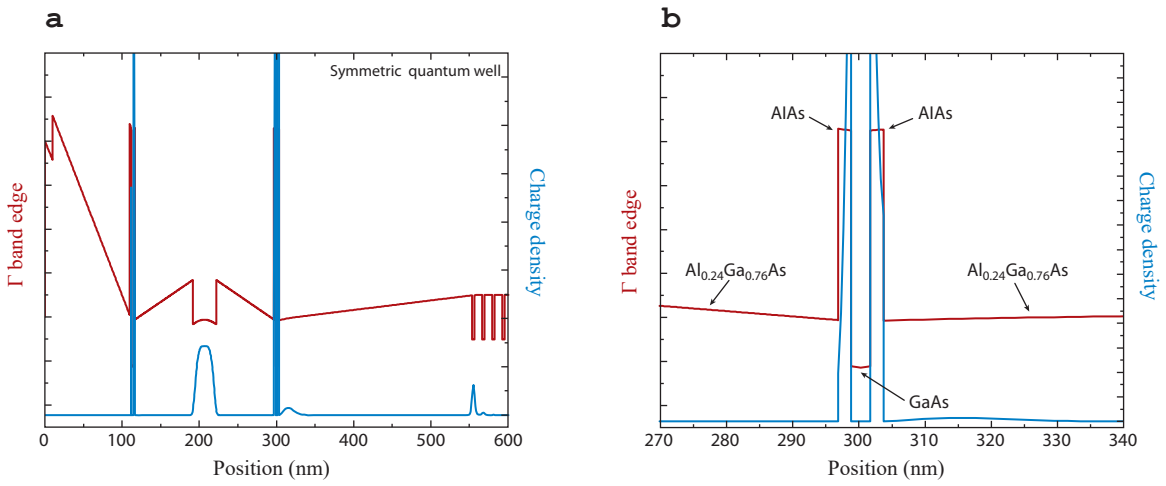

Figure 1.1: (a) Conduction band edge and charge density profile for a modern high-mobility quantum well. The silicon donors are located in the center of a narrow GaAs well and surrounded by AlAs. (b) A zoom-in of the doping well. (Adopted from [22])

and meanwhile wide enough such that the electrons do not experience too much scattering potential from the interface roughness; the spacer needs to be thin enough such that enough electrons migrate to the GaAs quantum well as a larger 2DEG density usually means better screening of the disorder potential, and meanwhile thick enough so that the scattering potential due to the ionized donors is suppressed. Increasing the donor concentration is another way to increase the 2DEG density, and, naively one would think that a larger concentration of donors would bring in more scattering. However, overdoping, although it couldn't further increase the 2DEG density once the donor energy level reach the Fermi level, turns out to help with the 2DEG quality. One reason is that it helps with the homogeneity of the 2DEG; in addition, the excess electrons that do not go to the quantum well provide extra screening of the disorder potential. This idea was further developed into the "doping well" [23, 22] scheme, which has significantly advanced the 2DEG quality and has been widely applied. A illustration of such scheme is shown in Fig. 1.1. In the "doping well" design, the Si impurities are placed in very narrow GaAs quantum wells, flanked by narrow AlAs (which is barrier at the Γ point). The excess electrons reside at the X point of AlAs and has a high effective mass. This helps to reduce the chance of parallel conduction from the excess electrons, while they are still mobile enough to screen the disorder potential.

Also, it is preferable that Si are doped from both sides of the quantum well; this helps with producing higher electron densities than the single-interface heterostructures, and also makes the quantum well and electron wavefunction essentially symmetric in the confinement direction, thus reducing the scattering due to the interface roughness. In most typical high mobility structures we use, the quantum well is about 30 nm, the spacer thickness around 75 nm and the carrier density n_e about 3×10^{11} cm^{-2}.

1.2 Types of disorder in a 2DEG

In a clean 2DEG, the main sources of disorder include remote donors and background impurities. The most conventional way to characterize disorder has been the study of transport properties, and especially through the scattering lifetime τ and mobility $\mu = e_0\tau/m^*$, with m^* being the carrier effective mass. Here we briefly discuss how these parameters are dependent on different types of disorder, while a more thorough discussion of transport is saved to Chapter 3.

The Fourier component of the scattering potential from the donors can be written as

$$W_q \sim e^{-qd}\,. \tag{1.1}$$

Therefore, the correlation length of the disorder potential experienced by the 2DEG is on the order of $q^{-1} \sim d$, while any disorder potential on a smaller length scale is exponentially damped. In the typical case of $k_F d \gg 1$, where $k_F = \sqrt{2\pi n_e}$ is the Fermi wavevector (for $n_e = 3\times10^{11}$ cm^{-2} and $d = 75$ nm, $k_F d \approx 10$), scattering with the remote donors is predominate on small angles. In this case, transport scattering rates due to remote donors can be written as

$$\frac{1}{\tau} = m^* \int_0^{2\pi} \frac{d\phi}{2\pi}(1-\cos\phi) W_{q=2k_F\sin(\phi/2)} \tag{1.2}$$

$$= \frac{m^*}{k_F^3}\int_0^{\infty}\frac{dq}{2\pi}q^2 W_q\,, \tag{1.3}$$

Inserting Eq. (1.1) into the equation above gives

$$\frac{1}{\tau} \sim (k_F d)^{-3} \tag{1.4}$$

On the other hand, the total scattering rates, which do not weight on the scattering angles, and which determines the broadening of energy levels such as Landau levels as we'll discuss

in the next chapter, is written as

$$\frac{1}{\tau_q} = m^* \int_0^{2\pi} \frac{d\phi}{2\pi} W_{q=2k_F \sin(\phi/2)} \tag{1.5}$$

$$= \frac{m^*}{k_F} \int_0^{\infty} \frac{dq}{2\pi} W_q \tag{1.6}$$

$$\sim (k_F d)^{-1} \sim (k_F d)^2 \frac{1}{\tau} \,. \tag{1.7}$$

Therefore, both τ and τ_q increases with increasing carrier density or the spacer thickness, but τ_q due to remote donors is usually much smaller than τ.

In addition to remote donors, background impurities in the 2D channel are unavoidable. They come from either the residual gas in the ultra-high vacuum MBE environment, or impurities in the source material [24]. In the state-of-art materials nowadays, the concentration of background impurities N_{bg} is about 5 $\times 10^{13}$ cm^{-3} [22]. The characteristic length scale of the background impurities is the 2D screening length, which is Bohr radius, $a_B = \epsilon\hbar^2/m^*e^2$ in Gaussian units. Here $\epsilon = 12.8$ is the dielectric constant in GaAs. The Bohr radius is thus about 10 nm in GaAs. On the simplest level, the scattering lifetime can be taken as the time of flight between two impurities along a straight line,

$$1/\tau \sim v_F N_{bg} a_B^2 \,, \tag{1.8}$$

where $v_F = \hbar k_F/m^*$ is the Fermi velocity.

1.3 How to characterize the "quality" of 2DEG?

Historically, a clean or high quality 2DEG usually means a 2DEG of high mobility. Indeed, the mobility at zero magnetic field at low temperature has been the most popular and convenient parameter for characterization. The same criterion is still being used in many other material systems. However, it is most interesting to study the behavior of a 2DEG under perpendicular magnetic field, and it has been realized that [25, 26], the mobility is not a good predictor for the quality of the interesting phases under magnetic fields. In addition, practical tricks such as illumination [27] has been known to significantly improve the quality of interesting phases though having little effect on mobility. The total scattering rates τ_q, which can be decided from the Shubnikov-de Haas oscillations, and non-equilibrium magneto-oscillations (as we'll discuss in later chapters) has been proposed to be a better

criteria for sample quality [26]. This idea, nevertheless, has also encountered opposition, for example, when the change of τ_q as a function of carrier density is compared to that of the excitation gap at the fractional quantum Hall states at $\nu = 5/2$ [28]. Instead, it was proposed that the resistance at $\nu = 5/2$ at 0.3 K, is a good predictor for the magnitude of the excitation gap at $\nu = 5/2$ at low temperatures [29]. However again, a large $\nu = 5/2$ gap doesn't necessarily guarantee that the sample would reveal "high-quality" stripe phases or microwave-induced resistance oscillations. In short, different phases and phenomena in 2DEG have different dependence on disorder properties and a universal characterization criterion for the study of different phases does not seem to be feasible.

Perhaps, compared to "how to characterize the quality of the 2DEG", a more valid question is, "how to further minimize the disorder in the 2DEG so that new physics can be discovered". Ongoing efforts include further purifying the MBE source material [22, 24] and improving the doping scheme. The answer is so far unclear but definitely exciting if it exists.

Chapter 2

The general properties and various ground states of a 2DEG under a magnetic field

The ultimate many-body Hamiltonian of a 2DEG in a magnetic field can be written as the following, [1]

$$H = H_{\text{kinetic}} + H_{\text{Zeeman}} + H_{\text{confinement}} + H_{\text{disorder}} + H_{\text{interaction}} + H_{\text{drive}}\,. \tag{2.1}$$

Here, $H_{\text{confinement}}$ is the electrostatic confinement potential of the physical sample, $H_{\text{interaction}}$ is the Coulomb interaction between electrons, and H_{drive} is the microwave radiation field or dc current which may or may not be present. We note that, unlike other condensed matter systems, the lattice band structure can be disregarded in most circumstances, and information of the GaAs band structure only appear in the effective mass m^* and g factor. This property is due to the small Fermi wavevector compared to the size of Brillouin zone, and makes the GaAs 2DEG a simple system. While the first 3 terms (with a certain confinement potential) are exactly solvable, the additional of disorder and interactions makes an exact solution impossible. Nevertheless, many interesting phenomena can be understood reasonably well. Below we first discuss the single-particle solution without considering the interactions, and then discuss the effect of interactions for certain situations.

[1] Of course, additional terms such as H_{SO} considering the spin-orbital interaction and $H_{hyperfine}$ considering the nuclear hyperfine interaction are sometimes needed but for this thesis the following is sufficient.

2.1 Single-particle problem

2.1.1 Landau quantization

Kinetic term − The essence of the problem stems from the kinetic term which gives rise to heavily-degenerate Landau levels. For a single electron under an magnetic field,

$$\hat{H}_{\text{kinetic}} = \frac{1}{2m^*}\hat{\boldsymbol{\pi}}^2 = \frac{1}{2m^*}[\hat{\boldsymbol{p}} - e\hat{\boldsymbol{A}}(r)]^2 \tag{2.2}$$

where $\nabla \times \boldsymbol{A} = \boldsymbol{B}$. For $\boldsymbol{B} = B\hat{z}$, we note that

$$[\hat{\pi}_x, \hat{\pi}_y] = i\hbar e\left[\frac{\partial}{\partial x}A_y - \frac{\partial}{\partial y}A_x\right] = i\hbar eB\,. \tag{2.3}$$

We can define another operator $\hat{\boldsymbol{o}} \equiv \hat{\boldsymbol{\pi}}/\sqrt{\hbar eB}$, so that

$$[\hat{o}_x, \hat{o}_y] = i\,, \tag{2.4}$$

and

$$\hat{H}_{\text{kinetic}} = \frac{\hbar eB}{2m^*}\left[\hat{o}_x^2 + \hat{o}_y^2\right] = \frac{\hbar\omega_{\text{c}}}{2}\left[\hat{o}_x^2 + \hat{o}_y^2\right]\,. \tag{2.5}$$

where $\omega_c = eB/m^*$ is the cyclotron frequency. Eq. (2.4) and Eq. (2.5) above suggests that the problem is nothing but that of a simple harmonic oscillator, and the energy levels can thus be written down as,

$$E_N = \hbar\omega_{\text{c}}(N + 1/2)\,. \tag{2.6}$$

Now, the energy spectrum is split into a set of equally-spaced LLs with the energy gap of $\hbar\omega_{\text{c}}$ and N is the quantum number known as the LL index. For a 2DEG in the absence of a magnetic field, the density of states (DOS) per spin per unit area is a constant of energy, $m^*/2\pi\hbar^2$. Since the application of magnetic field cannot change the total number of states, what it does can be taken as compressing the states in the energy interval $\hbar\omega_{\text{c}}$ to a single level. Therefore, the degeneracy of each level is

$$N_B = \hbar\omega_{\text{c}} \times m^*/2\pi\hbar^2 = eB/h\,. \tag{2.7}$$

In other words, for each LL, there is exactly one state per flux quanta h/e. One can also define the filling factor ν, which is the number of filled LLs, as

$$\nu = n_e h/eB\,. \tag{2.8}$$

The massive degeneracy of states for a single energy level suggests that there could be many representatives to write down the wavefunctions, which can be obtained by choosing different gauges for the vector potential. We emphasize that the LL quantization and the level degeneracy discussed above are independent of the choice of gauge. The two most used gauges are the Landau gauge and the symmetric gauge.

Under the Landau gauge $\boldsymbol{A} = (0, -Bx, 0)$, the wavefunction corresponding to the N-the LL can be written as

$$\Psi_{N,m}(x, y) = A_L \phi_N(x - l_B^2 k_m) e^{ik_m y}\,, \tag{2.9}$$

which is localized along one direction and a plane wave along the other. Here $\phi_N(x) = H_N(x/l_B)e^{-x^2/l_B^2}$ is the N-th linear oscillator state [$H_N(x)$ is the Hermite function], $l_B = \sqrt{\hbar/eB}$ is the magnetic length, and $A_L = (\pi 2^{2n}(n)^2)^{-1/4}$ is the normalization factor. For a 2DEG of the dimension $L_x \times L_y$, k_m takes on values of $\frac{2\pi}{L_y}m$ (m is an integer) to satisfy the boundary conditions, while smaller than L_x/l_B^2. This gives the total number of states that can be accommodated in each level as $L_x L_y / 2\pi l_B^2$. Noting that $1/2\pi l_B^2 = eB/h$, the degeneracy of each level per unit area, the above expression is consistent with Eq. (2.8). The Landau gauge is the common choice for the construction of stripe phases, and for problems under an constant electric field.

2.1.2 Spin, disorder and confinement potential

Zeeman term − The Zeeman term lifts the degeneracy between opposite spin index with $E_z = g\mu_B B$ where g is the g-factor, and μ_B is the Bohr magnon. Therefore, each LL consists of two spin branches. For the typical parameters of a GaAs 2DEG, $m^* = 0.067m_0$ (m_0 is the bare electron mass) and $g = 0.44$, the Zeeman gap is much smaller than the cyclotron gap. However, the energy gap between different spin branches of the same LL is usually enhanced to be much larger than the Zeeman gap, due to the exchange interactions [30, 31]. We'll save this point for later sections.

Disorder term − In a simple picture, disorder introduces level broadening; the density of states (DOS) in the presence of LLs are therefore no longer a sum of delta-functions. The exact shape of broadened LLs depends on the properties of the disorder potential [19, 8]. Simply put, from theoretical calculations, a semicircle shaped DOS has been obtained for weak white noise disorder potential [32] and a Gaussian DOS was obtained for smooth

varying potential [33]. From the experimental side, the DOS has been studied through magneto-capacitance [34, 35] and magnetization [36] measurements, with conflicting results, either Lorentzian [35] or Gaussian [34] shape and the width either dependent [36] or independent [34, 35] of B. Nevertheless, it is usually accepted, through the Heisenberg uncertainty relationship that the width $\Gamma = \hbar/\tau_q$, where τ_q is the quantum scattering lifetime. At very low magnetic fields where $\Gamma \ll \hbar\omega_c$, the Landau quantization is blurred out by disorder, and the magnetic field only introduces oscillations in the DOS,

$$\nu(E) = \nu_0 \left[1 - 2\lambda \cos \frac{2\pi E}{\hbar\omega_c}\right] \tag{2.10}$$

where $\nu_0 = m/2\pi\hbar^2$ is the DOS in the absence of magnetic field, and $\lambda = e^{-\frac{\pi}{\omega_c \tau_q}}$ is a small quantity, called the Dingle factor.

Confinement potential − In the discussions above, we have neglected the confinement potential. For most of the problems, only the confinement in the z direction is relevant so the potential is just $V(z)$. If only a perpendicular magnetic field is applied, on the single-particle level, the motion along z direction can always be separated from the main Shrodinger equation and the 2D results above are independent of $V(z)$. However, if the magnetic field has a in-plane component, it is no longer possible to separate the motion along z direction from the 2D motion, and $V(z)$ is important in this situation. The problem is only exactly solvable with a parabolic $V(z)$ [37]. In some cases, one need to consider the physical or gate-defined boundaries in the 2D plane. An important example is the quantum Hall edge states [38] which we will discuss later in Sec. 3.5.

2.2 Electron-electron interactions

So far we have been neglecting the interaction between electrons. The interactions between electrons in the setting of LLs give rise to many interesting phases. The interaction energy is smaller than the cyclotron gap. Things are particularly interesting in the partially filled Landau levels. The interactions depends on the shape of the wavefunctions, or the LL index.

2.2.1 The lowest LL

How will the electrons in a single LL organize themselves to minimize the total interaction energy? Let's start from the case where electrons are sparse, with the average distance

between them much larger than l_B characterizing the spatial extend of their wave-functions. In this situation, a quasi-classical treatment catches the physics well, that electrons would organize themselves into a Wigner crystal of triangular lattice to avoid interacting with other electrons. Wigner crystals are observed for below filling factor around $\nu = 1/5$ [39, 40].

More interestingly, electrons can organize themselves into incompressible liquids at certain filling factors, which gives rise to the fractional quantum Hall effects. Laughlin proposed a trial many-body wavefunction for $\nu = 1/q$ [3],

$$\psi_{1/q} = \prod_{i<j} (z_i - z_j)^q \exp\left(-\frac{1}{4l_B^2} \sum_i |z_i|^2\right), \tag{2.11}$$

where q is an odd integer to keep ψ anti-symmetric and z_i is the position of the ith electron in complex numbers. It can be seen that for $q = 1$, Eq. (2.11) is many-body wavefunction for $\nu = 1$, which is constructed from the single-particle wavefunction under the symmetric gauge and satisfies the Pauli inclusive principle. The Laughlin wavefunction characterizes a uniform and imcompressible liquid, which has a gap in the excitation spectrum and its quasiparticle carrying fractional charge. Numerical calculations in small systems provided support that the Laughlin wavefunction describes well the ground state in the presence of electron-electron interactions. Moreover, the fractional charge has been detected experimentally by tunneling [41], shot noise [42, 43] and single electron transistor [44] measurements.

The Laughlin wavefunction above describes fractional quantum states at $\nu = 1/q$, with q being an odd integer. By the particle-hole symmetry one can expect similar state at $\nu = 1 - 1/q$, and by the symmetry in spin branches, at $\nu = 1 + 1/q$ and $2 - 1/q$. However, fractional quantum Hall states have been observed at many other filling factors that cannot be described by the above. Jain has brought up a composite fermion model which elegantly accounted for these fractional QH states. In this model, one electron can absorb an even number of flux quanta and become a composite Fermion. The composite fermion then experience a reduced effective magnetic field, and form a set of "Λ levels" in analogous to the Landau levels. At $\nu = 1/2$, the effective magnetic field experienced by the composite Fermions is zero, and the system can be described by a composite Fermion sea which can be well described by the Landau Fermion liquid theory. At

$$\nu = n^*/(n^* p \pm 1), \tag{2.12}$$

where p is the number of flux quanta, n^* numbers of "Λ levels" are occupied, and the system

becomes incompressible and gapped. The picture of composite Fermions has also received considerable support from experiments. The physical entity of composite Fermions were confirmed by surface acoustic wave [45], magnetic focusing [46, 47], cyclotron resonance [48] and geometry commensurability measurement [49]. Recently, it has been proposed that the composite Fermion at $\nu = 1/2$ is a Dirac Fermion [50]. However, this proposal has not received support from experiments.

We note that the presence of disorder [51] as well as the quantum confinement potential [52, 53] can tune the competition between the above two states. In short, the reason is that the formation of the Wigner solid is driven by the long-range part of the interaction, while the fractional QH liquid derives its energy advantage from the short-range part [52]. If the spread of the wavefunction in the z direction is large enough, the Coulomb interaction can be softened at short distances in the 2D plane, and a WC phase is favored over the fractional QH liquid state [53]. WC phase may also be favored in disordered 2DEG [51]. At filling factors where neither WC or fractional QH states are favored, the 2DEG form a isotropic compressible liquid.

2.2.2 The high LL problem

When multiple Landau levels are occupied, it can be shown that the low-energy physics is dominated by the electrons in the topmost spin-resolved LL, while other electrons only act as an effective dielectric medium and provide screening [30]. The effective Hamiltonian of Coulomb interactions can be written as,

$$H_{eff} = \frac{1}{2}\sum_{\boldsymbol{q}} v(q)\rho(\boldsymbol{q})\rho(-\boldsymbol{q})\,, \tag{2.13}$$

where $\rho(\boldsymbol{q})$ is the usual density operator in q space. Here, the bare Coulomb interaction is replaced by the renormalized interaction

$$v(q) = \frac{v_0(q)}{\epsilon(q)}\left[F_N(q)\right]^2\,, \tag{2.14}$$

where $v_0(q) = 2\pi e^2/q$, $\epsilon(q)$ is the dielectric function due to screening by other LLs [54, 30], and $F_N(q)$ is the form factor

$$F_N(q) = \int dxdy|\psi|^2 e^{-iqx} = L_N(\frac{q^2 l_B^2}{2})e^{-q^2 l_B^2/4} \tag{2.15}$$

with L_N being the Laguerre polynomial. It turns out that such an unusual interaction results in the formation of charge density waves [4, 5]. It is an remarkable example that electron clustering originates from pure repulsive interactions.

CDW instability in q space − Within the Hartree-Fock approximation, the CDW cohesive energy per electron can be written as,

$$H_{HF} = \frac{1}{2\nu^*(2\pi l_B^2)} \sum_{\boldsymbol{q}} u_{HF}(q) |\Delta(\boldsymbol{q})|^2 \,. \tag{2.16}$$

Here u_{HF} is the Hartree-Fock potential, $u_{HF}(q) = (1-\delta_{q,0})u_H(q) - u_F(q)$, and

$$u_H(q) = v(q), u_F(q) = \int \frac{d^2p}{(2\pi)^2} v(p) e^{i(p_x q_y - p_y q_x) l_B^2} \,; \tag{2.17}$$

$\Delta(\boldsymbol{q})$ is the CDW order parameter, with its Fourier transformation $\Delta(\boldsymbol{r})$ proportional to the guiding center density at point $\boldsymbol{r}$, $\Delta(\boldsymbol{r}) = \nu(\boldsymbol{r})/L_x L_y$. The next step is then to find the distribution of the guiding center that minimizes the energy. For $N > 0$, the form factor $F(q)$ has zeros. This leads to zeros in the Hartree potential at certain wavevectors, the smallest one at $q_0 = 2.4/R_c$. This originate from the shape of the wavefunction. Indeed, the charge density is a product of the guiding center density and the wavefunction form factor,

$$\rho_e(q) = e\Delta(q) F_N(q) \,. \tag{2.18}$$

A modulation at q_0 thus induces no charge density and no Hartree penalty. At the same time, the exchange part which is always negative, leads to the CDW instability. The HF potential is negative at a range of q's, but has it minimum at q_0. It is not surprising that the two most likely CDWs would be stripe and bubble phases as in most circumstances in nature [55].

Intuitive picture of CDW formation in real space − It is more intuitive to look at the HF potential in real space. Through a Fourier transformation, it can be shown that the HF potential has the asymptotic expression [5],

$$u_{HF}(\boldsymbol{r}) \approx E_b(r)\Theta(2R_c - r) + E_h[1 - \delta(r)/2\pi l_B^2] \,, \tag{2.19}$$

where $E_b(r) \sim (4R_c^2 - r^2)^{-1/2}$ is a rather flat function of r. Neglecting the second which is the hydrodynamic term [30, 5], the potential has a disk-like form due to the step function. In other words, the repulsive interaction experienced by one electron due to other electrons

has a plateau below $2R_c$. At partial filling factors where the average distance between electrons, $d_\nu \sim l_B/\sqrt{\nu^*}$, is much smaller than $2R_c$, it doesn't cost much more energy for electrons to move even closer, meanwhile, by doing so it could avoid interaction with other electrons. Eventually the guiding centers form into clusters and the final pattern depends on ν^*. It was found that for ν^* close to 1/2, stripe phase is formed while for ν^* away from 1/2, the bubble phase prevails. They are separated by a first-order transition at around ν^* = 0.39 (0.61).

For the stripe phase, [2] the 1D solution for $\Delta(\boldsymbol{q})$ can be written as,

$$\Delta(q\hat{\boldsymbol{x}}) = \frac{2}{qa}\sin\left(\frac{\nu^* qa}{2}\right), \tag{2.20}$$

where a is the optimized period, $a = 2.7R_c$ according to the HF calculations. The expression above describes stripes of width $a\nu^*$ with occupied guiding center states separated by stripes of width $a(1-\nu^*)$.

For the 2D bubble phase, the clusters of electrons will form a triangular lattice just like in the WC phase. Indeed, the WC phase can be taken as a special case where the electron in each cluster is 1. The optimized lattice constant can be found numerically to be similar to that of stripes. The area of unit cell of the bubble lattice is equal to $S_b = 2\sqrt{3}\pi^2 a^2$, and the number of particles per bubble is therefore $N_b = S_b\nu^*/2\pi l_B^2$. Using $q_0 = 2.4/R_c$, $N_b \approx 3\nu^* N$. Only the phases with integer N_b are found stable. Bubble phases of different N_b are thus separated with first-order transitions: as ν^* is varied, the lattice constant of the bubble phase changes smoothly and when discontinuously when it comes to a transition [56].

The validity of the Hartree-Fock approach − Unlike in the lowest LL where the incompressible quantum liquid could never originate from the HF approach, the HF theory is valid in the $N \gg 1$ limit. This can be understood as the lattice constant of the CDW, on the order of $R_c = \sqrt{2N+1}l_B$, is much larger than l_B, which is the length scale of quantum fluctuations. An alternative understanding is that, each electrons interact with a large number of neighbors, estimated as $\pi(2R_c)^2\nu^*/2\pi l_B^2 = 2(2N+1)\nu^*$. In this case each electron may be considered to interact only with an averaged background, without being influenced by individual motions. Although the arguments above do not exactly hold for

[2] The solution can be found using the 1D HF potential but setting $q_y = 0$ in for Fourier transformation. The 1D potential is also box-like, i.e., $\sim \Theta(2R_c - x)$ asymptotically.

$N = 2$, where CDW are observed to be the strongest in experiments, numerical calculations [57, 58, 59] has confirmed CDW to be the ground states for $N = 2$. Furthermore, the HF predicts many properties consistent with experiment, such as the transition ν^* between stripe and bubble phases.

Experiments − Experimentally, significant anisotropy between resistances along orthogonal directions were observed in GaAs 2DEGs, at filling factors 9/2, 11/2, 13/2, 15/2 and so on [6, 7]. The strong transport anisotropy is in sharp contrast with the essentially isotropic transport in the lowest two LLs and very high LLs, and consistent with the theoretical prediction of CDW formation. Meanwhile, reentrant integer quantum Hall states are observed consistent with the insulating "bubble" phase. Detailed discussion about transport in the CDW regime are saved to Chapter 3.

The observation of significant transport anisotropy in the stripe phases in a macroscopic sample relies on the presence of long-range orientational order, which was not expected. Indeed, the original theoretical proposal [4, 5] expected that stripes of random orientation would exist in domains, and their detection would require experiments different than a simple transport measurement in a macroscopic sample, such as the measurement of tunneling density of states. In contrast, the surprising experimental results suggest a symmetry breaking mechanism that aligns the stripes in a certain direction. This direction is observed to be the $\langle 110 \rangle$ crystal axes of GaAs in most of the past studies [6, 7], and in some rare cases along the $\langle 1\bar{1}0 \rangle$ crystal axes [60, 61, 62]. The origin of the symmetry breaking mechanism which decides the native stripe orientation has been a longstanding puzzle. It has been observed that stripes orientation can be modified by a number of means, including the application of an in-plane magnetic field $B_{\parallel}$ [11, 12], stain [63], changing the carrier density [60, 61], symmetry of the quantum well [61], density modulation [64], etc. We save a detailed discussion of stripe orientation to Chapter 4.

In addition to transport, the stripe and bubble phases has been probed by various techniques. Resonances with the disorder pinning modes has been observed in these phases, confirming the electronic crystalline order [65, 66, 67, 68]; exploiting nuclear magnetic resonance, spatial spin modulation concomitant with the charge modulation has been detected [69, 70]; the stripe period has been also measured through experiments involving surface acoustic waves with controlled wavevector [71]; in addition, negative permittivity has been suggested in the measurements of velocity shift of surface acoustic waves propagating in

stripes and bubble phases [72].

2.2.3 The second LL - a stage of competitions

The $N = 1$ LL manifest as a stage of delicate competitions between the phases discussed above. First, it host fractional QH states, e.g., at $\nu = 7/3, 8/3$, similar to the first-discovered $1/3$ state in the lowest LL, which has no counterparts at higher LLs. More interestingly, it also host the even-denominator fractional QH states at $\nu = 5/2$ [73] which cannot be described by the Laughlin wavefunction or the Jain series. The fractional QH states at $\nu = 5/2$ can be tuned in to a stripe phase by the application of an in-plane magnetic field $B_{\|}$ [11, 12] or hydrodynamic pressure [74]. In addition, four reentrant integer quantum Hall states in each spin branch has been observed [75, 76], suggesting the formation of bubble phases similar to those in high LLs, albeit with much smaller energy scales [76].

Chapter 3

Magnetotransport

Magneto-transport studies has been the most convenient and powerful technique to study the 2DEG. The famous integer and fractional quantum Hall effects bear their name based on their transport properties. In this chapter, we discuss the transport properties of a 2DEG in different phases.

3.1 General considerations

On the most classical level, a perpendicular magnetic field deflects the motion of electrons due to a Lorentz force, and the resistivity connecting the electric field $\boldsymbol{E}$ and current density $\boldsymbol{j}$ a second order tensor

$$\begin{pmatrix} E_x \\ E_y \end{pmatrix} = \begin{pmatrix} \rho_{xx} & \rho_{xy} \\ \rho_{yx} & \rho_{yy} \end{pmatrix} \begin{pmatrix} j_x \\ j_y \end{pmatrix} ,$$

and the conductivity

$$\begin{pmatrix} \sigma_{xx} & \sigma_{xy} \\ \sigma_{yx} & \sigma_{yy} \end{pmatrix} = \begin{pmatrix} \rho_{xx} & \rho_{xy} \\ \rho_{yx} & \rho_{yy} \end{pmatrix}^{-1} .$$

Before more specific discussions, we note that

$$\sigma_{xx} = \frac{\rho_{yy}}{\rho_{xx}\rho_{yy} + \rho_{xy}^2} , \quad \sigma_{yy} = \frac{\rho_{xx}}{\rho_{xx}\rho_{yy} + \rho_{xy}^2} . \tag{3.1}$$

Therefore, in the isotropic case of $\rho_{xx} \approx \rho_{yy} \ll \rho_{xy}$, we have $\rho_{xx} \sim \sigma_{xx}$, which is a peculiar transport characteristics in magnetic fields, in contrast to $\rho_{xx} = \sigma_{xx}^{-1}$ in zero magnetic field.

In the anisotropic case with significant difference between ρ_{xx} and ρ_{yy} such as in the stripe phases, we have $\rho_{xx} \sim \sigma_{yy}$ and $\rho_{yy} \sim \sigma_{xx}$.

In experiments, what we directly measure is the current I and voltage V (from which we obtain the macroscopic resistance R_{xx} and R_{xy}), rather than the current density j or electric field E. We denote the distance between the two voltage probes along the current flowing direction as L_x and the sample width perpendicular to the current flow as L_y. As long as the resistivity is homogeneous within the sample, we always have $R_{xy} = V_{xy}/I = \int \rho_{xy} j_x(y) dy / \int j_x(y) dy = \rho_{xy}$, irrespective of the geometry or current distribution. On the other hand, the geometry factors and current distribution are important in deciding the relation between R_{xx} and ρ_{xx}. In the assumption that the current is distributed uniformly in the sample, i.e., $j = I/L_y$, which is what a Hall bar geometry attempts to achieve, we have $R_{xx} = \frac{L_x}{L_y}\rho_{xx}$. Another commonly used geometry is the Van der Pawu geometry.

3.2 Drude formula

Main results - We first give the main results of Drude formula and then discuss different approaches to derive it. At the most basic level, the classical magnetotranport is described by the Drude formula,

$$\rho_{xx} = \rho_D \equiv m^*/n_e e^2 \tau \, , \rho_{xy} = B/n_e e \, , \tag{3.2}$$

or

$$\sigma_{xx} = \frac{\sigma_D}{1 + (\omega_c \tau)^2} \, , \sigma_{xy} = \frac{\sigma_D (\omega_c \tau)}{1 + (\omega_c \tau)^2} \, , \tag{3.3}$$

where $\sigma_D \equiv 1/\rho_D = n_e e^2 \tau / m^*$, and τ is the transport lifetime. The important feature of Drude formula is as follows. First, the Hall resistivity ρ_{xy} is a linear function of B, with its slope only decided by the carrier density. Second, the longitudinal resistivity is independent of the magnetic field.

Drude model - The Drude formula was commonly derived by solving the classical equation of motion in crossed magnetic and electric fields in the stationary state,

$$-m^* \frac{\boldsymbol{v}}{\tau} - e(\boldsymbol{E} + \boldsymbol{v} \times \boldsymbol{B}) = m^* \frac{d\boldsymbol{v}}{dt} = 0 \, . \tag{3.4}$$

All the information on disorder and scatterings was encoded in the scattering time τ, after which the electron loses its velocity due to driving forces. It was also assumed that all

electrons contribute equally to the transport, that is, $\boldsymbol{j} = n_e e\boldsymbol{v}$, and the Fermi statistics of electrons is not respected.

Boltzmann Approach - Despite of the negligence of Fermi statistics in Drude approach, it gives the same result as can be derived within the formalism of Boltzmann kinetic equations. Like in the Drude model, the Boltzmann approach is based on the relaxation time approximation, that the distribution function relaxes to its equilibrium state with the time τ after removing all driving forces. In this approach, the crossed magnetic and electric fields cause a shift of the equilibrium distribution function,

$$f(\boldsymbol{k}) = f^0(E(\boldsymbol{k})) + \delta f(\boldsymbol{k})\,, \tag{3.5}$$

and

$$\delta f(\boldsymbol{k}) = \frac{\partial f^0(E(\boldsymbol{k}))}{\partial E(\boldsymbol{k})}\hbar k \frac{e\tau}{m^*}\frac{\cos(\varphi-\theta)}{\sqrt{1+\omega_c^2\tau^2}}|\boldsymbol{E}|\,, \tag{3.6}$$

where $f^0(E) = 1/(e^{E/k_BT}+1)$ is the Dirac-Fermi distribution function, φ is the angle denoting the direction of $\boldsymbol{k}$, and θ is the Hall angle, $\tan\theta = \omega_c\tau$. Eq Eq. (3.6) can be taken as a constant shift of the isotropic Fermi surface in the direction decided by the Hall angle θ. The dissipative current can then be written as

$$\boldsymbol{j} = -e\sum_{\boldsymbol{k}}\boldsymbol{v}(\boldsymbol{k}) = -e\sum_{\boldsymbol{k}}\boldsymbol{v}(\boldsymbol{k})\delta f(\boldsymbol{k})\,, \tag{3.7}$$

as the equilibrium part contributes no dissipation. The sum over $\boldsymbol{k}$ can be changed into a integral of energy, and Eq. (3.3) can be obtained.

Fermi's golden rule - The Drude-Boltzmann formula assumes a relaxation time τ without accounting for the microscopic scattering process. Now we focus on the scatterings. In a magnetic field, a scattering of a electron causes a displacement of the guiding center of the cyclotron orbit, which in turn leads to a energy shift in the presence of an electric field, $\boldsymbol{E} = E_x\hat{\boldsymbol{x}}$. For the initial state $\boldsymbol{k_1} = k_F(\cos\varphi_1, \sin\varphi_1)$ and final state $\boldsymbol{k_2} = k_F(\cos\varphi_2, \sin\varphi_2)$, the energy shift

$$W_{\varphi_1\varphi_2} = eE_x\Delta x = eER_c(\sin\varphi_1 - \sin\varphi_2)\,. \tag{3.8}$$

This allows us to account for the scatterings in real space. The dissipative longitudinal current resulting from the scatterings can be written as a sum of j_x^+ and j_x^-,

$$j_x = 2e\nu_0\int_{-\infty}^{0}dx_1\int_0^{\infty}dx_2\left(P_{x_1\to x_2} - P_{x_2\to x_1}\right)\,. \tag{3.9}$$

The scattering probability $P_{x_1 \to x_2}$ and $P_{x_2 \to x_2}$ are given by the integrals over the initial and final energies in the scttering event,

$$P_{x_1 \to x_2} = \int^{+} \frac{d\varphi_1 d\varphi_2}{(2\pi)^2} \int dE_1 dE_2 d\Omega \delta(E_2 - E_1 - \Omega)\delta(x_2 - x_1 - \Delta x)\Gamma_{12} M \,, \tag{3.10}$$

where Γ_{12} is the scattering probability,

$$\Gamma_{1,2} = \delta(\Omega - W_{\phi_1\phi_2})\tau_{12}^{-1} \,, \tag{3.11}$$

and

$$M = \tilde{\nu}_1 \tilde{\nu}_2 f(E_1)\,[1 - f(E_2)] \tag{3.12}$$

takes care of the scattering phase space. Here we introduce the normalized density of states $\tilde{\nu}_i = \nu(E_i)/\nu_0$, which equals unity if we ignore the oscillations in DOS for now. The angle integrals in the Eq.Eq. (3.10) are done in the region for $\Delta x > 0$. For $P_{x_2 \to x_2}$, the angle integral are done in the region for $\Delta x < 0$, and Δx and $W_{\phi_1\phi_2}$ in the delta functions are replaced by $-\Delta x$ and $-W_{\phi_1\phi_2}$.

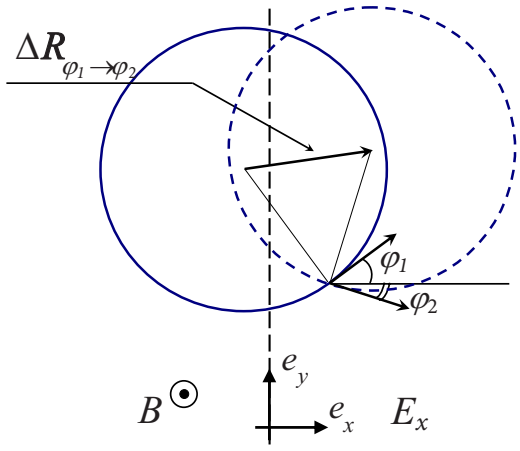

Figure 3.1: Illustration of disorder scattering which leads to the displacement of the cyclotron motion guiding center. [Adopted from [77]]

We can first evaluate the spatial integral. For $\Delta x > 0$,

$$\int_{-\infty}^{0} dx_1 \int_{0}^{\infty} dx_2 = \int_{-\Delta x}^{0} dx_1 \tag{3.13}$$

while for $\delta x < 0$,

$$\int_{-\infty}^{0} dx_1 \int_{0}^{\infty} dx_2 = \int_{\Delta x}^{0} dx_1 \tag{3.14}$$

One can then interchange the angular variables in the expression for $P_{x_2 \to x_1}$, so

$$j_x = 2e\nu_0 \int^{+} \frac{d\varphi_1 d\varphi_2}{(2\pi)^2} \int_{-\Delta x}^{0} dx_1 \int dE_1 dE_2 \delta(E_2 - E_1 - W_{\phi_1\phi_2}) \tau_{12}^{-1} \tilde{\nu}_1 \tilde{\nu}_2 \tag{3.15}$$

$$\{f(E_1)\,[1 - f(E_2)] - f(E_2)\,[1 - f(E_1)]\} \tag{3.16}$$

$$= 2e\nu_0 \int^{+} \frac{d\varphi_1 d\varphi_2}{(2\pi)^2} \Delta x \int dE_1 \tau_{12}^{-1} \tilde{\nu}_1 \tilde{\nu}_2 \,[f(E_1) - f(E_1 + W_{\phi_1\phi_2})] \tag{3.17}$$

For weak E_x, we can linearize the last term in the bracket and obtain,

$$j_x = 2e\nu_0 \int^{+} \frac{d\varphi_1 d\varphi_2}{(2\pi)^2} eE_x \Delta x^2 \int dE \tau_{12}^{-1} \tilde{\nu}_1 \tilde{\nu}_2 \left[-\frac{\partial f}{\partial E}\right] \tag{3.18}$$

$$= 2e^2 \nu_0 R_c^2 E_x \int^{+} \frac{d\varphi_1 d\varphi_2}{(2\pi)^2} (\sin\varphi_1 - \sin\varphi_2)^2 \tau_{12}^{-1} \int dE \tilde{\nu}_1 \tilde{\nu}_2 \left[-\frac{\partial f}{\partial E}\right] \tag{3.19}$$

Now we can evaluate the angular integral. By changing the integral variable to φ_+ and φ_- which satisfies $\varphi_1 = \varphi_+ + \varphi_-$ and $\varphi_2 = \varphi_+ - \varphi_-$, we obtain

$$\int^{+} \frac{d\varphi_1 d\varphi_2}{(2\pi)^2} (\sin\varphi_1 - \sin\varphi_2)^2 \tau_{12}^{-1} = 2 \times 4 \int_{\varphi_-}^{2\pi - \varphi_-} \cos^2\varphi_+ \int_0^{\pi} \sin^2\varphi_- \tau_{12}^{-1} \tag{3.20}$$

$$= \frac{1}{2} \int_0^{2\pi} \frac{d\theta}{2\pi} \frac{1 - \cos\theta}{\tau_\theta} = \frac{1}{2\tau_{tr}}\,, \tag{3.21}$$

where we have used $\theta = 2\varphi_- = \varphi_1 - \varphi_2$. The factor before the energy integral thus recovers the Drude conductivity in magnetic field. The generalized conductivity can be written as

$$\sigma_{xx} = \sigma_D \int dE \tilde{\nu}_1 \tilde{\nu}_2 \left[-\frac{\partial f}{\partial E}\right]\,. \tag{3.22}$$

We will see later that the golden-rule approach fomulated above describes a rich variety of phenomena when we take into account the oscillating DOS, especially under non-equilibrium conditions.

Other expressions of Drude conductivity - We note that the Drude conductivity σ_D can be expressed in different ways, which illustrate its physical meaning in different aspects. Through the Eisenstein relation,

$$\sigma_D = 2e^2\nu_0 D \;= e^2 \nu_0 v_F^2 \tau\,, \tag{3.23}$$

where $D = v_F^2\tau/2 = l^2/2\tau$ is the Diffusion constant with v_F and $l = v_F\tau$ being the Fermi velocity and mean free path. We can see that replacing l by the cyclotron radius R_c recovers Eq. Eq. (3.3) for $\omega_c\tau \ll 1$ or $l \ll R_c$. Therefore, R_c bears the role of mean free path for electron motion in a strong magnetic field. Also,

$$\sigma_D = (e^2/h)k_F l\,, \tag{3.24}$$

where e^2/h is the so-called conductance quantum, or the conductance of a single channel. $k_F l$ is thus a measure of localization.

3.3 Shubnikov-de Haas oscillations

Now we move to the modification of transport due to Landau quantization, starting from the generalized conductivity Eq. (3.22). We recall that in the presence of disorder, the generalized DOS at high LLs can be written as Eq. (2.10),

$$\tilde{\nu}(E) = 1 - 2\lambda\cos\frac{2\pi E}{\hbar\omega_c} \tag{3.25}$$

We thus write,

$$\sigma_{xx} = \int\left[-\frac{\partial f}{\partial E}\right]\sigma_D\tilde{\nu}^2(E)\;dE\,. \tag{3.26}$$

The factor $\frac{\partial f}{\partial E}$ is only nonzero for a small energy interval $\sim T$. Evaluating this integral gives the correction in conductivity to first order in λ,

$$\frac{\delta\sigma_{xx}}{\sigma_D} = -4\lambda\frac{2\pi^2T/\hbar\omega_c}{\sinh 2\pi^2T/\hbar\omega_c}\cos(2\pi E_F/\hbar\omega_c)\,. \tag{3.27}$$

The temperature damping factor appears as a result of averaging of the rapid oscillations in the density of states over thermal window $\sim T$. For $\sigma_{xy} \gg \sigma_{xx}$, it also leads to the correction in resistivity, $\frac{\delta\rho}{\rho_D} = \frac{\delta\sigma}{\sigma_D}$, known as the Shubnikov-de Haas oscillations (SdHO), which oscillates as a function of filling factor $\nu = E_F/\hbar\omega_c$, damps with temperature, and decays at low magnetic field due to the Dingle factor λ.

3.4 Microwave-induced resistance oscillations

Basic phenomenology - What happens to the resistance of a 2DEG if one shines microwaves of frequency ω on it? What was not difficult to expect is the resonance heating

at $\omega = \omega_c$ More interestingly, microwave-induced resistance oscillations (MIRO) were observed [9, 10], with the period controlled by $\epsilon \equiv \omega/\omega_c$, and amplitude increases with the radiation power and decays at low B. In the linear-power regime, MIRO have maxima at $\epsilon = n - 1/4$, where n is an integer, and minima at $\epsilon = n + 1/4$. Although MIRO decays with increasing temperature just like SdHO, they can survive higher temperature than SdHO and also persists to lower B.

There have been many theoretical proposals which produce an oscillatory contribution to the conductivity. Starting from the Fermi's golden rule approach in Eq. (3.2), the microwave modifies both the scattering rate with disorder, and the distribution function. These are called the "displacement" and "inelastic" mechanism, respectively, which we discuss below.

Displacement mechanism - We first focus on the displacement mechanism. The microwaves modify the scattering events in two aspects. First, the electrons can absorb or emit a microwave photon, and change its energy by $\pm\hbar\omega_c$ in addition to the energy change due to displacement of the guiding center. On the other hand, the ac electric field drives the electron in the 2D plane, and thus effectively smears the disorder potential experienced by the electron. This suppression of disorder scattering rate is reminiscent of the "motion narrowing". It can be shown [77] that the scattering probability which enters Eq. (3.10) can now be written as,

$$\Gamma_{12} = \frac{\mathcal{P}}{\tau_{12}} \sin^2 \frac{\varphi_1 - \varphi_2}{2} \left[\sum_{\pm} \frac{1}{2} \delta(\Omega \pm \hbar\omega_c - W_{\phi_1\phi_2}) - \delta(\Omega - W_{\phi_1\phi_2}) \right], \tag{3.28}$$

where $\mathcal{P}$ is the dimensionless effective power, which we will discuss later. Here we deal with the linear response regime, i.e., $\mathcal{P} \ll 1$. Substituting Eq. (3.28) into Eq. (3.10), in the linear dc response regime, we can obtain the correction in conductivity due to the microwave ($\sim \lambda^2$),

$$\delta\sigma_{dis} = -\sigma_D (2\lambda)^2 \mathcal{P} \frac{\tau}{2\tau^*} (\pi\epsilon \sin 2\pi\epsilon + \sin^2 \pi\epsilon), \tag{3.29}$$

where $\frac{1}{\tau^*} = 2 \int \frac{d\theta}{2\pi} \frac{(1-\cos\theta)^2}{\tau_\theta}$. It was assumed in the derivation above that $\omega \ll k_B T$ which is not realistic in experimental situations, but it can be shown that the main results are not affected at low temperatures. The displacement contribution only considers elastic scattering events, and it can be taken as originating from a modification in the distribution function in the form of

$$\delta f(E, \varphi) = A(E) \lambda (\partial f/\partial E) \cos\varphi, \tag{3.30}$$

where $A(E)$ is a function of E. It can be seen that due to the factor $\cos\varphi$, an integration over φ gives $\delta f(E) = 0$.

Inelastic mechanism - As first proposed by [78], the microwaves also produce an isotropic, energy-dependent modification to the distribution function $\delta f(E)$, which can only be stabilized by inelastic scatterings. At low temperatures, electron-electron scatterings are presumably the main source of inelastic scattering. In the linear $\mathcal{P}$ regime, the modification is found as,

$$\delta f(E) = \lambda \mathcal{P} \frac{\tau_{in}}{\tau} \frac{\partial f}{\partial E} \frac{\omega_c}{2\pi} (2\pi\epsilon \sin 2\pi\epsilon) \sin(2\pi E/\hbar\omega_c)\,, \tag{3.31}$$

which is proportional to the inelastic scattering time $\tau_{in} \sim T^{-2}$ considering e-e scattering as the inelastic relaxation mechanism. The correction in conductivity is then found as,

$$\delta\sigma_{in} = -\sigma_D (2\lambda)^2 \mathcal{P} \frac{2\tau_{in}}{\tau} (\pi\epsilon \sin 2\pi\epsilon)\,, \tag{3.32}$$

which has a the same oscillation period and phase as in the displacement mechanism.

Effective power - It is well known as the Khon's theorem [79] that cyclotron resonance (CR) and absorption only happens at $\omega = \omega_c$ and not $\omega = n\omega_c$. The observation of MIRO at high ϵ is due to a broadened CR due to disorder and radiative decay. The radiative decay is as a result of the screening of the 2DEG of the ac electric field. When the 2DEG is driven to oscillations by the ac electric field, it emits a secondary radiation. By solving the Maxwell equation, the absorption coefficient of the 2DEG under a circularly polarized microwave field can be obtained as [80],

$$A = \frac{2\gamma\Gamma}{(\omega \pm \omega_c)^2 + (\gamma + \Gamma)^2}\,, \tag{3.33}$$

where $\gamma = \tau^{-1}$ is the disorder broadening, and

$$\Gamma = \frac{2\pi n_e e^2}{m^* n^* c} = \frac{2\alpha}{n^*} \frac{E_F}{\hbar}\,, \tag{3.34}$$

is the radiative decay rate due to the collective motion of electrons. Here, $n^* \equiv \sqrt{\epsilon_{\rm eff}} = (\sqrt{\epsilon} + 1)/2$ is the effective refractive index, $\epsilon \approx 12.8$ is the dielectric constant of GaAs, and $\alpha = e^2/\hbar c$ is the fine structure constant.

All the present theoretical models presume that the MIRO depend on the power factor in the form above, which is sensitive to the polarization of the microwave. However, experiments have observed little, if any, polarization dependence on MIRO [81, 82], while at the

same time the reflection is confirmed to be dependent on polarization [81]. The insensitivity of MIRO to the polarization remains a puzzle as of now.

Zero resistance states - The MIRO minima could approach zero, giving rise to the so-called zero-resistance states (ZRS) [83, 84, 85, 86, 81, 87, 88, 89, 90, 91, 92]. The ZRS is a remarkable example of new phase forming under non-equilibrium conditions. In short, the formation of ZRS can be understood as follows [89]. The local resistivity under microwaves can be negative according to the displacement and inelastic mechanism above. But negative resistivity is not supported in a stable state; instead, current domains form which have different current flowing directions.

3.5 The integer and fractional quantum Hall effects

In Sec. 3.3, we have seen that oscillating DOS leads to the resistance oscillations in the regime of overlapping LLs. As we go to higher B, the amplitude of DOS oscillations gets larger, leading to a larger SdHO amplitude; with further increase of B, the LLs get separated, and the DOS reaches zero between LLs, which, consistent with intuition, drives the SdHO minima to zero. What is not so simply intuitive is that, the resistance stays zero for a finite range of filling factors centered at integer; more interestingly, the Hall resistance displays a plateau at quantized value $R_{xy} = ne^2/h$, known as the integer quantum Hall effect. The Hall resistance value is found to be independent of the disorder, material system or the measurement geometry, and has been employed in the precise measurement of the elementary constants and metrology [93].

The appearance of resistance zero in a finite filling factor range tells us that the resistance can be zero when the DOS at the Fermi level is finite. The reason is that the states off the LL energy due to disorder broadening, are localized states and do cont contribute to conductivity. In a real space picture, electrons circle around the peak or valleys in the disorder landscape, and cannot find its path through the sample. Conduction is only possible when the Fermi energy is close to the LL energy and there are extended paths through the disorder landscape.

However, it is difficult to understand the precisely quantized Hall resistance in the bulk picture above. When the bulk of the 2DEG becomes insulating, edge states exist at the sample boundary which can carry current. The quantization of Hall conductance can be

understood in the Landauer-Buttiker formalism. At bulk filling factor $\nu = n$, the Fermi level crosses with n edge states at the sample boundary. Consider a Hall bar with the source contact at the chemical potential $\delta\mu$ above the drain contact. Each of the edge channels carry current $\delta\mu e^2/h$, leading to the Hall conductivity of $\sigma_{xy} = ne^2/h$. Because the edge states on each side of the Hall bar carries current in the same direction, the edge transport is immune of backscattering with disorder, leading to the precise quantization. Due to the electron-electron interactions, the realistic edge states consists of compressible and incompressible strips [38]. The current is carried mainly be the innermost incompressible strip. This is consistent with experiments measuring the Hall potential distribution across the sample with scanning probe techniques [94, 95].

The zero longitudinal conductivity in the fractional QHE can be understood in the same way as in the integer QHE, because the bulk does not contribute to transport as it is an incompressible liquid with an excitation gap. The Hall conductivity can be understood in the picture of edge transport of quasiparticles in stead of electrons.

3.6 Electron crystals

A 2D electron crystal is pinned by arbitrarily weak disorder. Therefore, if the bulk of a 2DEG forms an electron crystal, the bulk is insulating just as in the QHE. For $\nu < 1/2$, no edge states exist, and the 2DEG is completely insulating, both σ_{xx} and σ_{yy} are close to zero. In most experiments, ρ_{xx} can as high as in the MΩ regime and ρ_{xy} is close to the classical value (after admixture from ρ_{xx} is removed) [96]. For $\nu > 1/2$, edge states exist, and transport is contributed by the edge states. ρ_{xx} are observed to be zero, and ρ_{xy} are the same to its closest integer QHE, also known as reentrant integer QHE.

3.7 Stripes

3.7.1 Microscopic models

Although the prediction of stripes at high LLs [4, 5] is one of the few examples in quantum Hall system that theory goes ahead of experimental discovery, the most striking experimental findings came as the significant transport anisotropy which was not expected. The original theory [5] recognized that both the stripe and bubble phases can be pinned by

disorder at low temperatures and becomes insulating; conduction only happens at exactly $\nu^* = 1/2$ where the bulk edge states between regions of different filling factors percolate through the sample. A few more theoretical works are done after the experimental discovery suggesting the long-range orientational order. Macdonald and Fisher (MF) [97] studied the transport in perfect unidirectional stripe phases with gapless edge states. Like in Fogler et al, it is assumed that the stripe phase itself is pinned by disorder and immobile. The quasiparticles travel along the edges in the direction decided by the edge chiralities, similar to the chiral edge states at the sample boundary in the integer QH states. Unlike the QH edges which are separated by the sample width, here the edges of different charalities are separated by electron or hole strips and backscatterings are possible between neighboring edges. The back scatterings are characterized by the scattering times τ_e and τ_h (across electron or hole stripes respectively), which are presumably dependent on the width of the strips. For stripes along $\hat{x}$ direction, the conductivities are calculated as,

$$\sigma_{xx} = \frac{e^2}{h}\frac{a^{-1}}{l_e^{-1}+l_h^{-1}}\,, \sigma_{yy} = \frac{e^2}{h}\frac{a}{l_e+l_h}\,, \sigma_{xy} = \frac{e^2}{h}([\nu] + \frac{l_e}{l_e+l_h})\,, \tag{3.35}$$

where l_e and l_h are the quasi-particle mean-free paths along neighboring edges. At $\nu^* = 1/2$ where $l_e = l_h$, $\sigma_{xx}/\sigma_{yy} = l_e^2/a^2 \gg 1$ and $\sigma_{xx}/\sigma_{yy} = (e^2/2h)^2$. And the resistivities follows as,

$$\rho_{xx} = \frac{h}{e^2}\frac{a}{l_e([\nu]+1)^2 + l_h[\nu]^2}\,, \rho_{yy} = \frac{h}{e^2}\frac{a^{-1}}{l_e^{-1}[\nu]^2 + l_h^{-1}([\nu]+1)^2}\,, \rho_{xy} = \frac{h}{e^2}\frac{([\nu]+1)l_e + [\nu]l_h}{l_e([\nu]+1)^2 + l_h[\nu]^2}\,. \tag{3.36}$$

A more realistic model considering the presence of topological and orientational defects such as dislocations and grain boundaries were developed [98]. It was found that under this condition the semicircle law is still satisfied,

$$\sigma_{xx}\sigma_{yy} + (\sigma_{xy} - \sigma_0)^2 = (e^2/2h)^2\,. \tag{3.37}$$

MF also evaluated the scattering times in a renormalization-group scheme, and found that $\tau_{e,h}$ increases with decreasing temperature. This is due to the strong coupling between the 1D edges which can be considered as Luttinger liquid, and increasing temperature could suppress the strong coupling and thus inter-edge scatterings. Therefore, with dropping temperature, the easy resistivity increases while the hard resistivity decreases. This is in contrast to most experimental data for temperatures just below an isotropic-anisotropic

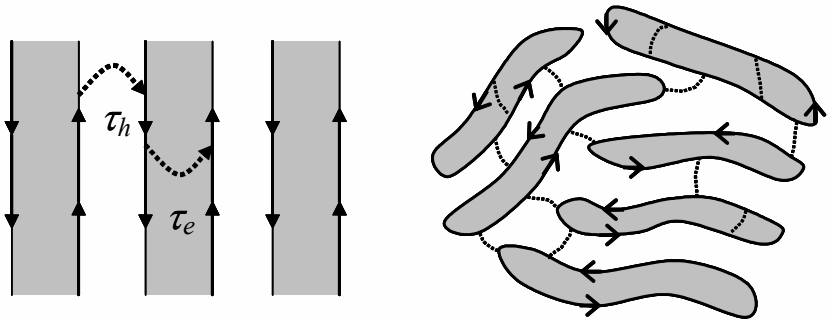

Figure 3.2: Illustration of transport based on the model assuming (left) perfect unidirectional stripes (right) the presence of topological defects. The dark region illustrates the electron region of filling factor $[\nu]+1$ and white for the hole region of filling factor $[\nu]$. [Adopted from thesis of K. B. Cooper]

transition. Indeed, the resistivity has to rise with dropping temperature to become the hard one from an isotropic phase. Positive $dR_{hard}(T)/dT$ has been recently observed at low T, separated from a regime of negative $dR_{hard}(T)/dT$ by a resistance maximum at an intermediate temperature. This observation might suggest the validity of the MF picture in describing stripe transport in the low-T regime. At higher T where the edges are no longer well-defined objects due to thermal fluctuations, a transport theory is not developed. It has been speculated [99] that, in this regime, the stripes may be depinned by an arbitrarily small electric field and a global sliding of the electron liquid becomes possible. Unlike in the bubble phases, no signatures of electric field-driven depinning have been observed for the stripe phases so far.

3.7.2 Conversion between resistance and resistivity

Soon after the experimental report of stripes, it was recognized that the resistance anisotropy measured in Van der Pauw samples, exponentially exaggerate the microscopic resistivity anisotropy. This is because of the current channeling effect in an anisotropic system. In typical Van der Pauw measurements, the current is sent between two contacts on the two opposite sides of the sample, and the voltage is measured between two corner contacts in the same direction. Along the stripe direction, the current is strongly collimated in the center

of the sample and does not spread out; the current density along the sample boundary is exponentially small, and the "easy resistance" is thus exponentially suppressed. On the other hand, if current is sent across the stripes, it is more spread out; sufficient current flows along the boundary and one measures a considerable voltage drop. It was calculated by Simon [100] that,

$$R_{xx} = \frac{4}{\pi}\sqrt{\rho_{xx}\rho_{yy}} \sum_{n=odd} \left[n \sinh(\sqrt{\frac{\rho_{yy}}{\rho_{xx}}}\frac{\pi n}{2}\frac{L_y}{L_x}\right]^{-1} \tag{3.38}$$

$$\approx (L_x/L_y)\rho_{xx} - C\sqrt{\rho_{xx}\rho_{yy}}\,, L_x^2\rho_{xx} > L_y^2\rho_{yy} \tag{3.39}$$

$$\approx \frac{8}{\pi}\sqrt{\rho_{yy}\rho_{xx}}e^{-[\pi L_y/2L_x]\sqrt{\rho_{yy}/\rho_{xx}}}\,, L_x^2\rho_{xx} < L_y^2\rho_{yy}\,, \tag{3.40}$$

where $C \approx 0.44$. In typical high-quality Van der Pauw sample, R_{easy} is usually difficult to be distinguished from zero, so the conversion from resistance and resistivity is not feasible. Nevertheless, exploiting the relation $\rho_{xx}\rho_{yy} = \text{const.}$ at half-filling from MF theory, one can make an estimate from the hard resistance. For example, for $\nu = 9/2$, a hard resistance $R_{yy} = 2\text{k}\Omega$ gives $\rho_{yy} \approx 2.3\text{k}\Omega$, $\rho_{xx} \approx 0.18\text{k}\Omega$, $\rho_{yy}/\rho_{xx} \approx 13$, which in turn would give R_{xx} too small to be measured. In Hall bar samples, where $L_x \gg L_y$, the exaggeration due to the current channeling effect is much smaller.

Even when the current channeling effect is taken care of, the comparison between the measured resistance and microscopic models still needs further caution. All the microscopic models consider the bulk conductivity; on the other hand, edge transport at the sample boundary which involves all the filled LLs are always in place. The transport properties of bulk stripes would decide the measured resistance, only when reasonable equilibration between the boundary bulk edge states and bulk conducting channels. However, this equilibration may fail [101], especially at low temperatures.

Part II

Experiments on stripes and bubbles

Chapter 4

Stripe orientation under $B_{\|}$

Shortly after the experimental discovery of stripes [6, 7], it was found that the application of an in-plane magnetic field $B_{\|}$ can induce reorientation of stripes, signatured by the switching of high and low resistances [11, 12]. In these early experiments [11, 12], it was consistently found and concluded that $B_{\|}$ tends to align stripes perpendicular to it. This also applies for half-integer filing factors in the $N = 1$ LL, where stripes can be induced by $B_{\|}$, whereas FQHS are the ground state in a perpendicular field. Theoretical considerations [102, 103] after the experiments, explains the effects of $B_{\|}$ on the stripe orientation as an orbital effect. In other words, in the presence of $B_{\|}$, the quantum confinement potential $V(z)$ can no longer be separated from the single-particle Shrodinger equation; $B_{\|}$ couples the 2D cyclotron and electric subband levels. This mixing modifies the interaction between electrons and thus the cohesive energy of stripe phases, and result in an energy difference in stripes perpendicular and parallel to $B_{\|}$. Calculations [102, 103] gave results consistent with the experimental observations, that stripes perpendicular to $B_{\|}$ are more favorable. While Jungwirth *et al.* [102] further extends this conclusion to apply to any single-subband system, Stanescu *et al.* [103] points out that stripes parallel to $B_{\|}$ could be favored when the thickness of the 2DEG is large. On the other hand, while it is well known that the g-factor of GaAs 2DEG is decided by the total (rather than only perpendicular) magnetic field, it was understood that the spin degree of freedom doesn't play a major role here. Indeed, none of the theoretical calculations above distinguishes between different spin branches when the same LL is considered.

We have studied the $B_{\|}$-induced reorientation of stripes and have established a phase diagram of stripe orientation with respect to $B_{\|}$ sensitive to a number of parameters, including carrier density, spin index, partial filling factor of a certain LL and the magnitude of $B_{\|}$. Through this chapter, we define $\hat{x} \equiv \langle 1\bar{1}0 \rangle$ and $\hat{y} \equiv \langle 110 \rangle$ for simplicity. We focus on data from sample A1 unless otherwise noted in this chapter. Observations in different samples are also discussed.

4.1 Multiple reorientations of stripes induced by $B_{\|}$

4.1.1 Stripes parallel to $B_{\|}$

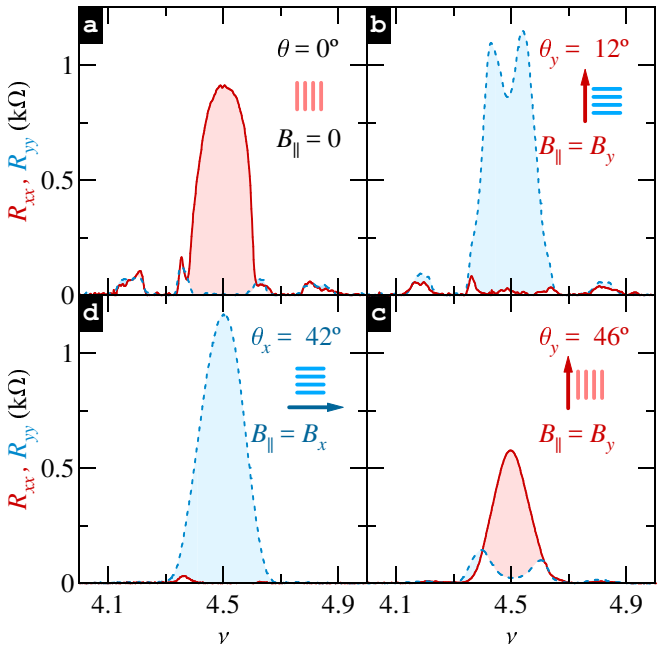

Figure 4.1: R_{xx} (solid line) and R_{yy} (dotted line) versus ν at (a) $\theta = 0°$, (b) $B_{\|} = B_y$ and $\theta_y = 12°$, (c) $B_{\|} = B_y$ and $\theta_y = 46°$, and (d) $B_{\|} = B_x$ and $\theta_x = 42°$.

In Fig. 4.1(a) we present an example of stripes in perpendicular magnetic field near $\nu = 9/2$, characterized by $R_{xx} \gg R_{yy}$, indicating stripes oriented along $\hat{y}$ direction. When $B_{\|}$ is applied parallel to the native stripes ($B_{\|} = B_y$), at $\theta_y = 12°$ stripes reorient along $\hat{x}$-direction (perpendicular to $B_{\|}$), as anticipated [see Fig. 4.1(b)]. Surprisingly, upon further increase of B_y, at $\theta_y = 46°$ stripes are reoriented again, back to their native direction and

are now aligned *parallel* to $B_\parallel$ [see Fig. 4.1(c)]. When $B_\parallel$ is applied perpendicular to the native stripes ($B_\parallel = B_x$), at $\theta_x = 42°$ stripes are reoriented along $\hat{x}$-direction, again aligning *parallel* to $B_\parallel$ [see Fig. 4.1(d)]. We thus conclude that, regardless of the orientation of $B_\parallel$, a large enough $B_\parallel$ align stripes *parallel* to it.

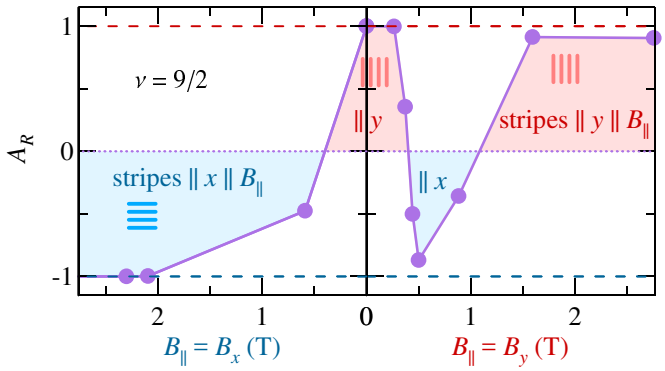

Figure 4.2: Resistance anisotropy $A_R \equiv (R_{xx} - R_{yy})/(R_{xx} + R_{yy})$ as a function of $B_\parallel = B_x$ (left) and $B_\parallel = B_y$ (right) at $\nu = 9/2$. The inset shows the stripes orientation and the direction of $B_\parallel$.

Figure 4.2 shows the resistance anisotropy $A_R \equiv (R_{xx} - R_{yy})/(R_{xx} + R_{yy})$ vs B_x (left panel) and B_y (right panel). Starting from $A_R \approx 1$, with increasing B_y, A_R vanishes at $B_y \approx 0.4$ T, reaches $A_R \approx -1$, turns around, disappears again at $B_y \approx 1.1$ T, and finally returns to $A_R \approx 1$. With increasing B_x, A_R vanishes at $B_x \approx 0.4$ T and then approaches $A_R \approx -1$. Taken together, the data above clearly demonstrate that the effect of $B_\parallel$ is non-monotonic, and that a second type of reorientation favors stripes parallel to $B_\parallel$. As we show next, the second type of reorientation is relevant at other filling factors as well, and it shows sensitivity to both the spin index σ and the Landau level index N.

4.1.2 Dependence on spin and LL index

Figure 4.3 shows the phase diagram of stripe orientations at $\nu = 9/2$, $11/2$, $13/2$ and $15/2$ for (a) $B_\parallel = B_y$ and (b) $B_\parallel = B_x$. The regions representing stripes along $\hat{y}$ ($\hat{x}$), marked by vertical (horizontal) lines, are demarcated by the characteristic fields (circles) where $A_R \approx 0$. We define B_c as the field at which stripes reorient perpendicular to B_y, and $B'_{c,x}$ ($B'_{c,y}$) as the field at which stripes reorient parallel to B_x (B_y). The dashed lines represent $B_\parallel$ at select tilt angles and the resistances at these angles are shown in Fig. 4.3(c) and (d).

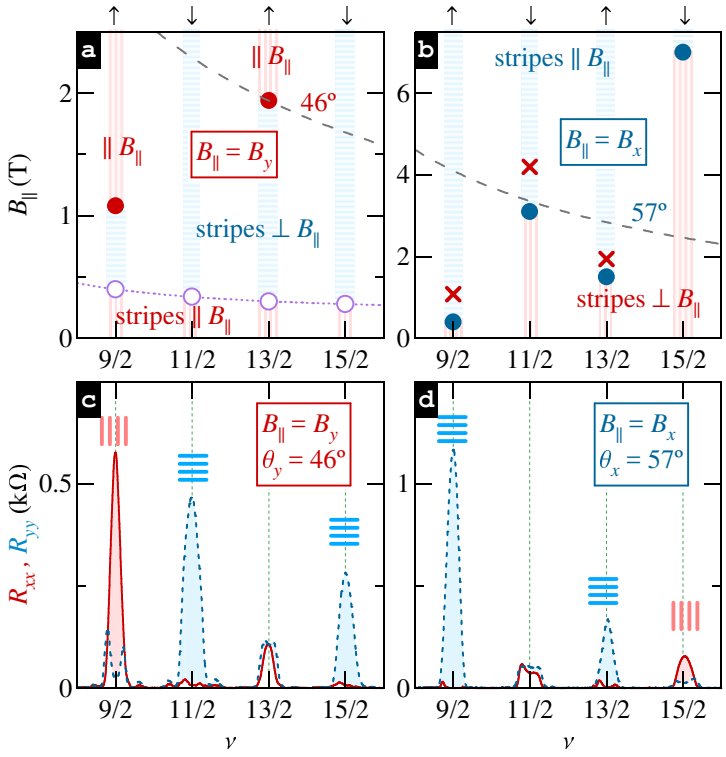

Figure 4.3: Evolution of stripe orientation at $\nu = 9/2$, $11/2$, $13/2$ and $15/2$ for (a) $B_{\parallel} = B_y$ and (b) $B_{\parallel} = B_x$. The regions with vertical (horizontal) lines represent stripes along $\hat{y}$ ($\hat{x}$), demarcated by the characteristic fields B_{1y} (open dots), B_{2x} [panel (b)] and B_{2y} [panel (a)] (solid dots). For comparison, B_{2y} (crosses) are added to panel (b) at $\nu = 9/2$ and $13/2$. Dashed lines represent $B_{\parallel}$ at marked tilt angles. R_{xx} (solid line) and R_{yy} (dotted line) vs ν at (c) $\theta_y = 46°$ and (d) $\theta_x = 57°$.

First, we notice that both $B'_{c,x}$ and $B'_{c,y}$ increase with N for a given σ while B_c decreases with N. Second, strong sensitivity to σ renders the overall dependencies of $B'_{c,x}$ and $B'_{c,y}$ on ν non-monotonic; indeed, both $B'_{c,x}$ and $B'_{c,y}$ are always considerably smaller for $\sigma = +1/2$ than $\sigma = -1/2$.

The sensitivity of $B'_{c,x}$ and $B'_{c,y}$ to σ and N is also evident in the raw data presented in Fig. 4.3(c) and (d). For $B_{\parallel} = B_y$ and $\theta_y = 46°$ [see Fig. 4.3(c)], the stripes at $\nu = 9/2$ have reoriented back to their native direction (along $\hat{y}$ axis) as manifested by $R_{xx} \gg R_{yy}$. The data at $\nu = 13/2$ suggest that the (second) reorientation is about to happen at this filling factor as well. However, stripes at $\nu = 11/5$ and $15/2$ are still oriented along $\hat{x}$ direction, as $R_{xx} \ll R_{yy}$. For $B_{\parallel} = B_x$ and $\theta_x = 57°$ [see Fig. 4.3(d)], stripes both at $\nu = 9/2$ and $13/2$

have reoriented along $\hat{x}$ axis, stripes at $\nu = 11/2$ are undergoing the reorientation, while stripes at $\nu = 15/2$ are still oriented along $\hat{y}$ direction.

To compare the magnitudes of $B'_{c,x}$ and $B'_{c,y}$ we add $B'_{c,y}$ (crosses) to Fig. 4.3(b) and observe that $B'_{c,y}$ is close to $B'_{c,x}$, though slightly larger. Combined with qualitatively identical dependence on σ and N, this observation suggests that the reorientations characterized by $B'_{c,x}$ and $B'_{c,y}$ are of the same origin.[1] We can now summarize the reorientations as of two types. The first type, which aligns stripes perpendicular to $B_\parallel$, is characterized by B_c that is not sensitive to σ and slightly decreases with N. The second type aligns stripes parallel to $B_\parallel$, is characterized by $B'_{c,x}$ and $B'_{c,y}$ that are sensitive to σ and increase with N. The data at $\nu = 9/2$ also suggest that the mechanism responsible for reorientation of the first (second) type dominates at lower (higher) $B_\parallel$.

4.1.3 Possible coupling between native and $B_\parallel$-induced orienting mechanism

The stripe orientation under $B_\parallel$ was understood as the competition between the $B_\parallel$-induced and native symmetry-breaking potential (SBP). Quantitatively, one can define the native anisotropy energy as $E_N = E_{N,x} - E_{N,y}$, where $E_{N,x}$ and $E_{N,y}$ is the energy of native stripes along $\hat{x}$ and $\hat{y}$ direction, respectively. For the most well-known case of stripes along $\hat{y}$, E_N is positive. One can also define the $B_\parallel$ induced anisotropy energy as $E_B = E_\perp - E_\parallel$, where $E_\perp$ and $E_\parallel$ is the energy of stripes perpendicular and parallel to $B_\parallel$, respctively. In the standard picture from early studies, E_B was understood to be negative for a single-subband case, and what's more, it was assumed that E_N and E_B are additive, giving the total anisotropy $E = E_x - E_y = E_N + E_B$ for $B_\parallel = B_y$, and $E = E_N - E_B$ for $B_\parallel = B_x$. The positive (negative) sign of the total anisotropy energy E is reflected in stripes along $\hat{x}$ ($\hat{y}$). The $B_\parallel$-induced anisotropy energy E_B calculated at the reorientation field $B_y = B_c$, or $E = 0$, is routinely used as a measure of the native anisotropy energy E_N, which was estimated to be on the order of 1 mK per electron.

We now examine the picture above in light of our observation of multiple reorientations induced by $B_\parallel$. The resistance anisotropy A plotted in Fig. 4.2 suggested E should have a qualitatively similar N-shape as a function of $B_\parallel$, which crosses zero 3 times. Again, this unambiguously demonstrate that E_B is non-monotonic and can change sign. What's more,

[1] In later discussions we call both $B'_{c,x}$ and $B'_{c,y}$ as B'_c.

observation of both $B'_{c,x}$ and $B'_{c,y}$ allows us to examine the symmetry of E_B for $B_\parallel = B_x$ vs $B_\parallel = B_y$, which was not possible before with only B_c available. If we assume that E_B, is the same for $B_\parallel$ applied along $\hat{x}$ or $\hat{y}$ directions, one would expect, in the absence of native orienting potential, $B'_{c,x} = B'_{c,y}$ at a given ν, illustrated by the dotted curve in Fig. 4.4 (in the figure the effect of $B_\parallel$ is denoted as E_A, i.e., $E_A = E_B$ for $B_\parallel = B_y$ and $E_A = -E_B$ for $B_\parallel = B_x$); a native mechanism favoring stripes along $\hat{y}$ direction, or in other words a positive E_N that is additive to E_B, would then lead to $B'_{c,x} > B'_{c,y}$, as illustrated by the solid curve in Fig. 4.4. In contrast, our data show exactly the opposite, e.g., $B'_{c,y} > B'_{c,x}$ at all filling factors $\nu = 9/2$, $11/2$ and $13/2$, and at $\nu = 9/2$, $B'_{c,y} \approx 1.0$ T is considerably larger than $B_{2x} \approx 0.4$ T. We thus conclude that E_B must depend on the direction of $B_\parallel$, or that E_N cannot be simply added to E_B. In other words, our data suggest possible coupling of $B_\parallel$ to native SBP. Furthermore, it seems that a horizontal shift of solid curve of $E_B(B_\parallel)$ in Fig. 4.4, rather than a vertical one, can result in $B'_{c,x}$ ¡ $B'_{c,y}$, qualitatively consistent with our data. A horizontal shift of $E_B(B_\parallel)$ to account for that native SBP, would be reasonable in a scenario that the native SBP acts like an effective $B_\parallel$, e.g., it induces deformation of electron wavefunctions favoring a certain stripe orientation, and the $B_\parallel$ makes further deformation of the electron wavefunction on this basis. We'll come back to this point in Sec. 4.2.4 and Sec. 4.4.

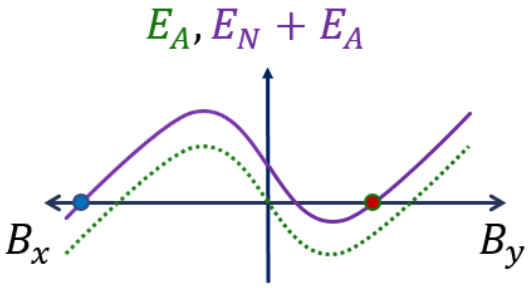

Figure 4.4: Anisotropy energy E_A in the absence of native SBP (dotted curve) and $E_N \pm E_A$ (solid curve) in the presence of the native SBP, as a function of B_x to the left and B_y to the right. $E_A = E_B$ for $B_\parallel = B_y$ and $E_A = -E_B$ for $B_\parallel = B_x$. The circles where the curves crosses zero mark the reorientation fields.

4.1.4 Temperature dependence of stripes parallel and perpendicular to $B_{\|}$

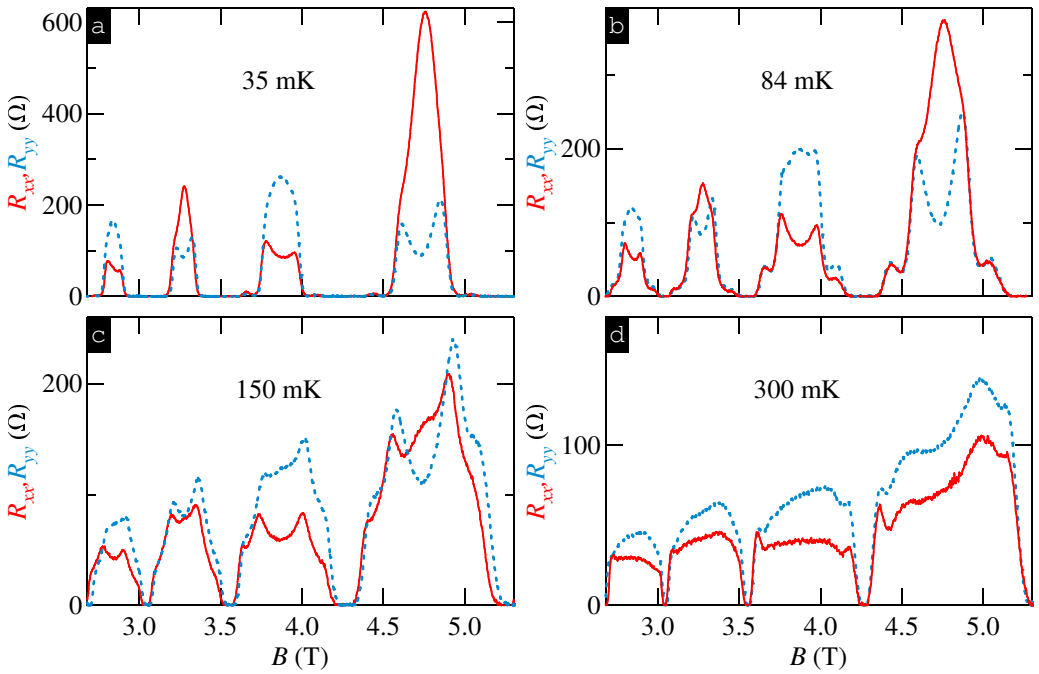

Figure 4.5: Resistances R_{xx} (solid) and R_{yy} (open) as a function of total B at different temperatures, as marked, under tilt angle $\theta \approx 56°$ and $B_{\|} = B_y$.

It is a curious question whether or not the stripes parallel and perpendicular to $B_{\|}$ have similar properties, e.g., if they follow similar temperature dependence. In addition, if the two types of reorientations induced by $B_{\|}$ are due to different mechanisms and if the two mechanisms have different temperature dependence, one might observe a switch of stripe orientation with respect to $B_{\|}$ as the temperature is changed. With this motivation, we have studied the temperature dependence of stripes at a tilt angle $\theta \approx 56°$ where different stripe orientations are observed at different spin indices. In Fig. 4.5 we present the resistances R_{xx} and R_{yy} at different temperatures at this angle, covering filling factor from 4 to 8. Alternating stripe orientation as one moves from one LL to another is clear at $T \approx 35$ mK in Fig. 4.5(a), with stripes along $\hat{y}$ for the lower spin branch ($\nu = 9/2$ and $13/2$) and stripes along $\hat{x}$ for the upper one ($\nu = 11/2$ and $15/2$). As temperature is raised, the anisotropy at all filling factors gets weaker, and stripes have disappeared at $T = 300$ mK with some

weak residual anisotropy. In Fig. 4.6 we present R_{xx} and R_{yy} vs T at four filling factors ν = 9/2, 11/2, 13/2 and 15/2, as marked. In short, the stripes of different orientations with respect to $B_{\|}$ seem to follow similar temperature dependence. Nevertheless, we comment on the following points. First, stripes perpendicular to $B_{\|}$ at $\nu = 11/2$ and 15/2, have the anisotropy spanning a larger filling factor range, and the resistance extrema less sharper; the easy resistance decreases with increasing temperature. Second, it has been pointed out in early studies [104] that $B_{\|}$, which always align stripes perpendicular to it, can raise the onset temperature of stripes and make the anisotropy survive temperatures as high as 600 mK in contrast to about 100 mK in pure perpendicular fields. This observation was taken as an evidence of randomly aligned stripe domains above the anisotropy onset temperature in pure perpendicular fields, and the effect of $B_{\|}$ is to align them resulting in the anisotropy. If the anisotropy in our data, which has the sign consistent as in [104], indeed represents weakly aligned stripe domains, then we must conclude that the mechanism that favors stripes parallel to it, has dies out at this temperature. However, we cannot make this conclusion because it is not clear whether the weak residual anisotropy at $T = 300$ mK is due to pure geometry and disorder effects without the presence of stripe domains. We do observe in another set of data that the anisotropy at 300 mK becomes weaker at 600 mK, consistent with the scenario in [104]. Still, more careful studies are needed to make a solid conclusion.

4.1.5 Even more reorientations

In all the data above, we are limited to moderate magnetic fields lower than 8 T. The reason is that, in our early experiments, we usually observe that as higher $B_{\|}$ is approached, resistances along both directions show maxima around half-filling, and it is difficult to decide whether stripes still exist or not. Although a complete understanding is missing, disappearance of stripes at very high $B_{\|}$ is not too surprising to anticipate, as the $B_{\|}$ not only introduces strong mixing between LLs, but also pushes the electrons against the interface resulting in a stronger effect of interface disorder. Indeed, it is common to observe degradation of interesting phases at very high $B_{\|}$, including FQHE, bubble phases, MIRO, etc. Nevertheless, in later experiments, we have observed significant transport anisotropy at high $B_{\|}$ with resistance along the easy direction showing a minimum around half-filling, providing strong evidence for the existence of stripes, which must have undergone a third

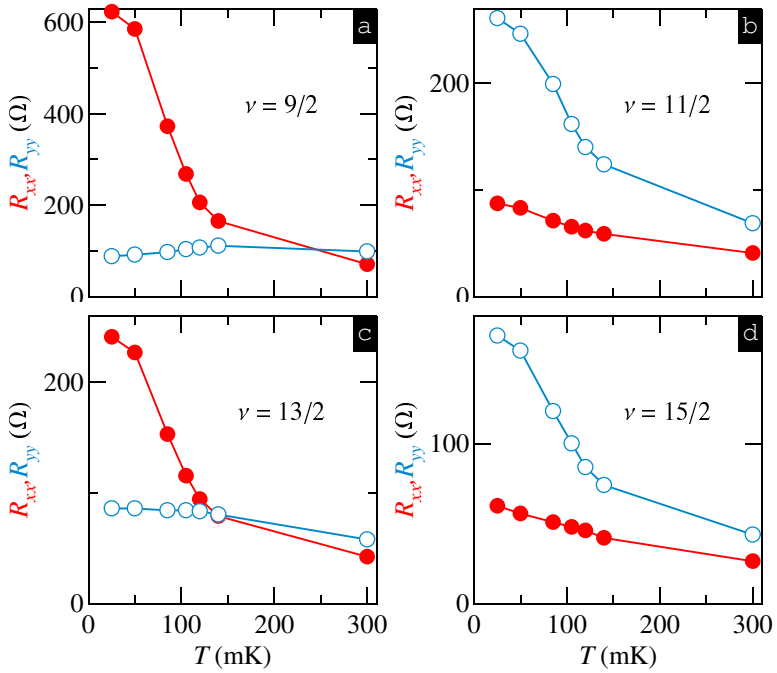

Figure 4.6: Resistances R_{xx} and R_{yy} as a function of T at $\nu = 9/2$, 11/2, 13/2 and 15/2, under tilt angle $\theta \approx 56^\circ$ and $B_\parallel = B_y$.

reorientation with increasing $B_\parallel$. In Fig. 4.7 we plot the reorientation behavior of sample A1 with $B_\parallel$ applied along native stripes at $\nu = 9/2$ in sample A1. Fig. 4.7(a) and (b) displays the resistances R_{xx} and R_{yy}, and the resistance anisotropy $A_R \equiv (R_{xx} - R_{yy})/(R_{xx} + R_{yy})$, respectively. Remarkably, just by changing the magnitude of B_y, we reorient stripes a total of 3 times, with A_R oscillating and crossing zero 3 times, at roughly 0.4 T, 1.2 T and 8.5 T. It is interesting to notice that the slope of A_R at these reorientation fields decreases with increasing $B_\parallel$.

4.1.6 Discussion

Multiple reorientations induced by $B_\parallel$ have been observed in almost all samples we have studied. The sensitivity to spin and LL indices proves to be robust. However, we do observe different classes of reorientation behaviors in different samples. For example, for $\nu = 9/2$ and $B_\parallel = B_y$ [2] , some samples show two reorientations under increasing B_y (sample A1,

[2] Here we also limit ourselves to not too large $B_\parallel$, $B_\parallel < 8$ T so the case as in 4.1.5 is not considered

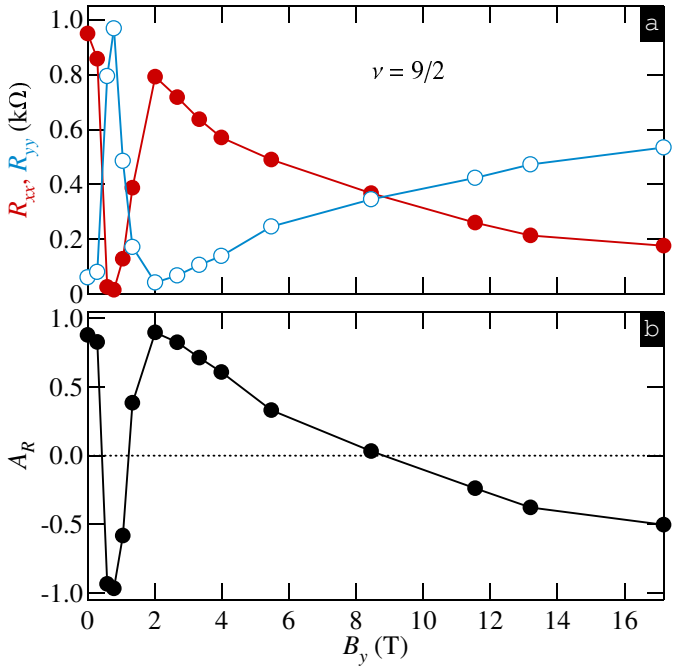

Figure 4.7: (a) Resistances R_{xx} and R_{yy} and (b) the resistance anisotropy A_R as a function of $B_{\|} = B_y$ at $\nu = 9/2$ in sample A1.

B1, N1), some samples show no reorientation at all and stripes always stay parallel to $B_{\|}$ (sample A2, A6, M1, M2), and some samples show only one reorientation resulting in stripes perpendicular to $B_{\|}$ (sample A4), consistent with the result of early studies (also see 6.2 for more details). The contrast between different samples had led to the dis-encouraging thought that the stripe orientation under $B_{\|}$ is a messy problem. It motivated us to look at the stripe reorientation behaviors in a sample with an in-situ back gate as a knob. It turned out that the distinguished reorientation behaviors can be unified by just tuning one parameter as we discuss in the next section.

4.2 The effects of density on stripe orientation

As we show in this section, the distinguished reorientation behavior in different individual samples can be unified in a single device, by tuning the carrier density with an *in situ* back gate.

Our 2DEG resides in a 30-nm GaAs/AlGaAs quantum well (about 200 nm below the

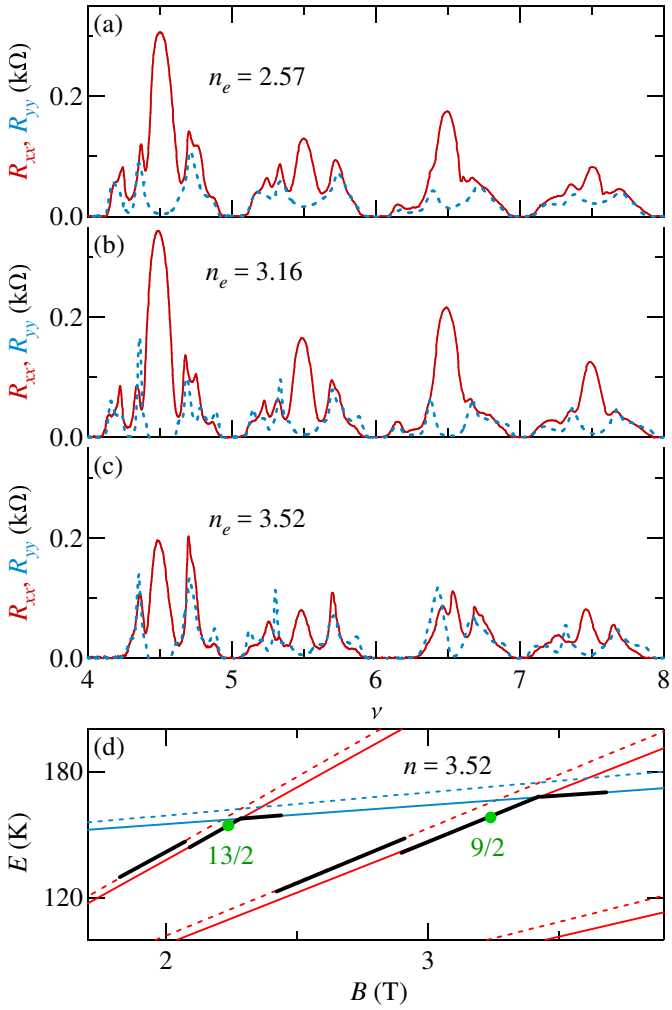

Figure 4.8: Longitudinal resistances R_{xx} (red) and R_{yy} vs ν at different densities, as marked. (d) LL diagram close to the Fermi level for $n_e = 3.52 \times 10^{11}$ cm^{-2}.

sample surface) that is doped in a 2 nm GaAs quantum well at a setback of 63 nm. The *in situ* gate consists of an n^+ GaAs layer situated 850 nm below the bottom of the quantum well [105]. Eight Ohmic contacts were fabricated at the corners and midsides of the lithographically-defined 1×1 mm^2 Van der Pauw mesa. The electron density n_e was varied continuously from 2.2 to 3.8×10^{11} cm^{-2}. The peak mobility was about $\mu \approx 1.2 \times 10^7$ cm^2/Vs at $n_e \approx 3.3 \times 10^{11}$ cm^{-2}.

Examples of resistances in perpendicular fields at different densities are shown in Fig. 4.8 in the filling factor range $\nu = 4 \sim 8$. In the whole density range explored, native stripes

always appear along $\hat{y} = \langle 110 \rangle$ direction, that is, the easy transport direction is along $\hat{y}$, signaled by much larger R_{xx} than R_{yy}. Most magnetoresistance features changes only slightly from $n = 2.57$ to 3.16×10^{11} cm^{-2}. For $n = 3.52 \times 10^{11}$ cm^{-2}, the quantum Hall plateau at $\nu = 4$ and 6 has become wider, and stripes barely survive at $\nu = 13/2$. This is a result of population of the second subband at these filling factors, as we illustrate in Fig. 4.8(d). In Fig. 4.8(d) we schematically plot the level diagram at $n = 3.52 \times 10^{11}$ cm^{-2}, where red (blue) lines represent LLs from the first (second) subband, and solid (dashed) lines represent the spin up (down) branch. The Fermi level for $\nu = 4 \sim 8$ are marked by black segments, with 9/2 and 13/2 marked by green dots. At range of filling factors $4 < \nu < 4.5$ and $6 < \nu < 6.5$ are in the second subband while the spin down branch are below the second subband. At even higher density, the Fermi levels at $\nu = 9/2$ and 13/2 are in the second subband and stripes disappear in a perpendicular magnetic field.

4.2.1 Main results - Stripe orientation under $B_{\parallel} = B_y$ at $\nu = 9/2$

In Fig. 4.9 we summarize our experimental findings at $\nu = 9/2$, namely the phase diagram of stripe orientation in the (n_e, B_y)-plane. The diagram contains two distinct phases, "stripes $\parallel \hat{x}$" and "stripes $\parallel \hat{y}$". While the native stripes are along the $\hat{y}$-axis at all densities studied, one easily identifies three distinct evolutions of stripe orientation with $B_{\parallel}$. At low densities we observe a *single* reorientation ($\hat{y} \rightarrow \hat{x}$), in accord with the "standard picture" [11, 12, 102, 103, 106]. At intermediate densities, the stripes undergo *two* successive reorientations ($\hat{y} \rightarrow \hat{x}$ and $\hat{x} \rightarrow \hat{y}$), ultimately aligning along $B_{\parallel}$ [14]. Finally, the high density regime reveals *no* reorientations whatsoever, and the native direction of the stripes ($\parallel y$) is preserved at all $B_{\parallel}$. While each of these regimes was previously realized in individual samples [11, 12, 60, 68, 14], to our knowledge, it is the first observation of all three classes of behavior in a single device.

Further examination of the phase diagram (Fig. 4.9) shows that the characteristic in-plane field $B_y = B_c$, describing the first ($\hat{y} \rightarrow \hat{x}$) reorientation, is virtually independent of n_e, as revealed by essentially horizontal lower boundary at $B_c \approx 0.25$ T of the "stripes $\parallel \hat{x}$" phase. On the other hand, the in-plane field $B_y = B_c'$, corresponding to the second ($\hat{x} \rightarrow \hat{y}$) reorientation (the upper boundary of the "stripes $\parallel \hat{x}$" phase) decreases sharply with n_e until it merges with B_c at $n_e \approx 3.5 \times 10^{11}$ cm^{-2}. Indeed, B_c' drops by an order of magnitude over a density variation of less than 20 %. It is this steep dependence of B_c' on n_e that is

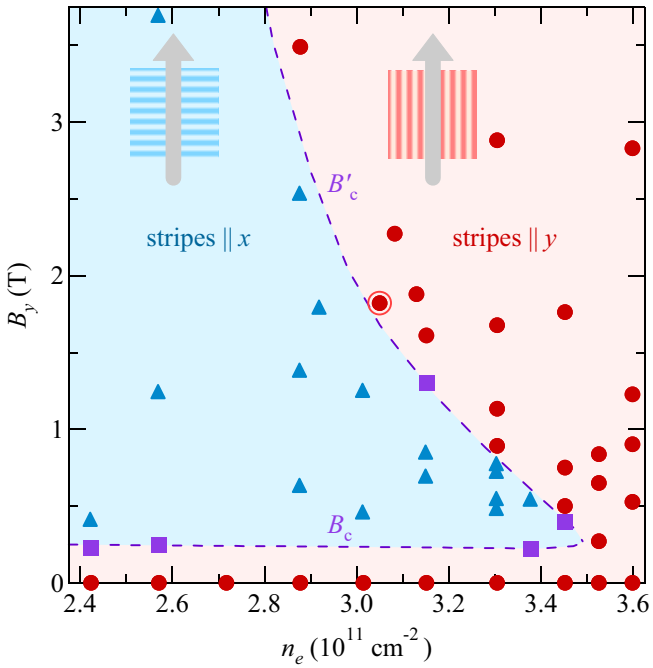

Figure 4.9: Stripe orientation as a function of n_e and B_y at $\nu = 9/2$. Triangles (circles) mark stripe orientation perpendicular (parallel) to $B_\parallel = B_y$. The big circle was obtained from the density sweep in Fig. 4.10. Squares mark the isotropic state. The lower (upper) phase boundary (dashed line) is a guide to the eyes marking $B_\parallel = B_c$ ($B_\parallel = B_c'$), see the text.

responsible for the appearance of the three distinct regimes discussed above.

As pointed out in the last section, where we investigate both B_c and B_c' at fixed n_e, B_c' depends strongly on spin and orbital indices, in sharp contrast to B_c; at $\nu = 11/2$, B_c' is significantly higher than at $\nu = 9/2$. This observation, together with theoretical considerations [102] predicting similar $B_\parallel$-induced anisotropy energies favoring perpendicular stripes at these filling factors, has lead to the conclusion that the second reorientation is of a different origin [14]. The observation of strong (weak) n_e-dependence of B_c' (B_c) lends further support to this notion.

4.2.2 Density dependence of stripe orientation at other filling factors

It has been demonstrated in details in Sec.4.1.2 [14] that two reorientations are observed at other filling factor as well such as $\nu = 11/2$ and $13/2$, and B_c' sensitively depends on the spin and LL index while B_c does not. We observe similar behaviors in the gated sample.

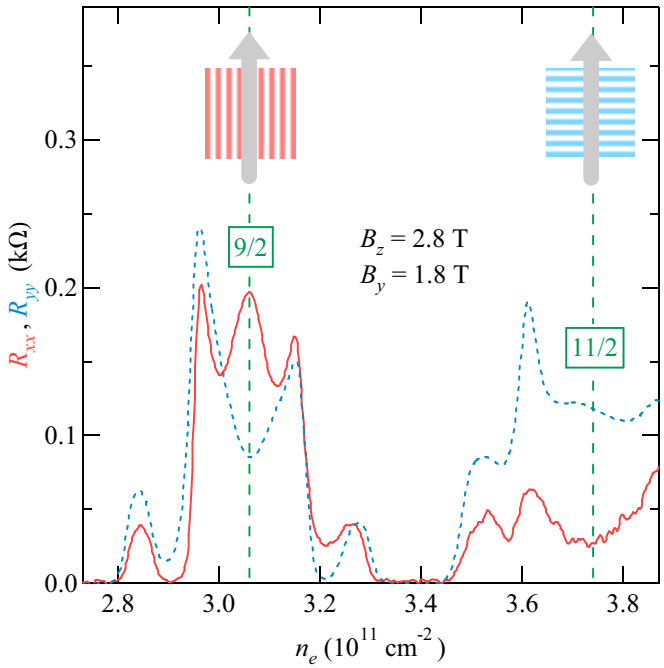

Figure 4.10: R_{xx} and R_{yy} vs. n_e measured at $B_z = 2.8$ T and $B_y = 1.8$ T.

Consistent with Sec.4.1.2 [14], for fixed density, $n = 3.30\times10^{11}$ cm^{-2} as shown in Fig. 8.3(a), B_c' is smaller at spin up branch ($\nu = 9/2$ and $13/2$), and slightly increases with LL index although the dependence is weaker, demonstrating non-monotonic behavior as a function of ν or B_z. On the other hand, for higher density, $n = 3.52\times10^{11}$ cm^{-2}, where stripe parallel to $B_\parallel$ prevail without any reorientations, reorientations leading to perpendicular stripes do appear at other filling factors. In short, at other ν such as $11/2$ or $13/2$, B_c' is larger than that at $9/2$, while B_c is almost the same. As a result, at these filling factors we do not observe the high density regime behavior as at $9/2$, where no reorientations are observed. Nevertheless, it holds true that at each fixed filling factor, B_c' decreases with increasing density and stripes parallel to in-plane fields are more favorable.

4.2.3 How to understand the role of density on stripe orientation?

Listing all possibilities – The phase diagram (Fig. 4.9) implies that it is not $B_\parallel$ alone, but rather its combination with the carrier density that determines stripe orientation. In particular, it indicates that at higher n_e stripes are more likely to be oriented parallel to $B_\parallel$, which is also their native orientation. There are a few effects which can be directly ascribed

to the density change at a given filling factor (here, $\nu = 9/2$). First, the perpendicular field B_z increases with n_e. This fact alone leads to (i) a smaller stripe period, (ii) a weaker inter-LL screening [30],[3] and (iii) a closer proximity of the valence LL to the second subband. Second, the increase in n_e results in a smaller inter-subband splitting [which further facilitates (iii)]. Finally, with increasing gate voltage electrons are pressed towards the interface and thus experience stronger interface potential, which, e.g., might affect coupling to the native symmetry breaking field.

Exclusion of the quantum confinement potential as responsible for the phase diagram – To single out the dominant effect, we have measured R_{xx} and R_{yy} at a fixed $B_z = 2.8$ T and $B_y = 1.8$ T while sweeping the gate voltage to cover the filling factors $\nu = 9/2$ and $11/2$. The results of these measurements are presented in Fig. 4.10 showing R_{xx} (solid line) and R_{yy} (dotted line) as a function of n_e. At $\nu = 9/2$, which occurs at a lower density, $R_{xx} > R_{yy}$ and stripes are parallel to $\hat{y}$, as a result of the second reorientation. In contrast, at $\nu = 11/2$, which is at a higher density, we find $R_{xx} < R_{yy}$ implying stripes still perpendicular to $B_\parallel$. We note that $\nu = 9/2$ and $11/2$ are characterized by the same 2D wavefunction, stripe period, and inter-LL spacing, justifying their direct comparison in Fig. 4.10. At first glance, this finding might appear puzzling as it indicates that the overall trend observed in Fig. 4.9, namely that higher n_e favors stripes parallel to $B_\parallel$, is completely reversed by simply changing the spin index.

The contrasting behavior in Fig. 4.9 (at fixed ν) and Fig. 4.10 (at fixed B), allows us to rule out the factors that works the same way in both situations to be responsible for the phase diagram in Fig. 4.9. These factors include the interaction with the interface potential, which was considered in [68] as the reorientation mechanism favoring stripes parallel to $B_\parallel$. Indeed, at fixed B_z and B_y, increasing n_e from $\nu = 9/2$ to $11/2$ could only increase the electron-interface interaction. However, stripe orientation switches from $\hat{y}$ (native direction) at $\nu = 9/2$ to $\hat{x}$ at $\nu = 11/2$, suggesting that this mechanism, even if present, is of secondary importance. Similarly, the data in Fig. 4.10 allow us to conclude that the proximity to the second subband is also not a dominant factor for the $\hat{x} \to \hat{y}$ transition (at fixed $B_\parallel$) seen in Fig. 4.9. If the opposite were true, $\nu = 11/2$ in Fig. 4.9 would reveal stripes along $\hat{y}$ since it is closer to the second subband than $9/2$, as already discussed.

[3] Screening at a wavevector of stripe modulation is characterized by $\varepsilon(1 + a/\pi a_B)$ where $a_B \approx 10$ nm is the Bohr radius [30, 4, 54].

One possible character: the inter-LL screening – On the other hand, what is responsible for the phase diagram in Fig. 4.9 could only be those n_e-associated variations that are present at fixed ν but absent at fixed B. One such effect is screening from other LLs which gets weaker with B_z due to increased inter-LL spacing. While theory always yields $E_A > 0$ in a single-subband 2DEG when screening is taken into account, it does produce $E_A < 0$ when screening is neglected [102]. One can therefore expect stripes parallel to $B_\parallel$ if screening in realistic samples is weaker than calculations suggest [30, 54]. Screening at a wavevector of stripe modulation is characterized by $\varepsilon(1 + a/\pi a_B)$, where $\varepsilon \approx 12.8$ is the dielectric constant of GaAs, $a \approx 2.8R_c$ is the stripe period, R_c is the cyclotron radius, and $a_B \approx 10$ nm is the Bohr radius [30, 4, 54]. While there are other B_z-related effects, $(\hat{x} \to \hat{y})$ stripe reorientation with increasing n_e in Fig. 4.9 can be explained qualitatively by decreasing screening which favors stripes parallel to $B_\parallel$.

In a hand-waving manner, the role of screening on stripe orientation can be understood as follows. First, we recall that stripes form when direct Coulomb repulsion (Hartree) is overwhelmed by the exchange interaction, which is effectively attractive but comes into play only when there exist an overlap between wavefunctions. Since $B_\parallel$ causes the elongation of the wavefunction (cyclotron orbit) along $B_\parallel$, different stripe orientation different degrees of overlap between the wavefunctions. Hartree and Fock term would thus favor different stripe orientations [102]. The competetion between Hartree and Fock can be tuned by screening.

It remains to be understood why stripes parallel to $B_\parallel$ in a single-subband quantum well are never predicted by theories [102] that calculate the dielectric function using the random phase approximation (RPA) [30]. While we cannot point out the exact reason, it appears plausible that such calculations might not accurately capture a real experimental situation. For example, the period of the stripe phase might be different from what Hartree-Fock calculations suggest. Experiments employing surface acoustic waves have obtained about a 30% larger stripe period than suggested by theory [4, 5]. In addition, LL mixing effects beyond the RPA or disorder-induced LL broadening [107] were not taken into account.

Reconsidering the role of quantum well confinement – Now we discuss the reorientation in Fig. 4.10 concerning stripes at different spin branches at the same B. We first discuss the situation in the absence of $B_\parallel$. Different behavior at different spin branches of the same LL is common in many aspects in quantum Hall physics with poor understanding. In most cases, the experimental data are taken in sweeping magnetic fields. Indeed, [108]

explains the spin-index dependence of stripe onset temperature in perpendicular magnetic field as due to different energy scales depending on B. However, this argument would not explain the difference in stripes at fixed B and varying density. In Fig. 4.11 we present the resistance of stripes at different filling factors as a function of the gate voltage in fixed magnetic field. Obviously, the anisotropy is stronger at the lower spin branch, although the difference is less than in field sweeps (similarly, the difference in anisotorpy energy should small in Fig. 4.10, as the anisotropy, in opposite directions, is weak at both filling factors). Similar behavior is observed at different magnetic fields and LLs.

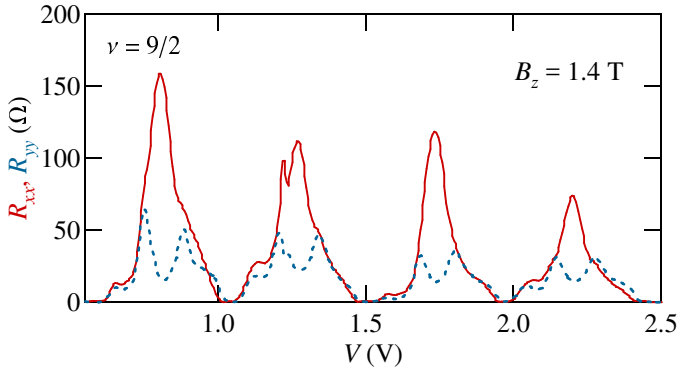

Figure 4.11: R_{xx} (solid) and R_{yy} (dashed) as a function of gate voltage in fixed perpendicular magnetic field $B_z = 1.4$ T, covering ν from 4 to 8.

We note that in the density sweeps at fixed B, the primary change is in the quantum confinement potential. For spin down ($\nu = 11/2$), the gate voltage is higher, and the width of the wavefunction in the z direction is larger than for spin down ($\nu = 9/2$). It is possible that the increase of finite thickness leads to a softening of the Coulomb interaction and thus weakening of stripes. Another possibility is a weaker native anisotropy energy at $\nu = 11/2$ due to an unknown mechanism. If one assumes the anisotropy energy due to $B_{\|}$ is the same in Fig. 4.10, a weaker native anisotropy at $\nu = 11/2$ could lead to the contrasting stripe orientation as shown in Fig. 4.10.

4.2.4 Stripe orientation under $B_{\|} = B_x$

In Fig. 4.12 we plot the phase diagram of stripe orientation at $\nu = 9/2$ at $B_{\|} = B_x$. Reorientation is observed at all densities. The characteristic field needed to induce the reorientation, demonstrate a weak dependence on n_e. $B'_{c,x}$ has a shallow minimum around

$n_e \approx 3.2 \times 10^{11}$ cm^{-2}, increases at lower density, and also a little bit at higher density. Across the whole density range studied, the variation in $B'_{c,x}$ is within 0.5 T. This is in sharp contrast the one order of magnitude variation in $B'_{c,y}$ (noted as B'_c in Sec. 4.2.1). Therefore, the close quantitative comparison between $B'_{c,x}$ and $B'_{c,y}$ in Sec. 4.1.2 seems to be coincidence. Still, the qualitatively similarity in the dependence on spin and LL indices suggest the similar origin of the orientations characterized by $B'_{c,x}$ and $B'_{c,y}$. In addition, the phase diagram in Fig. 4.12 is consistent with our observations in individual samples, that a reorientation under $B_\parallel = B_x$ is always observed, irrespective of whether or not second reorientation under $B_\parallel = B_y$ is observed, or the value of $B'_{c,y}$.

The contrast in the density dependence of $B'_{c,x}$ and $B'_{c,y}$ highlights the asymmetry on the direction that $B_\parallel$ is applied ($B_\parallel = B_x$ vs $B_\parallel = B_y$). The asymmetry can be due to either the coupling between $B_\parallel$ and the native symmetry breaking potential, or, some mechanism that breaks the symmetry between x and y directions in terms of the effect of $B_\parallel$ but not responsible for the native stripe orientation, such as disorder. The explanation of the phase diagram in Fig. 4.12 is a subject of future studies.

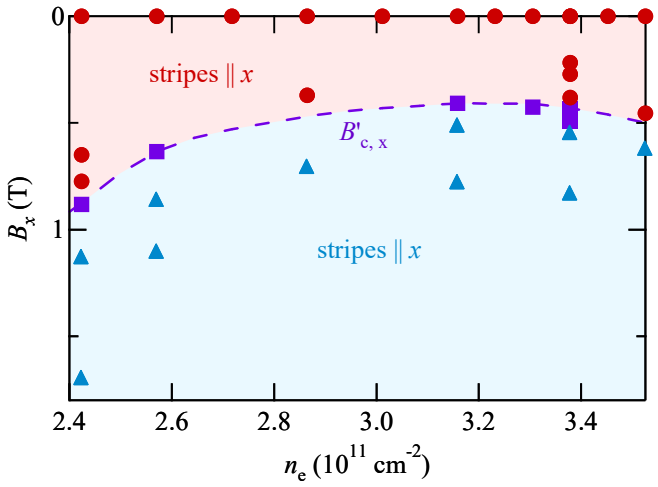

Figure 4.12: Stripe orientation as a function of n_e and B_x at $\nu = 9/2$. Triangles (circles) mark stripe orientation parallel (perpendicular) to $B_\parallel = B_x$. Squares mark the isotropic state. The upper phase boundary (dashed line) is a guide to the eyes marking $B_\parallel = B'_{c,x}$, see the text.

4.3 Partial filling factor dependence of stripe orientation within a single LL

It is well known that stripes exist in a finite partial filling factor range, roughly, $0.4 \leq \nu^* \leq 0.6$, while they break in to bubble phases out of this range through a first-order phase transition [5]. However, most of the studies have focused on the case of exact half-filling, $\nu^* = 0.5$. This is where the strongest anisotopy is observed in early studies, [4] as manifested by a maximum in the hard resistance and a minimum in the easy resistance (the latter is sometimes not present as the easy resistance is too small to reveal any variation from zero). In addition to the variation in the transport anisotropy amplitude, there are several characteristics of stripes that change as a function of ν^*. (i) It is usually observed that stripes away from half-filling disappear first as temperature is raised [7, 74]. (ii) In experiments studing the pinning mode resonances [67], a slightly higher peak frequency, lower maximum real diagonal conductivity, and lower quality factor for resonance, are observed for stripes away from half-filling. (iii) The frequency of collective excitations measured by a combination of surface acoustic wave, microwave and photoluminescence [109] decreases as one goes away from half-filling.

From the Hartree-Fock point of view, stripes away from half-filling consist of electron and hole stripes of different widths, rather than those of equal widths at half-filling. For $\nu^* = 0.4(0.6)$, the electron (hole) stripes have the width of $0.4a$, smaller than $0.5a$ for stripes at half-filling. Here a is the stripes period, $a \sim R_c \sim \nu$ for a fixed carrier density, and for high LLs such as $\nu = 4.4 \sim 4.6$, the relative variation is small. Stripe phases consisting narrower stripes, is likely to be more susceptible to disorder as well as thermal and quantum fluctuations, consistent with the experimental observations above.

4.3.1 Main observations at the first reorientation

Here we demonstrate that the $B_{\|}$-induced reorientation behavior and stripes orientation, can also be sensitive to ν^*. In Fig. 4.13 we present R_{xx} (solid line) and R_{yy} (dotted line) versus filling factor ν at different θ, from 0° to 12.2°, as marked. At $\theta = 0°$, the data reveal

[4] A deviation from this "standard" observation is observed recently, i.e., at about 20 mK, the maxim in hard resistance is usually observed at filling factors a bit higher than half; at intemediate temperatures such as 40 mK, the hard resistance displays a minimum at half-filling.

strong anisotropy near $\nu = 9/2$ with $R_{xx} \gg R_{yy}$ [see Fig. 4.13(a)], i.e., stripes are oriented along $\hat{y}$ direction. Near $\nu \approx 4.28$ and $\nu \approx 4.72$, R_{xx} and R_{yy} reveal isotropic reentrant quantum Hall or "bubble" states [6, 7, 75, 110, 111, 76]. At $\theta = 5.7°$ [Fig. 4.13(b)], new anisotropic states of *orthogonal* orientation (e.g., along $\hat{x}$-direction) develop near $\nu \approx 4.4$ and $\nu \approx 4.6$, i.e. at the edges of the native stripe range found at $\theta = 0°$. Like the native stripes, which reside near $\nu = 9/2$, these new anisotropic states are represented by high peaks along one direction and deep minima along another, albeit with $R_{yy} \gg R_{xx}$. As θ increases to 8.1° [Fig. 4.13(c)], these orthogonal anisotropic states take over larger range of ν, while the native anisotropy at $\nu = 9/2$ becomes noticeably weaker. At $\theta = 8.7°$ [Fig. 4.13(d)], stripes along $\hat{x}$-direction occupy almost the whole filling factor range of the original stripes, except near $\nu = 9/2$, where the system becomes isotropic. At still larger tilt angle, $\theta = 12.2°$, $\hat{x}$-directed stripes occur in the whole filling factor range, i.e., the reorientation of the native stripes by B_y is complete at all filling factors within the Landau level.

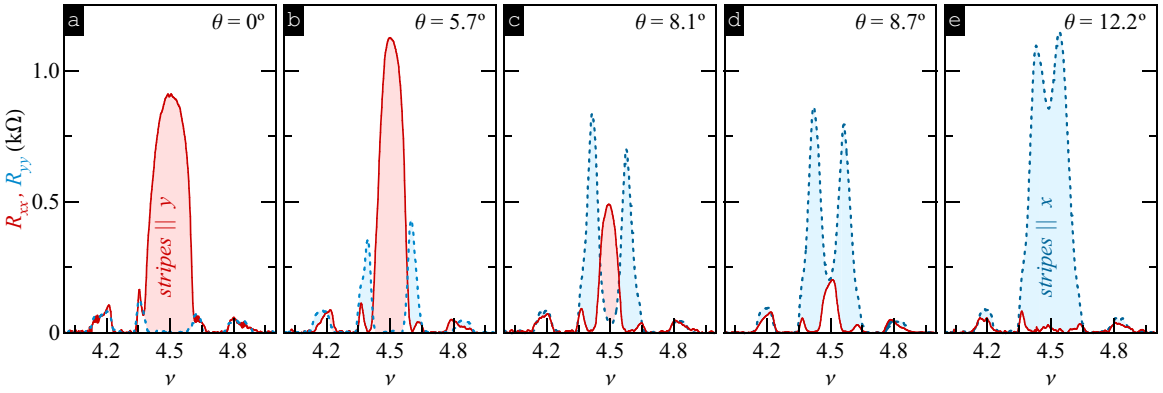

Figure 4.13: R_{xx} (solid line) and R_{yy} (dotted line) versus ν at $T = 25$ mK and θ from (a) 0° to (e) 12.2°, as marked.

Before proceeding with the more detailed data analysis, we demonstrate that the evolution shown in Fig. 4.13 is not unique to $\nu = 9/2$. In Fig. 4.14 we show R_{xx} (solid line) and R_{yy} (dotted line) at (a) $5 \leq \nu \leq 6$ and (b) $6 \leq \nu \leq 7$ measured at $\theta = 8.1°$ and 8.7°, respectively. In both cases, the data show alternating stripes orientation which is qualitatively identical to what is observed in Fig. 4.13(c). We thus conclude that the sensitivity of the stripes orientation to the filling factor is a generic feature of the anisotropic phases in

our sample; it appears in both spin-up and spin-down branches and in different ($N = 2, 3$) Landau levels.

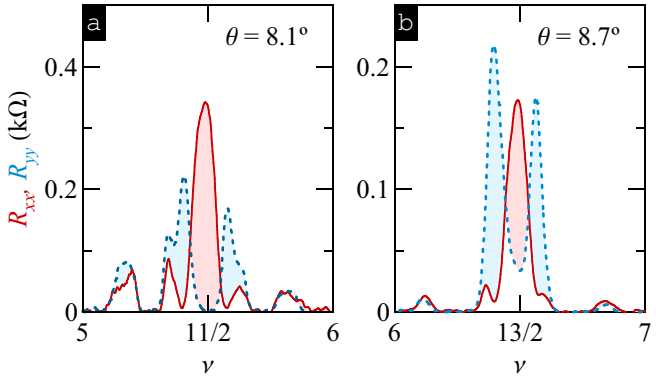

Figure 4.14: R_{xx} (solid line) and R_{yy} (dotted line) versus ν around (a) $\nu = 11/2$, $\theta = 8.1°$ and (b) $\nu = 13/2$, $\theta = 8.7°$.

To further examine the evolution of the anisotropic states with the tilt angle, we compute the resistance anisotropy $A_R = (R_{xx} - R_{yy})/(R_{xx} + R_{yy})$ from the data shown in Fig. 4.13 and present the results in Fig. 4.15. At $\theta = 0$ [Fig. 4.15(a)], we see that $A_R \approx 1$ at all filling factors within a band $4.4 \leq \nu \leq 4.6$, reflecting the native stripes orientation along $\hat{y}$ direction. As the sample is tilted, this $A_R \approx 1$ band becomes narrower [Fig. 4.15(b) and Fig. 4.15(c)], and eventually vanishes as the system becomes isotropic at $\nu = 9/2$, where $A_R \approx 0$ [Fig. 4.15(d)]. Concomitant with the narrowing of the $A_R \approx 1$ band (stripes $||\hat{y}$), we observe the emergence of the $A_R \approx -1$ bands (stripes $||\hat{x}$), which germinate at the edges of the native stripe band [Fig. 4.15(b)]. With increasing θ, these $A_R \approx -1$ bands expand towards each other [Fig. 4.15(c)] and eventually merge at half-filling [Fig. 4.15(d)]]. At the $\theta = 12.2°$ [Fig. 4.15(e)], the $A_R \approx -1$ band occupies the whole range of the native stripes, $4.4 \leq \nu \leq 4.6$, i.e. stripes are now oriented along $\hat{x}$ direction everywhere within the spin-down branch of the $N = 2$ Landau level.

Taken together, the data demonstrate that the reorientation of stripes by $B_{||}$ depends sensitively on the filling factor and that at a certain fixed θ stripes can reorient twice within a single Landau level. More specifically, we establish that the reorientation first occurs at filling factors near the onset of the native stripes, i.e. at $\nu \approx 4.4$ and $\nu \approx 4.6$, and then the boundary, separating two orthogonal stripe phases, propagates towards half-filling.

We next quantitatively examine the evolution of the anisotropy with $B_{||}$ at different

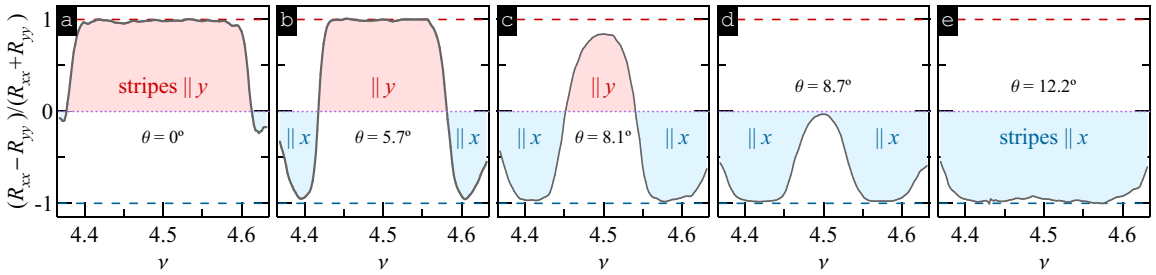

Figure 4.15: Resistance anisotropy $A_R = (R_{xx} - R_{yy})/(R_{xx} + R_{yy})$ versus ν computed from the data in Fig. 4.13.

fixed filling factors in the vicinity of $\nu = 9/2$. In Fig. 4.16(a), (b), and (c), we present R_{xx} (filled circles) and R_{yy} (open circles) as a function of B_y, at $\nu = 4.5$, 4.46, and 4.43, respectively. In all three cases, we find that the anisotropy axes are switched when $B_\parallel$ reaches a characteristic field B_c, defined such that $R_{xx} \approx R_{yy}$ (cf. $\downarrow$). We further notice that B_c *decreases* as ν deviates from half-filling. We summarize these findings in Fig. 4.16(d) showing B_c as a function of ν. The dashed and dash-dotted lines in Fig. 4.16(d) represent $B_\parallel$ at $\theta = 8.1°$ and $\theta = 5.7°$, corresponding to the situation of Fig. 4.13(c) and Fig. 4.13(b), respectively. Two crossings of these lines with B_c is reflected in the transport data as switching of the anisotropy axes during the magnetic field sweep.

The characteristic field B_c reaches its maximum value of about 0.43 T at $\nu = 9/2$. As ν deviates from half-filling, B_c gradually decreases to ≈ 0.23 T at both $\nu = 4.41$ and $\nu = 4.59$ The dependence of B_c on ν is roughly symmetric about half-filling and can be reasonably well described by a parabola (dotted line).

Since B_c characterizes the competition between the native symmetry breaking potential and the effect of $B_\parallel$ on the orientation of stripes, the decrease of B_c away from half-filling can be due to either a stronger effect of $B_\parallel$ or a weaker native symmetry breaking potential at these filling factors. However, since the effect of $B_\parallel$ is predicted to have a very weak dependence on ν [102, 103], the relationship between B_c and ν must reflect a weaker native symmetry breaking potential away from half-filling. We note that the observed dependence is quite significant; B_c decreases by nearly 50% as ν is changed from 9/2 to 4.4 or 4.6. In other sets of measurements, we have also observed that the resistance at away from half-filling can be sensitive to a very small $B_\parallel$ and B_c as small as 0.13 T has been obtained.

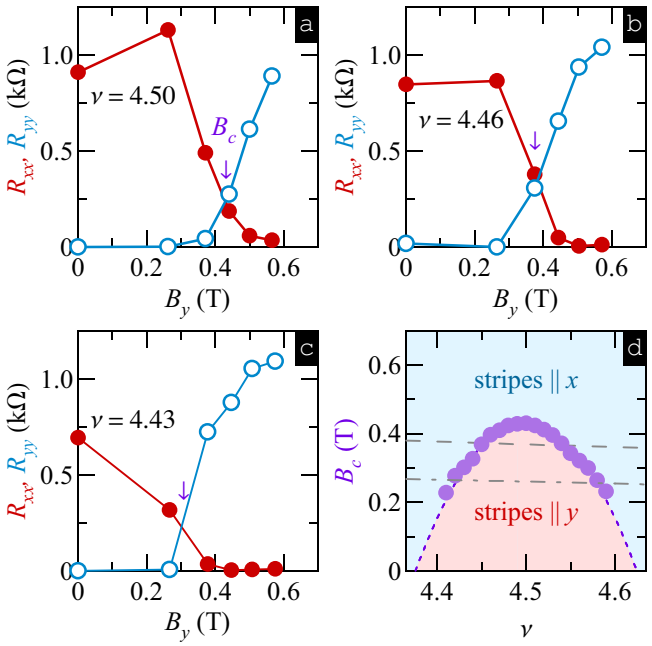

Figure 4.16: R_{xx} (filled circles) and R_{yy} (open circles) versus B_y (a) $\nu = 4.5$, (b) 4.46 and (c) 4.43. (d) B_c (filled circles) versus ν. Dashed (dash-dotted) line represents B_y at $\theta = 8.1°$ ($\theta = 5.7°$).

4.3.2 ν^* dependence at other reorientations

We observe ν^* dependence at other reorientations as well. After conducting the same procedure as in Fig. 4.16, we plot the characteristic field for the second reorientation B_c' vs ν together with B_c, and thus extended the phase diagram in Fig. 4.16. First, we observe that B_c' demonstrate the opposite dependence on ν; namely, it is larger at filling factors away from half-integer. In addition, variation in B_c' is larger in the same filling factor range.

Although we were not able to construct a similar phase diagram for $B_\parallel = B_x$ in this sample, we do observe that the B_x induced reorientations are also sensitive to ν^*. Fig. 4.18 shows an example of R_{xx} and R_{yy} vs ν at tilt angle about 13°, where the stripes are already reoriented. Variation of anisotropy amplitude is apparent, with the weakest anisotropy at half-integer filling factor, which can be only because that the stripes here are not yet fully reoriented. Therefore, we conclude that the characteristic field required to induce reorientations for $B_\parallel = B_x$, is also larger at half-integer filling factors. However, its dependence on ν^* might be weaker, and thus more difficult to be resolved.

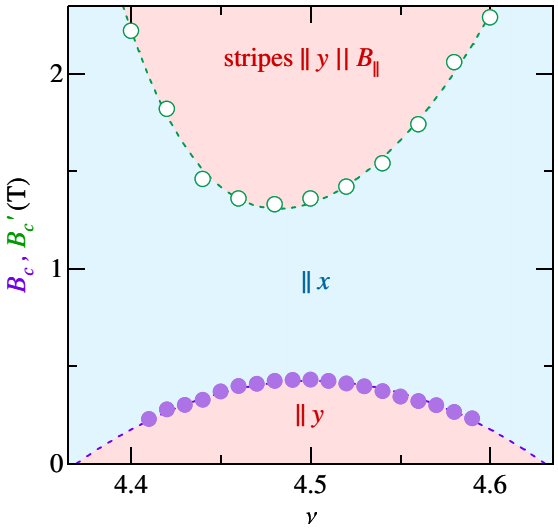

Figure 4.17: The characteristic reorientation fields B_c (filled circles) and B_c' (open circles) versus ν.

The observations above are consistent with the understanding that the ν^*-sensitivity in stripe orientation, is not with respect to the $B_{\|}$, but rather the native stripe orientation. Therefore, we conclude that the ν^*-sensitivity is due to a weaker orienting mechanism away from half-filling, rather than due to the ν^*-sensitivity in the effect of $B_{\|}$.

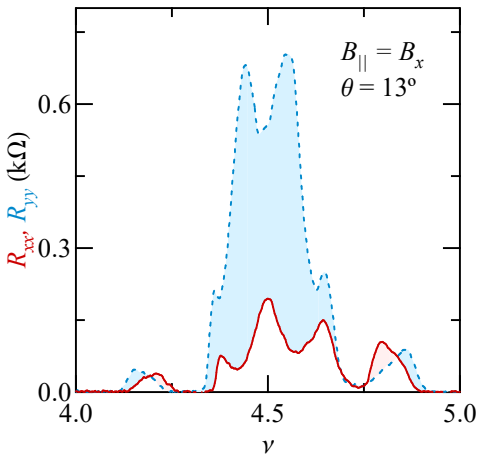

Figure 4.18: R_{xx} and R_{yy} versus ν under $B_{\|} = B_x$ at tilt angle about 13°.

4.3.3 ν^* dependence in other samples

Similar ν^* dependence are observed in almost all high-quality samples that we have studied. In Fig. 4.19 an example from sample B1 around $\nu = 9/2$ at a tilt angle is demonstrated. Here alternating stripe orientation is particularly striking, with the resistance along easy direction reaching zero in all three ν regions.

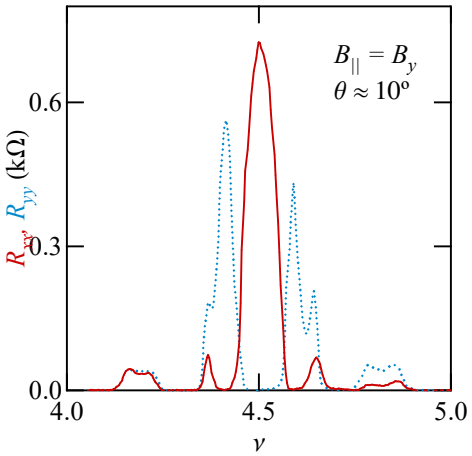

Figure 4.19: R_{xx} and R_{yy} versus ν under $B_{||} = B_y$ at tilt angle about 10° in sample B1.

4.4 Summary

We have studied the stripe orientation under the application of an in-plane magnetic field $B_{||}$ and have found that the effect of $B_{||}$ is far more rich than what was known from the early experiments, that stripes would like to align parallel to $B_{||}$. Instead, we find that the stripe orientation is sensitive to a variety of parameters, including the partial filling factor ν^*, spin and Landau level index, direction and amplitude of the applied $B_{||}$. Our findings establish the stripe orientation as a robust binary-code observable reflecting the electron-electron interactions in the high LL regime, and also shed new light on the longstanding mystery regarding the native stripe orientation.

More specifically, first, we find that there are two types of $B_{||}$-induced reorientations. The first type, known in early experiments, reorient the stripes perpendicular to $B_{||}$, and the characteristic field for the reorientations B_c is insensitive to spin, LL index, or the carrier density. The second type, reorient stripes parallel to $B_{||}$ and the characteristic field

B_c' is sensitive to the above parameters. B_c' is smaller at the lower spin branch, lower LL (but non-monotonic as a function of ν), and higher carrier density in our gated sample. The contrasting properties of the two types of reorientations strongly suggest that they are due to different mechanisms, but both controlled by the $B_{\|}$. The sensitivity of B_c' to carrier density (or other sample parameters) results in different classes of reorientation behaviors for $B_{\|}$ applied along the direction of native stripe orientation. In cases where B_c' is too large, only B_c is observed, converging with early experiments; when $B_c' > B_c$, two successive reorientations could be observed, with stripe first perpendicular and then parallel to $B_{\|}$, revealing a non-monotonic $B_{\|}$ induced anisotropy energy; there also exist a regime where no reorientations are observed and stripes stay parallel to $B_{\|}$, which can be understood as $B_c' < B_c$,.

The effect of $B_{\|}$ has so far been understood as an orbital effect, that it induces distortion of the 2D wavefunctions, and thus the stripe orientation, which is the pattern made out by the distorted wavefunctions. Within this framework, we suggest that the dependence of B_c' on spin and the carrier density may be due to the difference inter-LL screening. Essentially, at lower spin branch and higher carrier density, the perpendicular magnetic field B_z is larger for a certain LL, which leads to a larger dielectric function considering inter-LL screening. Stripes parallel to $B_{\|}$ are favored when screening is weaker according to the HF calculations[102]. However, the arguments above don't account for how screening changes as a function of $B_{\|}$ (calculations under random phase approximation show that the dielectric function depends weakly on $B_{\|}$), so the origin for the non-monotonic effect of the $B_{\|}$ on stripe orientation remains unclear.

In addition, we observe asymmetry in the magnitude of B_c' regarding whether $B_{\|}$ is applied along or perpendicular to native stripes. The asymmetry suggests coupling between the effect of $B_{\|}$ and the native orienting mechanism that cannot be simply accounted for by a sum of the anisotropy energies. We recall that the native stripe orientation may depend on spin and LL index [61], or the carrier density in a certain sample [60, 61]. We suggest that the variation of native stripe orientation may have the same origin as the sensitivity of the orientation with respect to $B_{\|}$ to such parameters. The variation of native stripe orientation as observed in [60, 61] can be also understood as due to a change of screening with these parameters. The difference is that, in our experiments, the distortion of the wavefunction is provided by $B_{\|}$, while in [60, 61], one can think that the native orienting

mechanism, wherever it originates from, controls the stripe orientation by distorting the 2D wavefunction, in a similar way as the $B_{\|}$ does. Furthermore, the distortion of the wavefunction due to the native mechanism and the $B_{\|}$ may be coupled in a non-trivial way. B_c observed when $B_{\|}$ is applied along native stripes, which is small (around 0.5 T) and shows very weak dependence on spin, LL index or carrier density, may signal canceling of the native distortion by $B_{\|}$.

Finally, we observe that the $B_{\|}$-induced reorientations are sensitive to the partial filling factor ν^*. Experiments for both $B_{\|} = B_x$ and $B_{\|} = B_y$ suggest that the ν^*-sensitivity in stripe orientation, is not with respect to the $B_{\|}$, but rather the crystal axes (or the native stripe orientation). More specifically, stripes at exactly half-filling have a more robust tendency to stay in the native orientation. Our observations suggest a weaker native orienting mechanism at away from half-filling. The sensitivity of stripe orientation in ν^* leads to metastable stripe orientation as we discuss in the next chapter.

Chapter 5

Metastable stripe orientation and its relaxation

5.1 Metastable stripe orientation at low temperatures

In 4.3 we have focused on alternating stripe orientation within a single LL at a temperature about 50 mK. Interestingly, as temperature is lowered, different stripe orientations are observed in field sweeps. In Fig. 5.1(a) we present R_{xx} (solid line) and R_{yy} (dotted line) as a function of filling factor ν measured at $T \approx 75$ mK. The data demonstrate strong anisotropy (with $R_{xx} \gg R_{yy}$) near both $\nu = 9/2$ and $\nu = 11/2$, signaling that stripes at both filling factors are oriented along the native, $\hat{y} = \langle 110 \rangle$, direction. Around fractional fillings, $\nu \approx 4.28$ and $\nu \approx 4.72$, both R_{xx} and R_{yy} reveal insulating states owing to the formation of bubble phases [4, 6, 7, 75, 110, 111, 76]. Closer examination of the data in Fig. 5.1(a) around $\nu = 9/2$ reveals that further away from half-filling $R_{yy} \gg R_{xx}$ (marked by $\downarrow$). This observation indicates that stripes at these filling factors have, in fact, already undergone $B_{\|}$-induced reorientation and are now aligned along the $\hat{x}$ direction. This happens because stripes away from half-filling require a smaller $B_{\|}$ to be reoriented, and, as a result, orientation of stripes within a given Landau level at a fixed tilt angle depends sensitively on the filling factor [13], as we have discussed in 4.3.

Like Fig. 5.1(a), Fig. 5.1(b) shows R_{xx} (solid line) and R_{yy} (dotted line) versus ν but measured at a lower temperature, $T \approx 20$ mK. One observes that the bubble phases are now almost indistinguishable from the neighboring integer quantum Hall states. The most

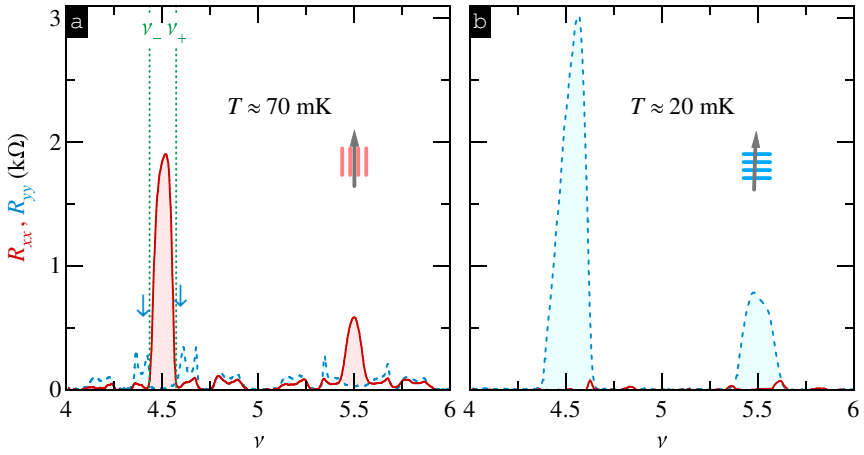

Figure 5.1: R_{xx} (solid line) and R_{yy} (dotted line) as a function of ν measured at (a) $T \approx 75$ mK and (b) $T \approx 20$ mK. The magnetic field was tilted with respect to the sample normal by $\approx 6°$. Cartoons illustrate orientation of the stripes with respect to the direction of $B_\parallel$ (thick arrow). Dotted lines around $\nu = 9/2$ in panel (a) mark filling factors $\nu_+ \approx 4.57$ and $\nu_- \approx 4.43$ near which the anisotropy energy changes sign at this tilt angle.

striking change, however, is that now one finds $R_{xx} \ll R_{yy}$ near both $\nu = 9/2$ and $\nu = 11/2$, indicating alignment of stripes along the $\hat{x}$ direction.

Since both data sets shown in Fig. 5.1 are acquired at the same tilt angle, one can argue that lowering the temperature is the sole cause for the observed reorientation. If so, one could be tempted to conclude that, surprisingly, the native symmetry-breaking potential becomes *weaker* at lower T as it is now easier to be overcome by the $B_\parallel$-induced anisotropy energy. However, as we show next, such a conclusion is premature.

We recall that the native stripes align along either $\hat{y} = \langle 110 \rangle$ (most common scenario) or $\hat{x} = \langle 1\bar{1}0 \rangle$ orientation [60, 112, 61, 62] but never otherwise. Moreover, there is strong evidence for the existence of two distinct minima in the native orientation potential along orthogonal directions [112]. The anisotropy energy can be defined as a difference between these two minima, $E = E_x - E_y$. While the orientation of stripes is usually decided by the sign of E, it can also be determined by the history. The latter happens when (i) E changes sign at some filling factor within a region where stripes form and (ii) the relaxation is slow enough for the system to relax from the higher minimum to the ground state during the magnetic field sweep. Indeed, both [60] and [112] observed that when ν is swept from high to low (low to high) stripes near $\nu = 9/2$ align along the $\langle 110 \rangle$ ($\langle 1\bar{1}0 \rangle$) direction. Field-cooling [112] confirmed the existence of the filling factor at which E changes sign.

Thus, observed hysteresis demonstrates that the orientation of stripes manifested in low-temperature measurements can be governed by the sign of E preceding the degeneracy of the two minima. In other words, no matter which orientation is realized first, stripes can get stuck in that orientation even though the sign of E suggests an orthogonal one.

At this point it is worth mentioning that in our experiment, up- and down-sweeps of the magnetic field revealed essentially identical data at both $T \approx 75$ mK and 20 mK. While no significant hysteresis was observed at these temperatures, our experimental situation bears clear similarities to that of [60, 112], albeit with one difference. Indeed, our higher temperature data clearly illustrate the existence of characteristic filling factors around $\nu = 9/2$, ν_+ and ν_-, separating stripes of orthogonal orientations [cf. dotted lines in Fig. 5.1(a)]. The anisotropy energy is negative when $\nu_- < \nu < \nu_+$, vanishes at ν_+ and ν_-, and is positive further away from half-filling. As a result, crossing either ν_- or ν_+ leads to a sign change of E, very much like the situation of [112]. The important distinction, however, is the existence of *two* such filling factors in the filling factor range within which stripes form. As a result, the stripe orientation revealed in magnetic field sweeps can be a metastable one, even if no hysteresis appears.

We now demonstrate that the data in Fig. 5.1(b) at near both $\nu = 9/2$ and $11/2$ represent a metastable stripe orientation. To prove this, we have performed an additional experiment the results of which are summarized in Fig. 5.2. First, we cool down (i) our sample at a fixed filling factor $\nu \approx 4.52$ starting from $T \approx 75$ mK (square) down to $T \approx 20$ mK (circle) and observe a monotonic increase in R_{xx}. R_{xx} vs ν is shown as the dotted line in Fig. 5.2(a), and Fig. 5.2(b) plot the time trace of R_{xx} in the cooling process.The field-cooling data unambiguously demonstrate that when $\nu_- < \nu < \nu_+$, the equilibrium configuration corresponds to a stripe phase oriented along $\hat{y}$ direction at 20 mK, while the data shown in Fig. 8.1(b) likely reflects a metastable orientation. Next, we prepare stripes in metastable orientation again, by first sweeping the magnetic field away from the stripes region (ii, upper curve), and then returning back to $\nu \approx 4.52$ (iii, lower curve). Indeed, we find that $R_{xx} \approx 0$ at this filling factor, i.e. stripes are now oriented along $\hat{x}$ axis within the entire range of filling factors. This happens because, before the system enters the range $\nu_- < \nu < \nu_+$, where $E < 0$, it first needs to traverse the regime favoring stripes along $\hat{x}$ direction ($E > 0$) which occurs at $\nu > \nu_+$. The relaxation time is long enough to preserve the initial stripe orientation for the duration of the field sweep. Finally, we warm up (iv) the system at this

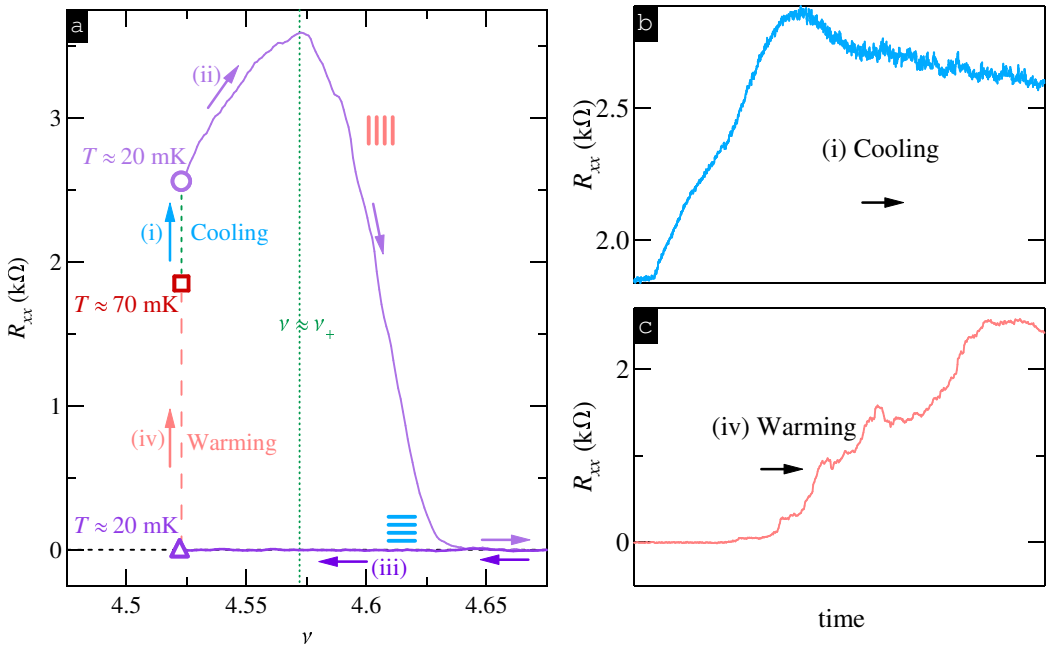

Figure 5.2: (a) R_{xx} vs. ν measured during (i) cooling (dotted line) from $T \approx 75$ mK (square) down to $T \approx 20$ mK (circle) at $\nu \approx 4.52$, (ii) down-field sweep at $T \approx 20$ mK (top curve), (iii) up-field sweep at $T \approx 20$ mK (bottom curve), and (iv) subsequent warming (dashed line) from $T \approx 20$ mK (triangle) to $T \approx 75$ mK (square) at $\nu \approx 4.52$. Cartoons illustrate orientation of stripes. The magnetic field was tilted with respect to the sample normal by $\approx 6^\circ$. Vertical dotted line is drawn at $\nu = \nu_+ \approx 4.57$. (b)[(c)] demonstrate the time trace of R_{xx} in step (i)[(iv)] when the sample is cooled down (warmed up) between about 20 mK and 75 mK.

filling factor [dashed line in Fig. 5.2(a) and see also Fig. 5.2(c) and observe an increase of R_{xx} which indicates reorientation of stripes back to $\hat{y}$. This T-induced reorientation reflects a transition from a metastable ($E > 0$) to a ground state ($E < 0$).

While no hysteresis is seen at either $T \approx 20$ mk or $T \approx 75$ mK (cf. Fig. 5.1), we do indeed observe sensitivity to the field sweep direction at intermediate temperatures. In Fig. 5.3 we present R_{xx} (solid line) and R_{yy} (dotted line) measured in (a) up-sweep and (b) down-sweep at $T \approx 45$ mK. One immediately observes that the data near $\nu = 9/2$ reveal dramatic differences depending on the magnetic field sweep direction. Indeed, when the region with stripes is approached from either higher or lower ν, the first anisotropic phase characterized by $E < 0$ (stripes parallel to $\hat{x}$) is marked by a stronger resistance anisotropy [cf. $\rightarrow$ in (a), $\leftarrow$ in (b)] than its counterpart which occurs on the opposite side of half-filling. In fact, the anisotropy away from half-filling can be as strong or even stronger

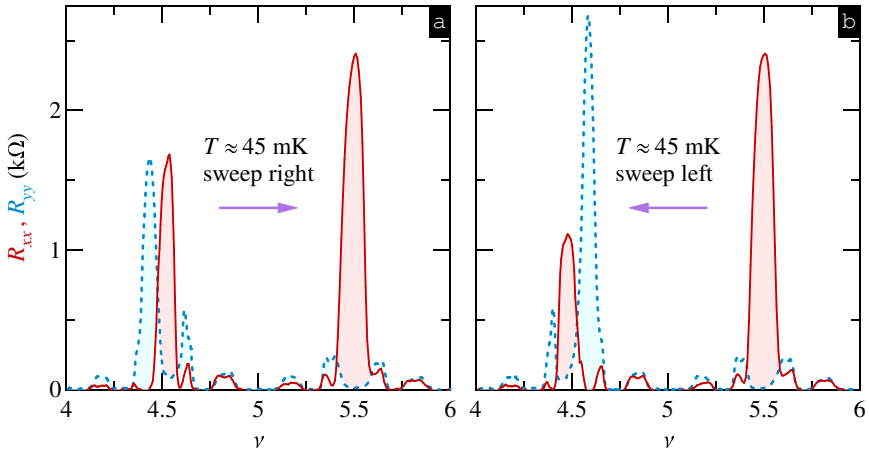

Figure 5.3: R_{xx} (solid line) and R_{yy} (dotted line) as a function of ν measured in (a) down-sweep and (b) up-sweep at $T \approx 45$ mK. The magnetic field was tilted with respect to the sample normal by $\approx 6°$.

than the anisotropy at exactly $\nu = 9/2$, in sharp contrast with the data in Fig. 5.1(a). This behavior manifests that a relaxation time at this T is comparable to the sweep time of about a minute. We note that the relaxation time appears significantly shorter than several hours in [112] at similar temperatures. At higher T, the relaxation becomes considerably faster which results in the data presented in Fig. 5.1(a) showing the equilibrium orientation of stripes with no hysteresis. At lower T, the relaxation is slower, and the transport data show the metastable orientation which is set by the sign of E away from half-filling.

Now we comment on several interesting features around $\nu = 11/2$, which are in contrast to those around $\nu = 9/2$ as we have beening focusing on. First, at 75 mK as shown in Fig. 5.1(a), no stripes along $\hat{x}$ direction exist around $\nu = 11/2$. This is because stripes away from half-filling survive lower temperatures than those at half-filling; nevertheless, stripes away from half-filling did appear as temperature is lowered, and they further lead to the observation of stripes along $\hat{x}$ direction in the whole stripe filling factor range as shown in Fig. 5.1(b). This is another role that temperature plays in our observation. Second, Fig. 5.3 shows that, in contrast to $\nu = 9/2$, the magnetoresistance near $\nu = 11/2$ exhibits virtually no dependence on the sweep direction. The absence of hysteresis near $\nu = 11/2$ indicates that the relaxation time at this T is short enough for the transport to always reflect the ground state. Faster relaxation near $\nu = 11/2$ can be attributed to a larger $|E|$ at this filling factor compared to that at $\nu = 9/2$. Indeed, $B_{\parallel}$-induced reorientation requires smaller $B_{\parallel}$ at $\nu = 9/2$ than at $\nu = 11/2$ in our sample [14]. Furthermore, a faster relaxation near

$\nu = 11/2$ can also explain a lower resistance anisotropy at $T \approx 20$ mK shown in Fig. 5.1(b) compared to $T \approx 45$ mK data shown in Fig. 5.3. Here, although the majority of the domains remain in a metastable orientation during the magnetic field sweep, some of the domains might have managed to relax to the ground state, thus lowering the resistance anisotropy at half-filling.

5.2 Relaxation of stripe orientation as a function of time

5.2.1 Main observations

In this section, we study the relaxation of metastable stripe orientation at a fixed magnetic field. An example is shown in Fig. 5.4, where we plot R_{xx} which was the original hard resistance in the absence of $B_{\|}$. The data in Fig. 5.4 are taken under $B_{\|} = B_y$ at a small angle of about 6° in sample N1. Here, we first prepare the stripes at $\nu = 9/2$ in a metastable stripe orientation, with R_{xx} being very low, shown as the solid curve in Fig. 5.4(a). Then we just wait at $B = 2.6$ T, and observe that R_{xx} increases by more than 1 kΩ, shown as the dashed line in Fig. 5.4(a). After that we sweep the field down again, and observe that R_{xx} makes a peak at $\nu = 9/2$, shown as the dotted curve in Fig. 5.4(a), confirming that the stripe orientation has changed.

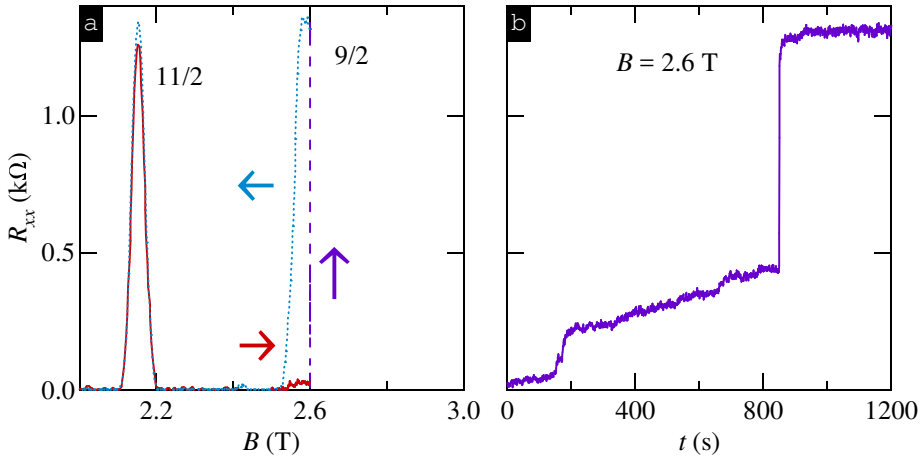

Figure 5.4: (a) R_{xx} vs. B measured during (solid) sweeping B up to 2.6 T, (dashed) waiting at $B = 2.6$ T and (dotted) sweeping B down from 2.6 T. The magnetic field was tilted with respect to the sample normal by about 6°. (b) shows the time trace of R_{xx} when waiting at $B = 2.6$ T. The measurement temperature is about 20 mK.

In Fig. 5.4(b) we plot the relaxation process of R_{xx}, which corresponds to the dashed line in Fig. 5.4(a), as a function of time. The relaxation seems to consist of two types of processes - a slow one, where R_{xx} gradually changes, and a fast one, where R_{xx} increases in abrupt jumps. The most striking jump of R_{xx} happening at $t \approx 800$ second, results in a resistance change of about 800 Ω. The jump suggests that a large patch of stripes are reorientated in a very short time. The same measurement procedure can be repeated. The relaxation as a function of time is not reproducible, but the sharp jumps of resistance are usually observed, happening at different times and resulting in different magnitudes of resistance changes, suggesting stochastic behavior.

In Fig. 5.5 we present an example where the resistance relaxes from high to low value. Here we plot R_{yy}, which is the easy resistance in the absence of $B_{\|}$ and has become the hard resistance at the beginning of this trace. R_{yy} vs time is plotted on a linear-linear plot in Fig. 5.5(a) and on a linear-log plot in Fig. 5.5(b). Several jumps can be clearly observed. It is also clear here that the change of R_{yy} becomes slower as it gets closer to its equilibrium value. The relaxation between jumps can be well described by a time-logarithmic behavior.

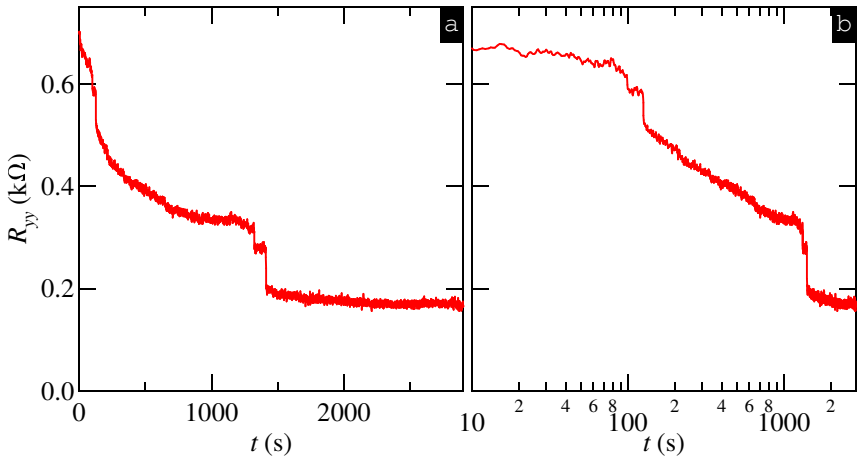

Figure 5.5: R_{xx} vs. time on a (a) linear-linear and (b) linear-log plot. The magnetic field was tilted with respect to the sample normal by about 6°. The measurement temperature is about 20 mK.

We note that similar time-logarithmic relaxation has been observed in ferromagnetic materials, and in the context of GaAs 2DEG, in fractional quantum Hall ferromagnets [113, 114]. What is common among these systems is the presence of domain structures. The time-logarithmic relaxation is understood as due to a wide spread of time constants in searching the heterogeneous free-energy landscape for the lower energy minima [113, 114].

We do not emphasize on the function form of $R(t)$, as the relation between the effective "magnetization of stripe domains" (the percentage of sample area that has stripes along the ground state orientation) and the resistances measured in the Van der Pauw geometry is likely not linear or straightforward. Indeed, time-logarithmic dependence is not observed in the relaxation from low to high resistance.

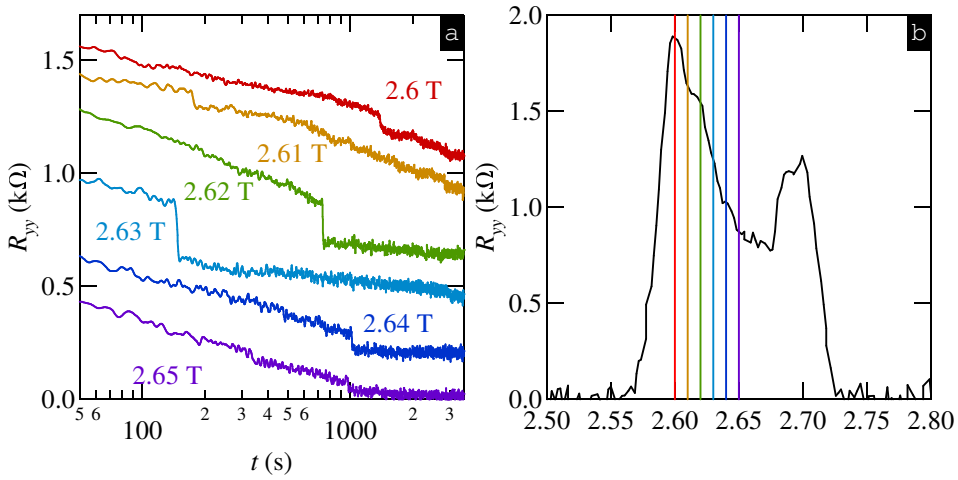

Figure 5.6: (a) R_{yy} vs. time on a linear-log plot, at different magnetic fields as marked. Traces are offset for clarity. (b) R_{yy} vs. B as B is swept from low to high values. The vertical lines mark where the field sweep is interrupted before the time trace in (a) was taken. The magnetic field was tilted with respect to the sample normal at a small angle. The measurement temperature is about 20 mK.

Next we take a look at the relaxation of stripe orientation at different filling factors. In Fig. 5.6(a) we record the change of R_{yy} as a function of time at several different fields, from 2.6 T to 2.65 T, which covers the filling factor range from about 4.57 to 4.5. Each trace was recorded by holding the field at a fixed values after sweeping from lower field out of stripe region (after each trace, the field was swept to 2.4 T and then swept to the next chosen field). The trace in Fig. 5.6(b) shows R_{yy} vs B as the field was swept covering the whole filling factor range of stripes around $\nu = 9/2$, and the vertical lines mark where the field sweep is interrupted before the time trace was taken. [1] In field sweep as shown

[1] We note that the R_{yy} does not show a single peak close to half-filling as in Fig. 5.1(b) (20 mK), but rather similar to Fig. 5.3 (45 mK), although the temperature is believed to be close to 20 mK, according to the appearance of magnetoresistance in the filling factor range between bubbles and quantum Hall states. Our data suggest faster relaxation rate than in 5.1 at the same temperature. The difference could in principle be due to the difference in $B_{\parallel}$ which adjusts the relative depths of the two energy minima, but we have searched through different angles and the manetoresistance similar to Fig. 5.1(b) is not observed. While the origin of the discrepancy is not clear, our discussion about relaxation is not affected.

in Fig. 5.6(b), a minimum is already observed close to half-filling, although the resistance is still high. In addition, when the field is held at different values as shown in Fig. 5.6(a), after one hour, the resistance at 2.64 T and 2.65 T has saturated at about 0, while those at lower fields are still non-saturating. The observations above suggest that the stripe domains relax faster close to half-filling, probably due to a larger energy difference between the two energy minima representing two stripe orientations.[2]

The slow and smooth relaxation of stripe orientation has been reported previously in [112] and discussed in light of the homogeneous nucleation theory [115] within an XY model. In this picture, bubbles nucleation of the ground state are produced by long-wavelength thermal fluctuations, and only the bubbles larger than the critical size grow until filling all the area with the ground state, while those smaller than the critical size shrink and finally disappear. The size and energy of critical bubble is decided from the competition between the energy benefit in the bulk of bubble and the cost from the surface. The relaxation rate is thus controlled by the probability of generating a bubble of a critical size, $e^{-E_c/T}$, where E_c is the energy of a critical bubble, and the growth rate of the critical bubble once it is formed. One can consider a potential $V(\theta) = h_2 \cos(2\theta) - h_4 \cos(4\theta)$ which has two minima at $\theta = 0$ and $\pi/2$ with an energy splitting of $2h_2$, and a barrier between them $V_{max} - V(0) = 2h_4$. A smaller barrier/splitting ratio h_4/h_2 gives a smaller critical bubble energy, and a larger splitting h_2 gives larger growth rate, and both could lead to a faster relaxation rate. Smaller h_4/h_2 also gives rise to thicker domain walls, which was believed to be the case in [112]. While the theory above roughly accounts for the relaxation behavior, it assumes constant relaxation rate and ignores the effect of disorder.

The novel feature in our data that is not observed in [112] or accounted for in [115] is the abrupt jumps in resistance. Before discussing its possible origin, we note on the following observations. Sometimes the jumps appear simultaneously in all the measured parts of a sample, while sometimes only appear in one part; the appearance of the jump does not rely on the application of small ac current - the resistance could change during the time that the sample is grounded; in most cases, the jumps happen in the same direction as the slow

[2] In principle, there is a scenario where stripes don't have to hold their rigidity during reorientation but would rather deform and then electrons would reorganize into stripes of the orthogonal orientation, rather than rotate between the two orthogonal orientations. It is then speculated that it is possible that stripes away from half-filling are easy to be reorientated because they are more susceptible to fluctuations and disorder. However, our data suggest that this scenario is not realistic and probably that the local stripe order is robust during relaxation.

relaxation but in some rare cases they can happen in the opposite direction. To understand the jumps, the questions we would like to ask are the following: Are they disorder-related or thermal-driven? Could quantum tunneling be relevant? Is large correlation length of stripe order a prerequisite of large resistance jumps, or could it result from fast propagation of domain walls initiated by an external turbulence?

While we could not provide a solid description of the physical process behind the resistance jumps, we note that it was understood that crackling, Barkhausen noise or avalanches are very common in disordered Ising model [116, 117]. Here the two orthogonal stripe orientations could be the effective Ising variable in a case where the barrier is much higher than their difference [118]. In addition, the size of the avalanche depends on disorder; in low disorder cases, large cluster flip happens giving large avalanches.

5.2.2 The effect of a current pulse

While we cannot thoroughly account for the resistance jumps in the relaxation process, we can think from the other direction, and ask what could be done to manipulate the relaxation process. It was known that the smooth relaxation rate increases with temperature. Here we note that a dc current pulse added to the small measurement ac current can induce resistance jumps very similar to what we observe in 5.2.1. The capability of the current pulses to induce jumps depends on both its amplitude and time duration. Typically, a current pulse of 1 μA and duration 2 ms is enough to induce jumps. There are two possible effects associated with the current pulse. First, most straightforwardly, it heats up the stripes, and stronger thermal fluctuations could help stripes to relax from the metastable state to the stable one, and the energy released can be in turn used to induce reorientations in neighboring patches, resulting in wide-spread avalanche behavior. Second, it also induces charge turbulence in the stripes, and since stripes are the pattern made out due to the interaction between electrons, reorientations may also be expected. The above two aspects can be taken as due to the kinetic and Coulomb term of the injected electrons, respectively. Whether it is the heat or charge carried by the current pulse that leads to the resistance jumps remains an open question.

The observations above also cast the question whether the resistance jumps without any intentional input, can be attributed to unintentional charge burst in the circuit. Further work needs to be done to address the question.

5.3 Cooling and warming at fixed magnetic fields

5.3.1 Resistance jumps during field cooling

In cases where magnetic field sweeps may bring the system into a metastable state, it is usually understood that cooling from a temperature where the metastable state does not exist while keeping the field fixed could uncover the ground state [112]. Here we show that field cooling could also bring the stripes into metastable orientation when the two energy minima are very close. In Fig. 5.7(a) we present R_{xx} and R_{yy} as a function of time as the sample is cooled at a fixed magnetic field.[3] Initially, a heater was holding the mixing chamber at temperature about 80 mK. At the beginning of each trace, the heater was turned off and the sample was slowly cooled down towards the base temperature of 20 mK. In Fig. 5.7(b) we plot R_{xx} and R_{yy} vs B at about 80 mK. We observe alternating stripe orientation at this temperature, suggesting that the relaxation of stripes is fast enough at this temperature to mostly recover the ground state orientation. At the $B = 2.67$ T (vertical line) where the data in Fig. 5.7(a) were taken, the two resistances are very close to each other, suggesting the two energy minima lying very close. When cooling down at this field, we observe resistance jumps as shown in Fig. 5.7(a). [4] Repeating the measurements above suggests that these resistance jumps shows similar stochastic characteristic as in 5.2.1, that the time when they take place and the resistance changes they result in are not reproducible, but the jumps are prevalent in all measurements at this field. We have tried raising the starting temperature above 150 mK and slower the cooling rate to about half of the above and the jumps still appear. On the other hand, at other filling factors where the two energy minima are not close, no such jumps are observed in field-cooling.

While the exact origin of the jumps is not clear, the observation that it is exclusive to filling factors where the two energy minima are close to each other, and its stochastic character strongly suggests that it bears similarity to those observed in 5.2.1. As the jumps in 5.2.1 appears during relaxation from a metastable state, we believe that metastable stripe orientation can also result from field-cooling. A simple picture to understand this is as follows. Considering a double-well potential with the two minimu almost equal to each other separated by a barrier, at high temperature, the stripes domains would be

[3] Data taken in sample A1.

[4] We note that the continuous R_{xx} and R_{yy} traces has to be taken in two separate field-cooling processes.

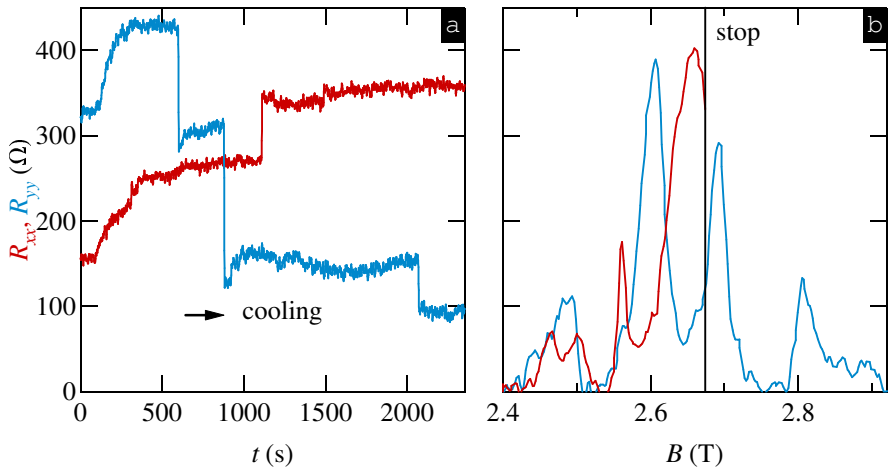

Figure 5.7: R_{xx} and R_{yy} versus (a) t as the sample is cooled from about 80 mK to 20 mK at fixed magnetic field and (b) B as the field is swept from low to high at T about 80 mK; the vertical line mark where the field is stopped. The sweeping was repeated for R_{xx} and R_{yy}.

almost equally distributed among the two wells due to the thermal fluctuations. As the temperature is lowered, less and less stripe domains should be in the excited state with slightly larger energy - at zero temperature, all the stripes should be in the ground state. However, if the cooling is faster than the relaxation rate, some stripe domains would be stuck in high minimum representing metastable orientation. In short, equilibrium is hard to reach in such a configuration, and our system can behave as a "stripe glass".

5.3.2 Telegraph noise

Our data also demonstrate telegraph noise as the sample is cooled down at a fixed field (at a small angle to the sample normal) to low temperatures about 20 mK.[5] An example is in Fig. 5.8, showing R_{yy} as a function of time. At the beginning of this trace, the heater holding the mixing chamber temperature at 180 mK was turned off. As the sample is slowly cooled, the resistance becomes more noisy and telegraph noise starts to appear. The telegraph noise is at first sparse and irregular, and after 2000 s, becomes regular as the temperature is close to base. The fluctuation is more than 5% of the total resistance and the averaging switching time between the two states is on the order of tens of seconds. A histogram of the resistance states demonstrating a clear bimodal distribution is shown in

[5] Data taken in sample H2.

the inset. Similar telegraph noise has been observed in neighboring filling factors but only close to a reorientation.

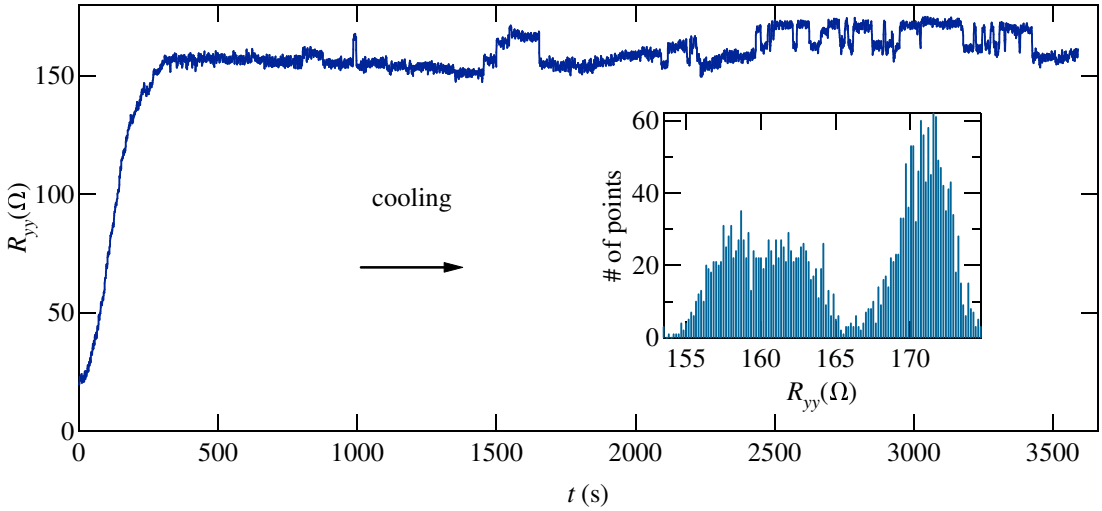

Figure 5.8: R_{yy} vs. t as the sample is cooled from about 180 mK to 20 mK. The inset shows the histogram between about 2500 s and 3500 s.

The telegraph noise we observe is a strong suggestion of the existence of two states between which the system switches back and forth. Most likely, a more specific picture is that a stripe domain switches between two orthogonal orientations. The large amplitude and clear bimodal behavior in a macroscopic sample is truly striking. It suggests long correlation lengths of the switching domain, and large barrier in the double-well potential compared to the well splitting (h_4/h_2) which also means thin domain walls. We believe that low disorder in our sample is a prerequisite for the large correlation length. Similar telegraph noise has also been observed in YBCO nanowires in the pseudogap regime [119], and has been interpreted as due to fluctuations in the nematic domain structures [119, 116]. Yet those observations are made in much smaller samples of sub-micron size, with much smaller fluctuation amplitude 0.25%, and the bimodal behavior much less clear.

5.4 Summary

We observe metastable stripe orientation in magnetic field sweeps. It originates from the ν^*-sensitivity of stripe orientation in tilted magnetic fields. When the ν^* is changed at a speed faster than the relaxation can follow, the stripes are quenched in a metastable

orientation. In contrast to the common understanding that metastable state is usually associated with hysteresis, our experiment suggests that what is observed in field sweeps may be a metastable state even if no hysteresis is observed, as the dependence on ν^* is roughly symmetric around half-filling.

The formation of metastable stripe orientation suggests a double well potential for stripes orientation, with two orthogonal orientations representing two local minima in the energy landscape, separated by an energy barrier which leads to a slow relaxation from the higher local minima to the lower one. We have studied the relaxation in the time domain and find that the relaxation consists of two types of processes - a slow one, where the resistance gradually changes, and a fast one, where the resistance jumps abruptly. The sharp jumps exhibit stochastic behavior and the resistance change can be as large as several hundred Ohms in rare events. While we could not provide a solid description of the physical process behind the resistance jumps, they probably suggest nearly degenerate local minima separated by a high barrier, which could be described by an Ising model.

In addition, we observe that metastable stripe orientation can also result from field cooling processes, which further confirms the picture above. Finally, we observe telegraph noise in the stripe regime, signaling the switch of the orientation of a local stripe patch. The large amplitude of the telegraph noise and clear bimodal behavior suggests large correlation length of stripe order in our ultra-high quality samples.

Chapter 6

The effects of alloy disorder on stripe and bubble phases

It is well known that both extremely low temperature ($\sim$ mK) and low disorder are required to observe the delicate phases in quantum Hall systems. Indeed, minimizing disorder, characterized by increasing mobility in GaAs/AlGaAs quantum wells, has been the driving force for the study of quantum Hall systems, and each significant advance reveals new physics. By a general argument, when disorder is stronger than the interaction energy, single-particle localization takes place and kills the correlation to establish the interesting phases. However, it is not clear how to quantitatively address disorder strength and interaction energy for different phases.

Disorder could also affect the melting transition of correlated phases. For both stripe and bubble phases, the cohesive energy per electron has been predicted to be about a few percent of the cyclotron energy according to Hartree-Fock calculations. This would imply $\sim$ 1 K for not too high LL, e.g., at $\nu = 9/2$ in typical samples, which is an order of magnitude larger than experimental onset temperature of about 100 mK to observe either anisotropy in transport measurements or signatures in other measurements such as pinning mode resonance [67], surface acoustic wave [71], or nuclear magnetic resonance [69]. For stripe phases, it was pointed out [108] that the experimentally observed onset temperature corresponds to a Kosterlitz-Thouless transition temperature above which dislocations became unbounded killing the long-range orientation order but the local order can still exist. However, no such

arguments have been made for bubble phases.

We have investigated the effect of alloy disorder on stripe and bubble phases. At the same low temperature about 40 mK, While both phases disappear in samples with sufficient alloy disorder, bubble phases survive more disorder than stripes phases. Before stripes are killed by disorder, the melting transition with increasing temperature is barely affected by adding in disorder, i.e., the onset temperature of anisotropy T_c stays almost constant above 100 mK, while above a certain threshold stripes are not observed even below 40 mK. This probably suggests that the melting transition is not dominated by alloy disorder.

The study on effects of disorder requires well-control of the disorder while not affecting other properties. One thing doable is introducing alloy disorder, from lattice mismatch due to Al in the GaAs quantum well. Early studies employing alloy disorder in low-mobility samples have addressed plateau-to-plateau transitions and reentrant quantum Hall states in the lowest LL. Recently, studies on the $\nu = 5/2$ fractional quantum Hall gaps have been done in alloy-disordered high-mobility samples. Since they are neutral scatters, the alloy disorder are characterized by delta-function like scattering potential with the correlation length scale just the lattice constant about 0.5 nm. In samples we studied, the average distance between alloy disorders varies from 2 to 5 nm. Both length scales are much smaller the period of stripes and bubble phases, which are of the order of the cyclotron radius and several hundred nanometers. The effective disorder potential experienced by the electrons, is thus an average on a length scale of the cyclotron radius, i.e., the effective correlation length of alloy disorder potential is of the order of the cyclotron radius. On the other hand, the mean free path of electrons is much larger (about 10 to 150 μm) even in the sample with the most alloy disorder.

6.1 Transport anisotropy and how it decays with increasing filling factor or temperature

6.1.1 Weakening stripes with increasing disorder

In Fig. 6.1 we present resistances R_{xx} and R_{yy} around filling factor $\nu = 9/2$ in 5 samples, with different alloy disorder concentrations, as marked. With increasing alloy disorder concentration, transport anisotropy close to $\nu = 9/2$ gradually diminishes. In the sample

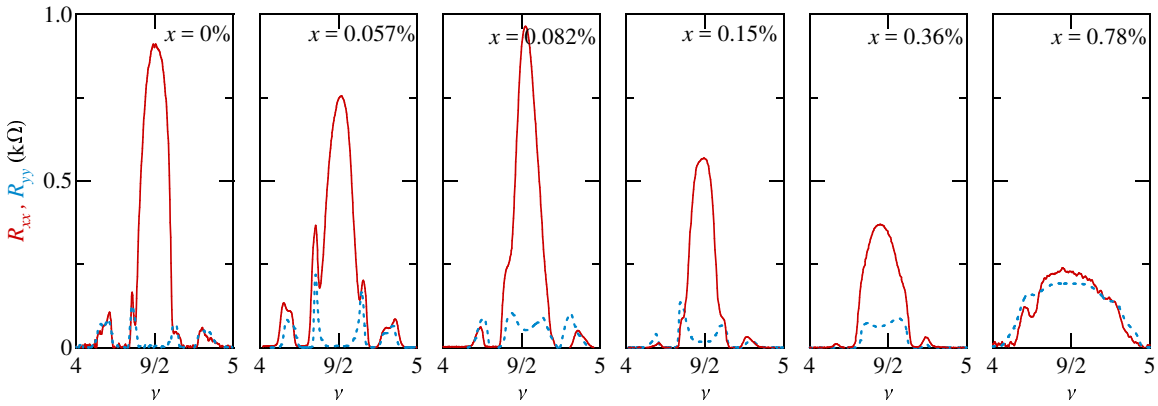

Figure 6.1: Resistances R_{xx} (solid) and R_{yy} (dashed) for filling factor $4 < \nu < 5$ in samples of different alloy disorder concentration (as marked) but otherwise similar at $T \approx 40$ mK.

with $x = 0.78\%$, we observe no significant transport anisotropy, suggesting that the addition of disorder has destroyed the formation of stripes. We note that application of in-plane magnetic field doesn't induce anisotropy either. In contrast, it has been shown that, in-plane magnetic field could induce anisotropy above the onset temperature, by aligning randomly oriented domains [104]. Our observation probably suggests that no anisotropy should be expected even at lower temperatures than in our experiment, and that local stripes orders are killed by disorder.

In the sample with $x = 0.78\%$, although there's no quantized reentrant quantum Hall effects observed, resistance minima at the filling factors for bubbles still exist. Indeed, we have observed in other samples that well-quantized bubble phases exist even no anisotropy are observed around half-filling, [1] suggesting that the bubble phases could survive more disorder than stripe phases. Although theoretical considerations on this problem have been lacking, this observation is consistent with intuition that the bubble phase, manifested by smaller clusters of electrons (or holes), could adjust themselves with more flexibility over the disorder landscape.

[1] This was observed in A8, in a different cooldown then for the data presented in the figures of this thesis.

6.1.2 Decay of stripes at high LLs

The effect of disorder on stripes is also manifested in the decay of stripes at high LLs. In Fig. 8.2(a) we show the number of LLs in which we have observed stripes at the same low $T \approx 40$ mK, as a function of alloy disorder concentration. With increasing disorder concentration, there are fewer LLs which support the formation of stripes. In other words, the critical magnetic fields for stripes onset gradually increases, as shown in Fig. 8.2(b). This is consistent with intuition, that since the cohesive energy increases with B, it is more difficult to break stripes with disorder at larger B. In Fig. 8.2(c) we plot an estimation for the stripe cohesive energy (per electron) E_c at the critical fields B_c, following the Hartree-Fock approach, $E_c \approx 0.02\hbar\omega_c$ [5].[2] On the simplest level, E_c can be taken as an estimation for the strength of disorder, i.e., it is reasonable to assume that stripe no longer survive if the energy scale of disorder is comparable to the stripe cohesive energy. As x is varied from 0 to 0.36%, we observe that E_c changes by about 400 mK and roughly doubles. We note that the change of E_c is roughly the same as the change of excitation gap for the $\nu = 5/2$ FQHE in the same series of samples [25].

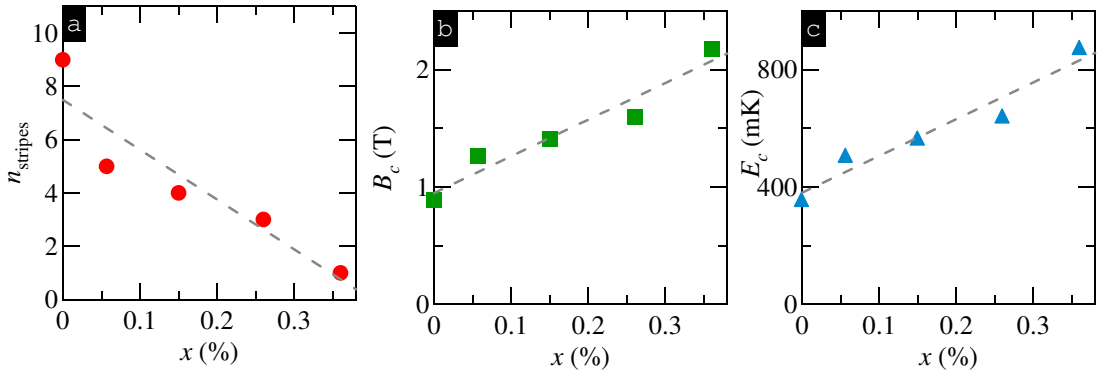

Figure 6.2: (a) Numbers of LLs showing stripes $T \approx 40$ mK, (b) the weakest mangetic field where stripes can survive, B_c, and (c) the estimated cohesive energy of stripes at B_c as a function of disorder concentration x.

6.1.3 How do disorder affect the melting temperature of stripes?

By definition, the stripe cohesive energy is also the temperature at which the stripes melt into the perfectly uniform electron liquid. However, how disorder affects the melting of stripes is somewhat surprising. In Fig. 8.3 we plot the hard resistance R_{xx} at $\nu = 9/2$,

[2] Strictly speaking, the Hartree-Fock approach only works at $N \gg 1$.

for three samples with different amount of alloy disorder, as marked. The added disorder results in higher resistance in an isotropic phase, and lower hard resistance in the stripe phase. However, remarkably, for $x = 0$ and 0.015%, the onset temperature of stripes T_c barely changes. We do not observe significant broadening of the transition, either. We note that the added alloy disorder changes mobility from 15 to 3.6 $\times 10^6$ cm^2/Vs, and reduces the gap at $\nu = 5/2$ FQHS by 220 mK [25]. Only in the most disordered sample among those which support stripes, the onset temperature drops to about 80 mK. Onset temperature T_c as a function of x is plotted in Fig. 8.3(c). The insensitivity of T_c to x suggests that the disappearance of anisotropy is probably through a transition that is not dominated by alloy disorder. In Fig. 8.3(b) we plot the onset temperature of stripes as a function of filling factor at half-integers in 3 samples with different alloy disorder concentration.

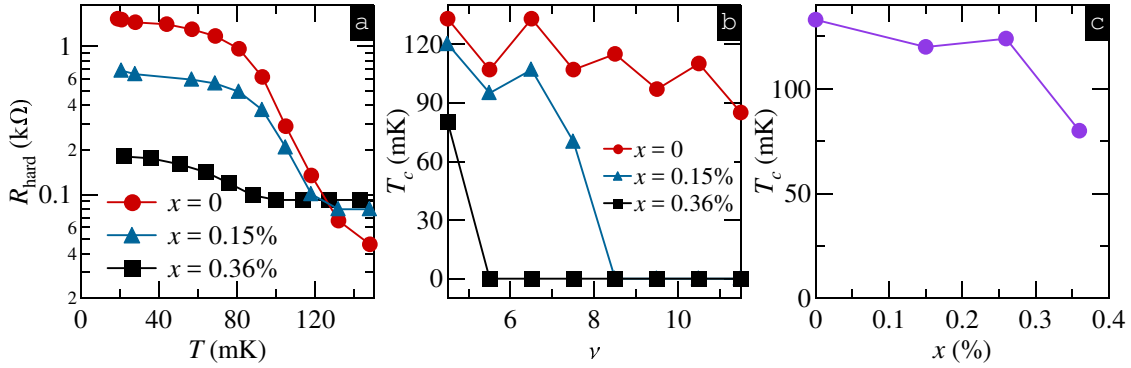

Figure 6.3: (a) The hard resistance R_{xx} as a function of T at $\nu = 9/2$ in the pristine sample and sample with alloy disorder concentration 0.15% and 0.36%. (b) The onset temeprature T_c as a function ν in these samples. (c) T_c as a function of x at $\nu = 9/2$.

The onset temperatures of bubble phases at $\nu \approx 4.72$ are very close to that for stripe phases in these A1 and A6, although we don't have it for higher disorder samples. The sharp peak at the onset temperature [76] disappears for high-disorder samples.

6.2 Reorientation by $B_{\|}$

Another interesting question is how alloy disorder affects the $B_{\|}$ induced reorientations. In Fig. 6.4 we demonstrate the reorientation of stripes under $B_{\|} = B_y$ in A1, A2, A4 with different amount of alloy disorder. They belong to the three different classes of reorientation behaviors discussed in Sec. 4.2.1. More specifically, stripes in A2 (A4) are more likely to be

parallel (perpendicular) to $B_{\|}$, while A1 is in between. In addition, A6 has the same kind of behavior with A2. The non-monotonic dependence with disorder concentration makes us conclude that disorder does not play a dominant role in the different behaviors. Instead, there are small density variations (from 2.8×10^{11} to 2.9×10^{11}) in these samples and the density dependence is consistent with Sec.4.2.1. The extreme sensitivity in density in the alloy disorder samples (more than in Sec.4.2.1) is indeed puzzling. The insensitivity of $B_{\|}$ induced stripe orientation to alloy disorder, can be understood on a similar basis as the insensitivity of stripe melting temperature to alloy disorder discussed in Sec.6.1.3. As both processes involve the alignment of stripe domains, we conclude that such alignment is not sensitive to alloy disorder.

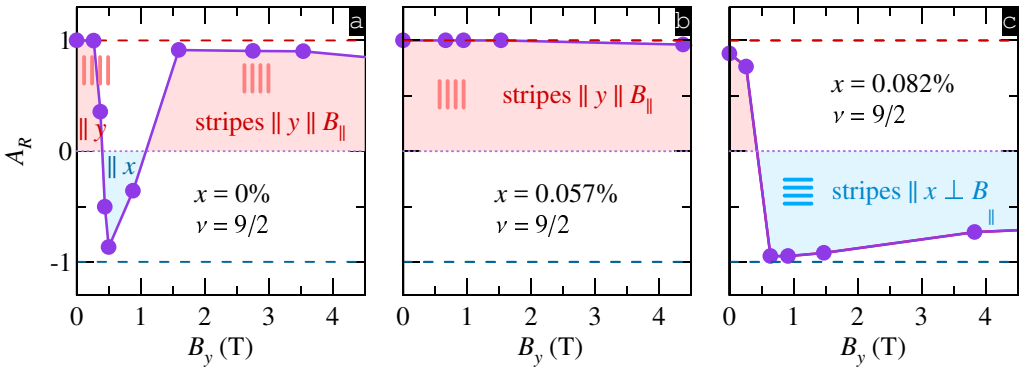

Figure 6.4: Resistance anisotropy A_R as a function of B_y in samples with different alloy disorder concentration, as marked

6.3 Double bubbles

An interesting observation in the alloy disordered samples is multiple bubble states at LL $N = 3$. In Fig. 6.5(a) we present R_{yy} vs ν in sample A8, taken at $T \approx 20$ mK. Weak resistance minima are observed at $\nu = 9/2$, 11/2 and 13/2, a feature of the easy resistance in the stripe phases. In addition, we observe resistance minima lying symmetrically on both sides of the stripe phases and separated from the integer QH states by resistance maxima, which are due to the formation of insulating bubble states. For $N = 2$, that is, between $\nu = 4$ and 6, we observe a single resistance minimum on each side as in most common cases; however, for $N = 3$, between $\nu = 6$ and 7, two resistance minima appear on each side,

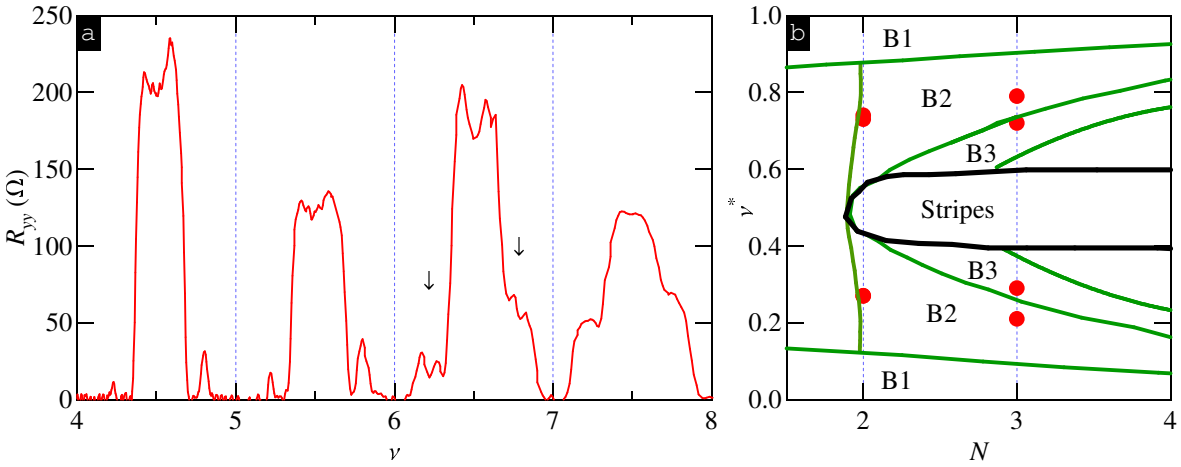

Figure 6.5: (a)Resistances R_{yy} for filling factor $4 < \nu < 8$ in samples A8 at $T \approx 20$ mK. (b)Filling factor of the observed bubble states in a $\nu^* - N$ phase diagram adopted from [99]. "B1", "B2" and "B3" mark bubble states with 1, 2, 3 electrons in each cluster, respectively.

marked by the arrows. The double minima appear in all measured parts of the sample and along both directions, and the resistances are sensitive to temperature while their positions do not change.

A likely interpretation of the double minima is the formation of bubble states consisting of different numbers of electrons in each unit cell [5, 56, 99]. According to the Hartree-Fock theory, the lattice constant of bubble states scales with $R_c = \sqrt{2N+1}l_B$. Therefore, more electrons can be accommodated in each unit cell as one goes to higher LLs. We find that the positions of the two resistance minima between $\nu = 6$ and 6.5 are at $\nu^* = 0.21$ and 0.29 respectively, with their ratio close to 2/3, suggesting bubbles of two and three electrons. In Fig. 6.5(b) we add the positions of the resistance minima on the $\nu^* - N$ phase diagram adopted from [99].

We note that the above observations are unique to the alloy disordered sample. In contrast, in samples without intentionally added alloy disorder, the filling factor of bubble states we observe for $N > 2$ are very similar to those in $N = 2$ LL.

6.4 Summary

In summary, we have studied the effect of alloy disorder on stripe and bubble phases. At low temperatures, the detriment of stripe phase due to disorder can be seen in two ways. First, at fixed filling factor and , the resistance anisotropy decreases with alloy disorder concentration. Second, the critical magnetic field B_c for stripes to appear, increases with the disorder concentration. From the change of B_c we estimate that the disorder energy scale have changed by 400 mK (which is also on the order of the stripe cohesive energy) in the sample with the maximum disorder while still supporting stripes. However, the onset temperature of stripes at $\nu = 9/2$, is essentially the same for a large range of disorder concentration, which is about 120 mK, much smaller than the estimated stripe cohesive energy. The insensitivity of the stripe onset temperature to alloy disorder, suggests that it does not manifest the melting of local stripe order, but rather the alignment of stripe domains, and the alignment is not sensitive to alloy disorder. In addition, the reorientations of stripes induced by $B_{\parallel}$, shows no systematic change with alloy disorder. This further confirms that the alignment of local stripe domains is a process not sensitive to alloy disorder.

Finally, in highly alloy disordered samples, at the $N = 3$ LL, we observe signatures suggesting two different bubble phases consisting of 2 and 3 electrons respectively per unit cell. This is in contrast to the situation in samples of zero or lower disorder concentration, that only the bubble phase of 2 electrons per unit cell has been observed in $N \geq 2$ LLs. Our observation suggests that alloy disorder stabilizes the electron crystal phases.

Part III

Experiments under microwave raidations

Chapter 7

Fine structure of high-power MIRO

7.1 Background - radiation power dependence of MIRO

As discussed in Sec.3.4, when a 2DEG is exposed to microwave radiation and weak perpendicular magnetic field B, the magnetoresistance acquires prominent $1/B$-periodic oscillations [9, 10] known as MIRO. MIRO are usually [120, 121, 122, 123, 124] attributed to the effect of Landau quantization on the radiation-assisted scattering off impurities. This affects the transport properties both directly (displacement mechanism [125, 126, 127, 128, 129, 77]) and indirectly through the emergence of a nonequilibrium electron distribution function oscillating with energy (inelastic mechanism [130, 86, 78]). The resulting photoresistivity $\delta\rho_\omega$ oscillates with the ratio $\epsilon = \omega/\omega_c$ of the microwave frequency $\omega = 2\pi f$ to the cyclotron frequency $\omega_c = eB/m$ (m is the electron effective mass) [131],

$$\frac{\delta\rho_\omega}{\rho_D} = -\lambda^2\eta\mathcal{P}\,2\pi\epsilon\sin(2\pi\epsilon)\,, \tag{7.1}$$

where η (specified below) is a dimensionless coefficient describing the combined strength of the displacement and inelastic contributions. In the expression for λ ($\lambda \ll 1$), describing the amplitude of weak oscillations in the density of states due to Landau quantization, $\tau_0^{-1} = \tau_{q0}^{-1} + \tau_{in}^{-1}(T)$ is the "total" quantum scattering rate including contributions from both the temperature (T) independent disorder and T-dependent electron-electron scattering (τ_{q0}^{-1} and τ_{in}^{-1}, respectively) to the Landau level broadening [129, 131].

Equation (7.1), applicable in the regime of low power, $\mathcal{P} \ll 1$, and overlapping Landau levels, $\lambda \ll 1$, well describes MIRO measured in many experiments [8]. It has been demonstrated that under stronger microwave radiation, $\mathcal{P} \gtrsim 1$, the oscillation amplitude undergoes a crossover to sublinear power dependence [132]. Concomitantly, the oscillation extrema move closer to the nodes at integer ϵ [132]. Such behavior is expected from theory [128, 78, 132] which attributes the nonlinear-in-$\mathcal{P}$ corrections to multiphoton processes and/or to modification of thermalization rate.

We have observed a fine structure of MIRO which emerges under intense low-frequency microwave irradiation in an ultra-clean 2DEG. This fine structure is manifested by additional ("secondary") sharp extrema residing besides the primary ones. Following theoretical framework of [132], we demonstrate that this fine structure originates from multiphoton-assisted scattering off short-range impurities, which are inherently present even in ultra-high mobility 2DEG. The properties of fine structure enable us to determine the microwave power seen by our 2DEG and to single out different photoresistance contributions, what has not been possible before [133]. The fine structure can also potentially be used as a tool to separate sharp and smooth disorder components of the electron mobility which is a subject of intense current interest but is difficult to achieve by conventional techniques [23, 134, 22, 26].

7.2 Experiment and main findings

In our experiments, the microwave radiation from the signal generator was delivered to the sample via a rectangular waveguide at various powers spanning two orders of magnitude. The longitudinal resistance was measured using low-frequency lock-in amplification under continuous microwave irradiation at a pumped liquid helium bath temperature of $T \approx 1.35$ K. In Fig. 8.1 we present the longitudinal magnetoresistance normalized to its zero-field value, $R_\omega(B)/R_\omega(0)$, recorded under microwave radiation of frequency $f = 18$ GHz for two different power levels corresponding to 0 dB and -20 dB attenuation, as marked.[1]

Vertical lines, marked by $\epsilon = 1, 2, 3$, correspond to cyclotron resonance harmonics characterized by vanishing photoresponse. At low power ($P_{\rm dB} = -20$ dB), we observe smooth MIRO exhibiting the conventional damped sine-like waveform, as prescribed by Eq. (7.1). In contrast, the data at the maximum power $P_{\max}$ ($P_{\rm dB} = 0$ dB) reveal a very rich

[1] Measurement was done in Z1.

and unusual waveform highlighted by multiple additional sharp features around each node at $\epsilon = N = 1, 2, 3$. The "secondary extrema", whose positions are marked by triangles, lie roughly symmetrically around each node and have an amplitude comparable to the primary extrema closest to the nodes. Though less pronounced, similar fine structure was observed at other frequencies.

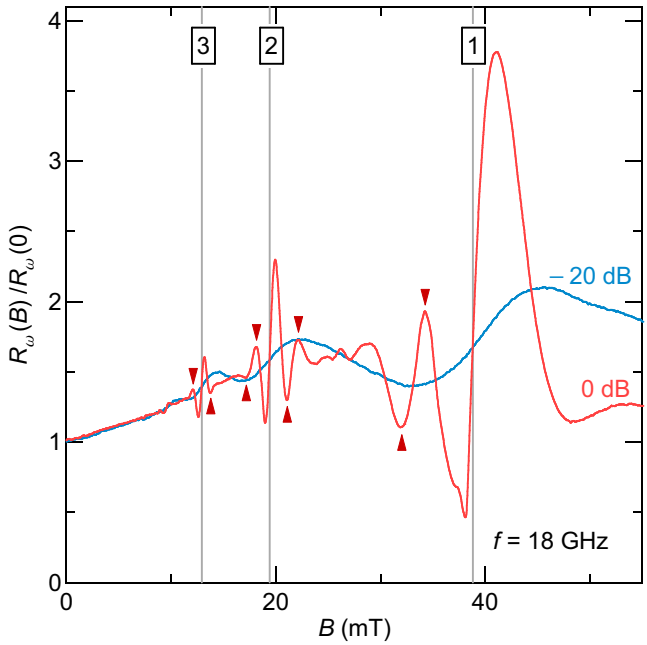

Figure 7.1: Longitudinal magnetoresistance normalized to its zero-field value, $R_\omega(B)/R_\omega(0)$, measured at $f = 18$ GHz for two different power levels corresponding to an attenuation $P_{\rm dB} = 0$ dB and -20 dB. Vertical lines mark $\epsilon = 1$, 2, 3. Secondary extrema are marked by triangles.

In Fig. 8.2 we plot the measured photoresistance (solid lines) normalized to the zero-field resistance without radiation, $\delta R_\omega/R_0$, as a function of ϵ at different powers. Here, we focus on structures around $\epsilon = 2$ and 3 where Landau levels strongly overlap, $\lambda \ll 1$. The high and low power regimes are illustrated in (a) and (b) respectively. A gradual transition between the two distinct waveforms shown in Fig. 8.1 is apparent. With decreasing power, secondary extrema move away from integer ϵ. Their amplitude decreases until they disappear at $P_{\rm dB} \sim -8$ dB (-8 dB corresponds to $\mathcal{P} \simeq \mathcal{P}_*$ specified below). This behavior clearly distinguishes the observed fine structure from the fractional MIRO [135, 136, 137, 138, 139] — distinct features in the photoresponse around certain rational $\epsilon = 1/2$, $1/3$, $3/2$, etc.

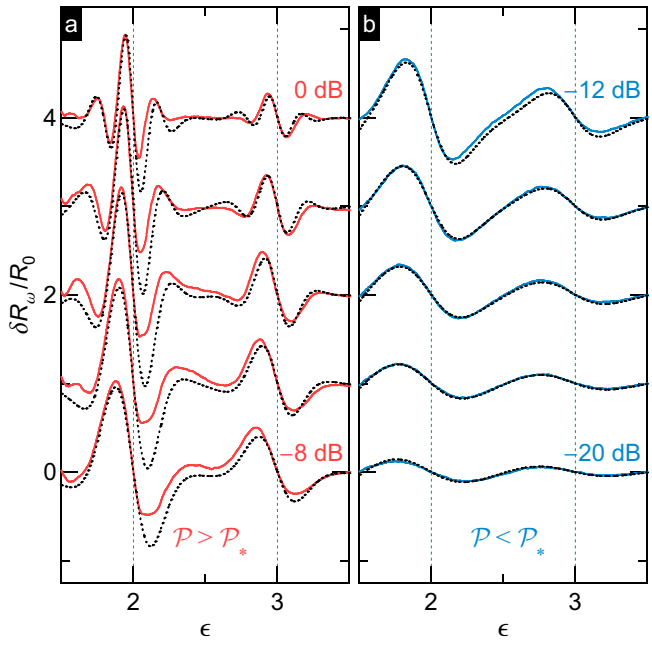

Figure 7.2: Measured (solid lines) and calculated (dotted lines) photoresistance normalized by the zero-field resistance without radiation, $\delta R_\omega / R_0$, as a function of ϵ at different power attenuations: from 0 dB to -8 dB (a) and from -12 dB to -20 dB (b), in -2 dB steps. The parameters of disorder used in calculation are: $\tau = 1.2$ ns, $\tau_{sh} = 1.7$ ns, and $\tau_{sm} = 75$ ps.

characteristic for the regime of well separated Landau levels [140, 141] and the crossover regime $\omega_c \tau_0 \sim 1$ [138]. At still lower power [panel (b)] the positions of the primary extrema still move away from the nodes and finally saturate at $\epsilon = N \pm 1/4$ consistent with Eq. (7.1).

7.3 Qualitative understanding

In the MIRO fine structures, the positions of the oscillation extrema in B are decided by not only radiation frequency, but also power. This is a remarkable character of the non-linear phenomena. The fine structures can be understood as due to multi-photon assisted scattering with disorder. We recall that the microwave drives electrons around, and thus modify the effective disorder potential experienced by the electrons. The scattering rates with the absorption or emission of N-photons can be written as [142, 132],

$$\alpha^{(N)}(\mathcal{P}, \theta) \sim J_N^2 \left[2\sqrt{\mathcal{P}} \sin(\theta/2) \right] / \tau_\theta \,, \tag{7.2}$$

where J_N is the Bessel function, and its argument contains the power factor $\mathcal{P}$ and the scattering angle θ. Similar expressions applies in other contexts, e.g., it describes the photo-assisted tunneling in irradiated Josephson junctions [143] or mesoscopic devices [144]. From Eq. (7.2), it can be seen that the scattering rates can have pronounced oscillations as a function of the power factor when scattering angle θ is large. On the other hand, in case of small angle scatterings, or when power is small, the Bessel function would not reach the oscillating regime. Therefore, the fine structure we observe, is not only a unique feature of high power MIRO, but also a fingerprint of large-angle scattering events. As we show below, because of these properties, the fine structures could be used to extract the power factor, but also disorder properties of the 2DEG in our sample, and separate the contribution of different mechanisms in MIRO. We also note that since $J_N(x)$ is strongly suppressed for Nx, a typical number of participating photons is $N_i \approx max\left\{1, \theta_i\sqrt{\mathcal{P}}\right\}$.

7.4 Quantitative analysis

We now turn to a quantitative analysis of the results within the quantum kinetic framework developed in Refs. [128, 78, 145, 77, 146, 132]. For arbitrary microwave power $\mathcal{P}$ and for $\lambda \ll 1$, the general expression for the photoresponse reads [132]

$$\frac{\delta\rho_\omega}{\rho_D} = \lambda^2(\mathcal{F}_{\rm dis} + \mathcal{F}_{\rm in}), \tag{7.3}$$

with the displacement and inelastic terms given by

$$\mathcal{F}_{\rm dis} = \tau\partial_\epsilon[\epsilon\bar{\gamma}(\xi)] - 1, \quad \mathcal{F}_{\rm in} = \frac{2\epsilon\tau\bar{\gamma}(\xi)\partial_\epsilon\gamma(\xi)}{\tau_{in}^{-1} + \gamma(0) - \gamma(\xi)}, \tag{7.4}$$

where $\xi = 2\sqrt{\mathcal{P}}\sin\pi\epsilon$. Aiming at a realistic description of elastic scattering in high-mobility 2DEGs with a minimal number of parameters, we use a two-component disorder model [145], with its sharp (smooth) component being weakly (strongly) correlated at the scale of the Fermi wave length. Within this model,

$$\gamma(\xi) = \frac{J_0^2(\xi)}{\tau_{sh}} + \frac{1}{\tau_{sm}}\frac{1}{(1+\chi\xi^2)^{1/2}}, \tag{7.5a}$$

$$\bar{\gamma}(\xi) = \frac{1}{\tau_{sh}}\left[J_0^2(\xi) - J_1^2(\xi)\right] + \frac{\chi}{\tau_{sm}}\frac{1-\chi\xi^2/2}{(1+\chi\xi^2)^{5/2}}, \tag{7.5b}$$

where τ_{sh}^{-1} and τ_{sm}^{-1} ($\tau_{sm}^{-1} \gg \tau_{sh}^{-1}$) characterize the strength of sharp and smooth disorder, respectively, while $\chi^{1/2} \ll 1$ is the typical scattering angle off smooth disorder. Here, the smooth component describes the potential of remote ionized donors. It dominates in the quantum rate: $\tau_{q0}^{-1} \equiv \gamma(0) = \tau_{sm}^{-1} + \tau_{sh}^{-1} \simeq \tau_{sm}^{-1}$. In turn, the short-range component accounts for residual impurities in close proximity [2] to the 2DEG which can contribute significantly to the momentum relaxation rate, $\tau^{-1} \equiv \bar{\gamma}(0) = \chi\tau_{sm}^{-1} + \tau_{sh}^{-1}$. This model was successfully employed to describe related nonequilibrium effects in the presence of strong dc excitation [147, 148, 149, 145, 77, 142, 150, 151]. With $\bar{\gamma}$ given by Eq. (7.5b), the displacement term $\mathcal{F}_{\rm dis} = \mathcal{F}_{\rm dis}^{\rm (sh)} + \mathcal{F}_{\rm dis}^{\rm (sm)}$ entering Eq. (7.3) naturally divides into the "sharp" ($\propto \tau_{sh}^{-1}$) and "smooth" ($\propto \tau_{sm}^{-1}$) parts, while for $\mathcal{F}_{\rm in}$ such separation is not possible.

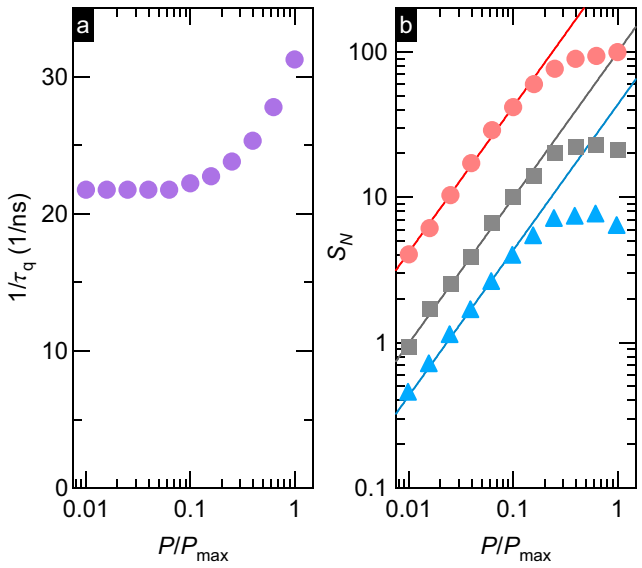

Figure 7.3: (a) Extracted quantum scattering rate $1/\tau_0$ vs normalized power $P/P_{\rm max}$. (b) Slope S_N, obtained from the data, as a function of $P/P_{\rm max}$, on a log-log scale, for $N = 1$ (circles), 2 (squares) and 3 (triangles).

As argued below, the fine structure in Figs. 8.1 and 8.2 originates from the sharp-disorder displacement contribution,

$$\mathcal{F}_{\rm dis}^{\rm (sh)} = -\frac{\tau}{\tau_{sh}} \pi\epsilon \cot(\pi\epsilon) \xi J_1(\xi) \left[J_2(\xi) - 3J_0(\xi)\right], \tag{7.6}$$

[2] Residual impurities lead to almost isotropic scattering and are modeled as a Gaussian white-noise disorder. The restrictive condition on the smooth component (fulfilled in our experiments) is that the distance to remote donors should be smaller than the magnetic length.

The expression involving Bessel functions oscillates with ξ.[3] Neglecting other contributions, for $\mathcal{P} \gg \sin^{-2}(\pi\epsilon)$ ($\xi \gg 1$) one thus obtains

$$\frac{\delta\rho_\omega}{\rho_D} \simeq 4\lambda^2 \frac{\tau}{\tau_{sh}} \cot(\pi\epsilon) \cos(4\sqrt{\mathcal{P}} \sin \pi\epsilon). \tag{7.7}$$

Equations (7.6) and (7.7) predict that, with increasing $\mathcal{P}$, more and more secondary extrema should show up in the photoresponse and, once present, each extremum should move towards the nearest node. The sensitivity of the extrema positions to microwave power thus offers a unique opportunity to quantitatively access $\mathcal{P}$ sensed by our 2DEG. Indeed, the positions of principal secondary extrema are given by $\xi = 2\sqrt{\mathcal{P}} \sin \pi\epsilon \simeq \pm 2.9$. Such scaling is observed in our data shown in Fig. 8.2 and the analysis using Eq. (7.6) for $P_{\rm dB} > -8$ dB yields $\mathcal{P} \simeq 15P/P_{\max}$. We also notice that the secondary extrema are expected to emerge at $\mathcal{P} > \mathcal{P}_* = 1.45^2 \sim 2.1$ (as follows from $|\xi| \geq 2.9$ and $|\sin \pi\epsilon| \leq 1$). In accord with this estimate, the fine structure in Fig. 8.2 becomes visible at $P_{\rm dB} = -8$ dB which corresponds to $\mathcal{P} \simeq 2.4$.

Having obtained $\mathcal{P}$ as a function of power attenuation, we turn to examination of the data at low power, where Eqs. (7.3)-(7.5) reduce to the linear-in-$\mathcal{P}$ Eq. (7.1) with

$$\eta \equiv \eta_{\rm in} + \eta_{\rm sh} + \eta_{\rm sm} = \frac{2\tau_{in}}{\tau} + \frac{3\tau}{2\tau_{sh}} + \frac{6\chi^2\tau}{\tau_{sm}}. \tag{7.8}$$

The inelastic lifetime can be estimated as $\tau_{in}(T) \simeq (\hbar E_F/T^2) \ln^{-1}(a_B v_F/2\Omega)$, where E_F and v_F denote the Fermi energy and velocity, $\Omega = \max\{T/\hbar, \omega_c^{3/2}\tau^{1/2}\}$, and $a_{\rm B} \simeq 10$ nm is the effective Bohr radius [78]. At the coolant temperature $T_0 = 1.35$ K, we obtain $\tau_{in} \simeq 120$ ps (at $\epsilon \sim 2$). On the other hand, the Dingle analysis of the lowest power photoresistance ($P_{\rm dB} = -20$ dB) yields the quantum lifetime $\tau_0 \approx 46$ ps comparable to the estimate for τ_{in}. Since $\tau_0^{-1} = \tau_{\rm q0}^{-1} + \tau_{in}^{-1}$, the contribution of electron-electron scattering to the Landau level broadening should be taken into account, wherefrom we obtain $\tau_{sm} \simeq \tau_{\rm q0} \simeq 75$ ps. We then model the lowest-$\mathcal{P}$ photoresistance trace using Eqs. (7.1) and (7.8), with τ/τ_{sh} being the only adjustable parameter (note that χ can be found from $\tau/\tau_{sh} + \chi\tau/\tau_{sm} = 1$ for a given τ/τ_{sh}, τ, and $\tau_{sm} \simeq \tau_{\rm q0}$). A dotted line, computed using $\tau/\tau_{sh} = 0.7$, is virtually indistinguishable from the experimental trace.[4] From this analysis we conclude that

[3] In Eqs. (7.1) and (7.8)-(7.9), we use $\mathcal{F}_{\rm dis} \simeq \epsilon\tau\partial_\epsilon\bar{\gamma}(\xi)$ while omitting the remaining part $[\tau\bar{\gamma}(\xi) - 1]$ which is relatively small for $2\pi\epsilon > 1$. The omitted part is included in the calculated photoresponse in Figs. 8.2 and 8.4, and provides a non-vanishing $\mathcal{F}_{\rm dis}$ at half-integer ϵ.

[4] We estimate a possible error in the extracted value of $\tau/\tau_{\rm sh} \simeq 0.7$ to be ~ 10 %. Despite the accuracy of the theoretical estimate for $\tau_{\rm in}$ can be lower, the associated error in $\tau/\tau_{\rm sh}$ is small as long as $\eta_{\rm in} \ll \eta_{\rm sh}$.

MIRO at low $\mathcal{P}$ are dominated by the displacement term associated with the sharp disorder component, $\eta_{\rm sh} \simeq 1.05$, $\eta_{\rm in} \simeq 0.2$, and $\eta_{\rm sm} \simeq 0.03$.

With a knowledge of τ/τ_{sh}, we can now compute the photoresistance using Eqs. (7.3)-(7.5) for all other power levels. The results, presented by dotted lines in Fig. 8.2, demonstrate excellent agreement at all $P_{\rm dB}$, accurately capturing the fine structures observed at higher intensities. This supports the previous analysis and confirms that the detected fine structure of MIRO originates from the multiphoton-assisted scattering by short-range impurities as described by Eqs. (7.6) and (7.7).

Apart from the known microwave power, the only parameter which was allowed to vary while generating theoretical curves in Fig. 8.2 was the electron temperature, to account for electron heating by high-power microwaves. Since $\tau_{in} \sim \tau_0 \ll \tau \sim \tau_{sh}$, we expect that heating affects primarily the quantum scattering rate entering the Dingle factor. The prefactor η, on the other hand, is affected only slightly, as it is dominated by $\eta_{\rm sh}$. Our analysis reveals that τ_0 initially stays constant at $\tau_0(T_0) \approx 46$ ps but eventually decreases to $\tau_0(T_{\rm max}) \approx 32$ ps at $P = P_{\rm max}$, see Fig. 8.3(a). Using $\tau_{in}(T_0) = 0.12$ ns and $\tau_{in} \propto T^{-2}$, we obtain $T_{\rm max} \simeq 1.7$ K and $\tau_{in}(T_{\rm max}) \simeq 0.5\ \tau_{in}(T_0)$.

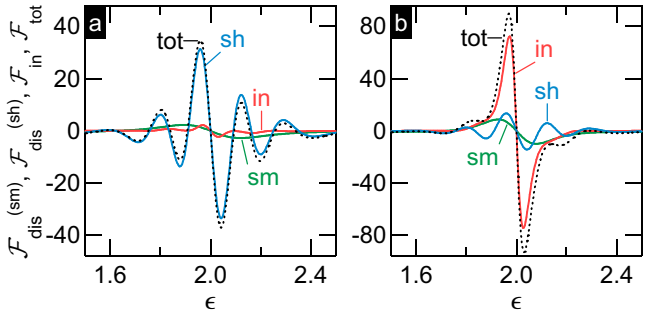

Figure 7.4: (a) Calculated $\mathcal{F}_{\rm dis}^{\rm (sh)}$ (marked as "sh"), $\mathcal{F}_{\rm dis}^{\rm (sm)}$ ("sm"), $\mathcal{F}_{\rm in}$ ("in"), and their sum $\mathcal{F}_{\rm tot}$ ("tot") vs ϵ, for $\tau/\tau_{sh} = 0.7$, $\tau_{in}/\tau = 0.05$, $\chi = 0.018$, and $\mathcal{P} = 15$. (b) The same for $\tau/\tau_{sh} = 0.3$, $\tau_{in}/\tau = 2$, $\chi = 0.042$ and $\mathcal{P} = 15$.

We confirm the effect of heating by analyzing the slope $\partial_\epsilon(\delta\rho_\omega/\rho_D)$ of the MIRO signal at integer $\epsilon = N = 1, 2, \ldots$. According to Eqs. (7.3)-(7.5), the photoresponse near integer ϵ should remain linear in $\mathcal{P}$ at arbitrary power, as long as λ and η remain $\mathcal{P}$-independent. The slope is most easily found from Eq. (7.1),

$$S_N \equiv \partial_\epsilon(\delta\rho_\omega/\rho_D)|_{\epsilon=N} \simeq -4\pi^2 N\eta\mathcal{P}\lambda^2. \tag{7.9}$$

Figure 8.3(b) demonstrates that the slope S_N, obtained from our data at $\epsilon = N = 1, 2$, and 3, indeed increases linearly with power up to $\mathcal{P} \approx 1.5$ ($P/P_{\max} \approx 0.1$) but tends to saturate or even decrease at higher P. Deviations at higher $\mathcal{P}$ become progressively stronger for larger N confirming that $\eta_{\rm in} \ll \eta$ so that heating of electrons primarily affects τ_0 entering $\lambda^2 = \exp(-N/f\tau_0)$.

We now summarize our analysis procedure. We first extract $\mathcal{P}$ from the position of the satellite extrema observed at higher powers and then find other $\mathcal{P}$ using known attenuation factors. Next, by doing standard Dingle analysis on the low power data [Eq.(1)], we obtain the quantum lifetime τ_0. Using the inelastic rate τ_{in} from theoretical estimates, the scattering rate of smooth disorder is obtained as $1/\tau_{sm} = 1/\tau_0 - 1/\tau_{in}$. We then fit the low power photoresistance with Eq.(1) and (7), leaving τ/τ_{sh} as the only fitting parameter. The photoresistance with fixed τ_{sh} and τ_{sm} is then calculated for all power levels, with the only parameter allowed to vary with power being the electron temperature. We use the slope of photoresistance at integer ϵ as a crosscheck, to confirm that the inelastic contribution is small and that the primary effect of heating is the suppression of τ_q.

7.5 Importance of backscatterings

Figure 8.4(a) illustrates the behavior of the subleading contributions $\mathcal{F}_{\rm dis}^{\rm (sm)}$ and $\mathcal{F}_{\rm in}$ which are largely irrelevant for the conditions of our experiment but can strongly affect the photoresponse in other parametric regimes. The contributions $\mathcal{F}_{\rm dis}^{\rm (sh)}$, $\mathcal{F}_{\rm dis}^{\rm (sm)}$, and $\mathcal{F}_{\rm in}$ are plotted with the above parameters found for $P = P_{\max}$, together with their sum $\mathcal{F}_{\rm tot} = \mathcal{F}_{\rm dis} + \mathcal{F}_{\rm in}$ entering Eq. (7.3). Here, both $\mathcal{F}_{\rm dis}^{\rm (sm)}$ and $\mathcal{F}_{\rm in}$ are small compared to $\mathcal{F}_{\rm dis}^{\rm (sh)}$. The large sharp disorder component produces a pronounced fine structure in the inelastic term similar to $\mathcal{F}_{\rm dis}^{\rm (sh)}$. Apart from being small due to $\tau_{in}/\tau \ll 1$, $\mathcal{F}_{\rm in}$ exhibits different positions of the secondary extrema and decays faster than $\mathcal{F}_{\rm dis}^{\rm (sh)}$ for $\xi \gg 1$. Figure 8.4(b) illustrates the parametric regime when the inelastic time is large, $\tau_{in}/\tau = 2$, while the transport rate is dominated by the smooth component of disorder, $\chi\tau/\tau_{sm} = 0.7$ (to keep $\tau_{\rm q0} \simeq \tau_{sm}$ unchanged, we use $\chi = 0.042$). Here, smooth disorder washes out the fine structure in $\mathcal{F}_{\rm in}$ which dominates the photoresponse. Despite still significant contribution of sharp disorder to the transport rate $1/\tau$, $\tau/\tau_{sh} = 0.3$, in this parametric regime the resulting fine structure in $\mathcal{F}_{\rm dis}^{\rm (sh)}$ is hardly visible on top of stronger, yet featureless contribution of $\mathcal{F}_{\rm dis}^{\rm (sm)} + \mathcal{F}_{\rm in}$.

According to the above theory, a sufficiently strong short-range disorder component is crucial for the observation of the fine structure. Apart from that, we have seen that the photoresponse is affected by detrimental heating effects which, in principle, can exponentially suppress MIRO at microwave intensities still insufficient to detect the fine structure. To avoid excess heating, it is therefore desirable to employ lower radiation frequencies as $\mathcal{P} \sim f^{-4}$. Using lower f, however, inevitably pushes MIRO to lower B which calls for samples with long quantum lifetimes. In addition, high transport mobility is also desirable since it helps to reduce both the heating effects and the inelastic contribution, which otherwise could overwhelm the MIRO signal and mask the fine structure. Finally, a nonuniformity of the microwave field across the sample may also smear out the fine structure leaving exclusively the inhomogeneously broadened primary extrema in the observed averaged signal.

7.6 Summary

In summary, we have observed and investigated high-intensity MIRO exhibiting multiple satellite oscillations. This fine structure is qualitatively distinct from conventional MIRO and can be quantitatively explained by theory considering multiphoton-assisted scattering by short-range impurities. Unique properties of the fine structure enable us to estimate all experimental parameters, including radiation intensity, draw quantitative conclusions about partial contributions to microwave photoresistance, and evaluate the role of electron heating. Furthermore, fine structure offers an opportunity to quantify short- and long-range disorder contributions to the electron mobility. For our 2DEG we demonstrate that the mobility is limited by short-range disorder, which is responsible for about 70% of the transport scattering rate.

Chapter 8

Resistively detected high-order magnetoplasmons

8.1 Background - magneto-plasmon reasonances (MPR)

When a 2DEG laterally confined to a Hall bar of width w, is subjected to a weak perpendicular magnetic field B and microwave radiation, its photoresistance reveals MPR [152, 9, 153, 154, 155, 156, 157, 158, 159, 160]. [1] Although there exists no quantitative theory of the MPR photoresistance, it is believed that the radiation absorption translates to electron heating which, in turn, causes a resistivity change [152, 154, 156].

The majority of photoresistance measurements revealed only the fundamental MPR, although in several cases the lowest few MPR modes were observed. The n-th plasmon mode has a wavenumber $q_n = \pi n/w$ ($n = 1, 2, ...$) and due to the hybridization with the cyclotron mode in a magnetic field its dispersion takes the form [162, 163],

$$\omega_{\mathrm{mp}_n} = \sqrt{\omega_\mathrm{c}^2 + \omega_{\mathrm{p}_n}^2}\,, \omega_{\mathrm{p}_n}^2 = n\omega_{\mathrm{p}_1}^2\,, \omega_{\mathrm{p}_1}^2 = \frac{2\pi\alpha c}{\epsilon^\star w}\frac{E_F}{\hbar}\,. \tag{8.1}$$

Here, $\omega_\mathrm{c} = eB/m^\star$ is the cyclotron frequency of an electron with the effective mass $m^\star$, $\omega_{\mathrm{p}1} = 2\pi f_{\mathrm{p}1}$ is the frequency of the plasmon mode with the wavenumber π/w, $\alpha = e^2/4\pi\epsilon_0\hbar c \approx 1/137$ is the fine structure constant, ϵ_0 is the vacuum permittivity, $\epsilon^\star = (\epsilon+1)/2$ is the effective dielectric constant of the surrounding medium, $\epsilon = 12.8$ is the dielectric constant of GaAs, and E_F is the Fermi energy.

[1] MPRs can also be observed directly in microwave absorption [154, 161].

The MPR can occur when the excitation frequency $\omega = 2\pi f$ is equal to ω_{mp_n} which can be tuned by B. Since the number of observable MPR modes is given by $(f/f_{\mathrm{p1}})^2$, high excitation frequency f is a prerequisite for observation of high-order modes. In addition, for the MPR modes to be experimentally resolved, the spacing between them should exceed their width. The half-width of the n-th MPR can be written as [164, 165, 166]

$$\delta\omega_{\mathrm{mp}_n} = \gamma + \Gamma_n \,, \tag{8.2}$$

where γ is the incoherent scattering rate and Γ_n is the superradiant rate due to coherent dipole reradiation of oscillating 2D electrons. The superradiant decay rate Γ_n is given by [167]

$$\Gamma_n = \Gamma_0 (L_n/\lambda)^2 \,, \quad \Gamma_0 = \frac{2\alpha}{n^\star}\frac{E_F}{\hbar} \,, \tag{8.3}$$

where L_n is the coherence length, $\lambda = c/fn^\star$ is the photon wavelength, and $n^\star = (\sqrt{\epsilon}+1)/2$ is the effective refractive index. At high n, the superradiant rate drops rapidly due to the decay of coherence length $L_n \sim w/n$ [168] and the MPR width is governed by the incoherent rate γ. Therefore, small incoherent scattering rate is another essential ingredient for the detection of high-order MPR.

In this chapter we report on high-order magnetoplasmon resonances resistively detected in very high-quality GaAs quantum wells at radiation frequencies up to ~ 0.4 THz. Owing to high sensitivity of SdHO to MPR-induced changes of electron temperature, the resonances manifest themselves as a series of resistance extrema superimposed on the SdHO. Extending to orders as high as $n = 25$, the extrema exhibit alternating strength, being less (more) pronounced at even (odd) magnetoplasmon modes. The employed experimental scheme provides a very efficient way to investigate the properties of MPR and could be applicable to other 2D systems.

8.2 Experiment and main findings

The samples in our experiments are 200 μm-wide Hall bars. The resistivity was measured at temperatures of $0.3-0.4$ K using a standard low-frequency lock-in technique, in sweeping B and under radiation of frequency f from 0.23 THz to 0.38 THz generated by a backward wave oscillator. In Fig. 8.1(a)[(b)] we show magnetoresistance $\rho(B)$ under microwave irradiation of frequency $f = 378$ GHz measured in sample A [B] at $f = 378$ [333] GHz and $T \approx 0.38$

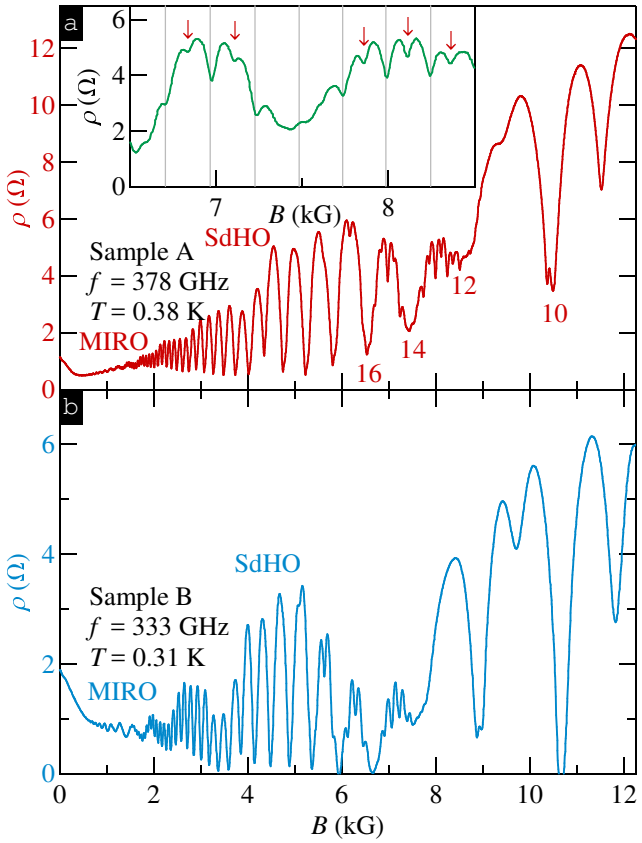

Figure 8.1: (a) [(b)] $\rho(B)$ measured in sample A [B] at $f = 378$ [333] GHz and $T \approx 0.38$ [0.31] K. SdHO minima in (a) are marked by filling factor $\nu = 8$, 10, 12, 14, 16. Inset shows zoomed-in part of the data shown in (a) near the cyclotron resonance. A series of deep (shallow) radiation-induced minima is marked by vertical lines (arrows).

[0.31] K.[2] In both samples, the data reveal MIRO [9, 83, 84, 85] and SdHO coexisting over a wide magnetic field range [169]. In addition to MIRO and SdHO, both data sets show a structure consisting of multiple sharp features in the vicinity of the cyclotron resonance.

A closer look at this structure, shown in the inset of Fig. 8.1(a), reveals that it is a series of extrema. Near the SdHO maxima, this series is represented by resistance minima which are roughly equally spaced in the magnetic field; between filling factors $\nu = 12$ and $\nu = 14$, we observe at least seven such minima. The minima can be divided into two classes, strong ones (cf. vertical lines) and weak ones (cf. ↓), appearing roughly in the middle between

[2] Sample A and B are B27-LHB and MMX respectively.

the neighboring strong minima. As discussed below, these strong (weak) features originate from magnetoplasmon resonances of odd (even) order n, with n as high as 25. While the feature around $\nu = 10$ in Fig. 8.1(a) also originates from photoresistance, identifying its exact nature is left for future studies. One possible origin is the plasmon-photon mode hybritization which leads to crossing of magnetoplasmon dispersion with cyclotron lines [170, 168].

Around the SdHO minima, MPRs are manifested by local maxima (see, e.g. a maximum at $B \approx 7.5$ GHz in the inset of Fig. 8.1(a)). These maxima are less pronounced due to a weaker temperature dependence of the SdHO resistance minima in the regime of separated Landau levels. Indeed, at even ν the density of electron states is small in a wide band around the Fermi level and raising the temperature has little effect as long as it remains small compared to inter-level spacing.

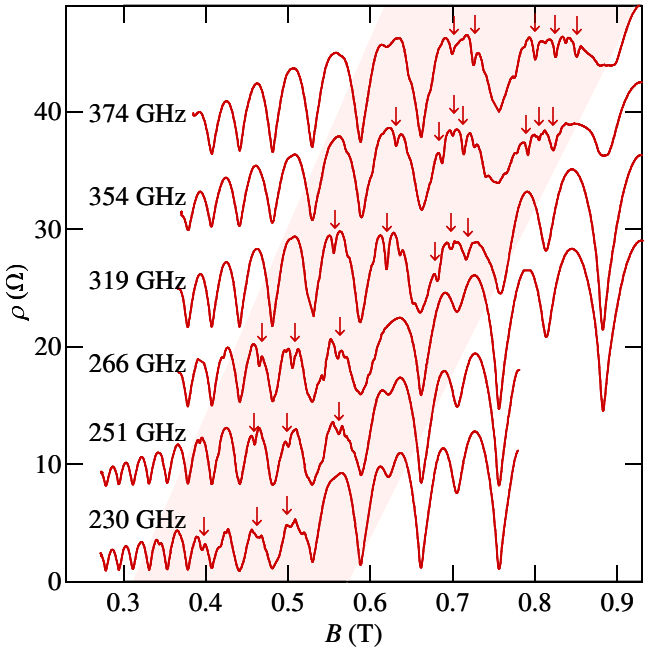

Figure 8.2: $\rho(B)$ at different f, as marked, measured in sample A. Some examples of MPR are marked by arrows. The traces are offset for clarity by 7 Ω.

8.3 Confirmation of magnetoplasmon dispersion

In Fig. 8.2 we plot magnetoresistance $\rho(B)$ measured in sample A at several frequencies from 230 GHz to 374 GHz, as marked.[3] Each trace reveals a series of extrema (some examples marked by arrow), similar to that shown in Fig. 8.1, which move to higher B with increasing f. Since the resonances are most pronounced around the SdHO maxima, these extrema are best observed at higher f (lower ν) where more MPR modes can be resolved within one SdHO period. One remarkable feature of our data is the unusually large number of both odd and even MPR modes, made possible by high sensitivity of SdHO to variations of electron temperature due to resonant absorption in our high mobility samples. [4]

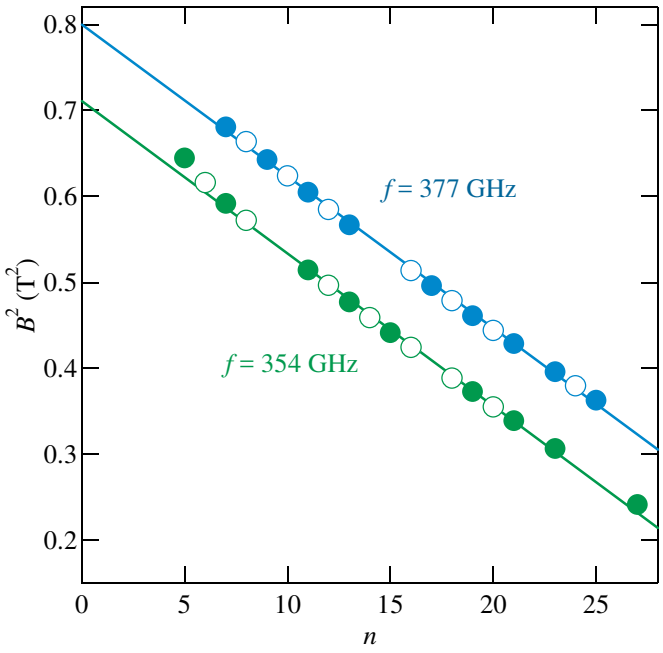

Figure 8.3: B^2 (circles) vs. n, for $f = 377$ GHz (upper) and 354 GHz (lower), obtained from sample A. Solid (open) circles represent odd (even) n. Fits to the data (lines) using Eq. (8.4) yield $m^\star \approx 0.066 m_0$ and $f_\mathrm{p} \approx 56$ GHz.

To confirm that the observed extrema originate from MPR we examine the dispersion

[3] While at different f we sometimes detect variations of electron density of $\sim 1\%$ due to different power, these variations have negligible effect on the MPR dispersion.

[4] In addition to heating, another possible contribution to the signal is the MPR-induced spatial density variations [171]. As such variations occur on the length scale set by the magnetoplasmon wavelength, it would also suppress SdHO which are measured over larger length scales.

relation for two radiation frequencies using the data from sample A. Per Eq. (8.1), the magnetic field at which the n-th MPR ($\omega = \omega_{\mathrm{mp}_n}$, $B = B_n$) occurs should satisfy

$$B^2 = B_n^2 \equiv (m^\star/e)^2 \left[\omega^2 - n\omega_{\mathrm{p1}}^2\right] . \tag{8.4}$$

In Fig. 8.3 we plot the square of the magnetic field, at which the n-th MPR occurs, for $f = 377$ GHz and $f = 354$ GHz, as marked, as a function of n. Here, filled (open) circles represent odd (even) n, spanning from $n = 5$ to $n = 27$. Lower order MPRs overlap with the cyclotron resonance absorption peak [168] which causes strong SdHO suppression making them insensitive to minute temperature changes caused by MPRs. Gaps in the data correspond to B_n away from the SdHO maxima where the resonances were not well resolved. Despite slight deviation at low n, the data for both frequencies conform to Eq. (8.4); linear fits generate $m^\star \approx 0.066 m_0$ [5] and $f_{\mathrm{p1}} \approx 56$ GHz. Obtained f_{p1} is about 0.95 of what is expected from Eq. (8.1), in reasonable agreement with past theoretical [172] and experimental [152, 154, 159] studies.

We next examine the frequency dependence of the observed resonances and demonstrate that it can also be well described by the magnetoplasmon dispersion, Eq. (8.1). In Fig. 8.4 we plot f^2 vs. B^2 for three select modes, $n = 7, 13, 19$, and observe that the data can be well described by parallel lines. Such a behavior is indeed expected for MPR since

$$\omega^2 = \omega_{\mathrm{mp}_n}^2 \equiv n\omega_{\mathrm{p1}}^2 + (e/m^\star)^2 B^2 , \tag{8.5}$$

see Eq. (8.1). The universal slope of the linear fits again conforms to $m^\star \approx 0.066 m_0$.

After performing such fits for all available n, we extract the intercepts of the fits with the vertical axis f_0^2 and present the result as a function of n in the inset of Fig. 8.4. The data reveal a linear relation between f_0^2 and n, in accordance with Eq. (8.1), and from the slope of the fit we find $f_{\mathrm{p1}} \approx 56$ GHz, in good agreement with the value obtained above. We further note that at $n < 10$, $f_0^2(n)$ slightly deviates from the linear dependence and bends down. As we show next, this deviation is likely due to retardation effects.

The retardation effects are characterized by the retardation parameter α', defined as the ratio of the plasmon frequency to the light frequency at the same wavenumber. At the fundamental plasmon wavenumber $q_1 = \pi/w$, we find, for sample A, $\omega_{\mathrm{ph}}/2\pi = c/2wn^\star \approx$

[5] Consistent with previous studies [160], this value is about 10% larger than the one obtained from MIRO.

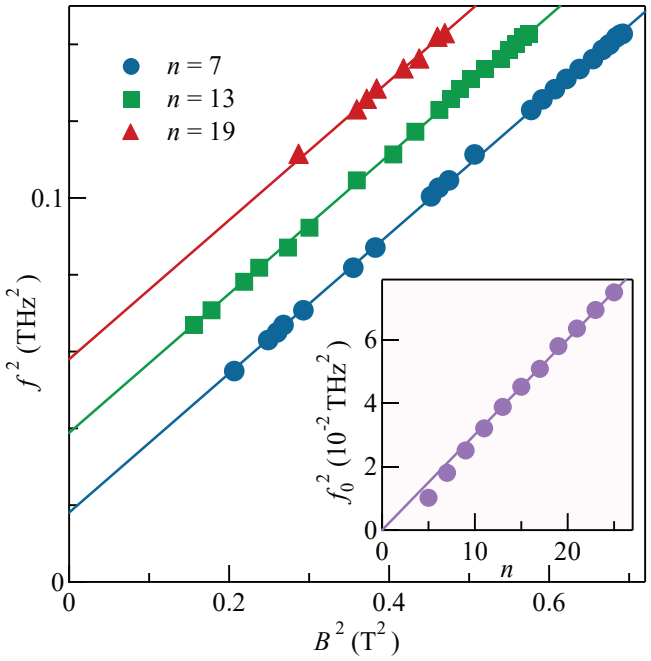

Figure 8.4: f^2 vs. B^2 for $n = 7$ (circles), 13 (squares), 19 (triangles), obtained from sample A. The fits to the data (lines) with $f^2 = f_0^2 + (e/2\pi m^\star)^2 B^2$ yield $m^\star = 0.066 m_0$. Inset shows f_0^2, obtained from the fits, vs. n, revealing linear relationship, $f_0^2 \sim n$. The slope of the linear fit (line) yields $f_{\rm P1} \approx 55$ GHz.

0.33 THz and $\alpha' = \Omega_1/\omega_{\rm ph} \approx 0.07(E_F/\hbar\omega_{\rm ph})^{1/2} \approx 0.18$. Since the phase velocity of the magnetoplasmon mode is proportional to $n^{-1/2}$, the retardation effects become weaker at higher n. It has been shown that the plasmon frequency decreases with α' [170, 154]. It is therefore reasonable to have a larger deviation from Eq. (8.1) at lower n, as observed in both Fig. 8.3 and Fig. 8.4(b).

8.4 Conditions to detect high-order MPR

As mentioned in the introduction, observation of multiple MPR modes relies on their sharpness. We estimate the half-width of the observed MPR as $\delta B_n \approx 2.5$ mT which is largely insensitive to n. Since the width is obtained from magnetoresistance, it does not directly translate to the width of the MPR. Nevertheless, since the width of the photoresistance

minima does not show significant variation within one SdHO period, it should be comparable to the actual MPR width. Using $\delta\omega_{\mathrm{mp}_n} \approx (\partial\omega_{\mathrm{mp}_n}/\partial B)\delta B_n = (e/m^\star)(\omega_\mathrm{c}/\omega)\delta B_n$, we estimate $\delta\omega_{\mathrm{mp}_n}/2\pi \simeq 1$ GHz, close to the cyclotron resonance.

The MPR width $\delta\omega_n$ is expected to be a sum of coherent radiative decay rate Γ_n and incoherent collisional rate γ, see Eq. (8.2) and Eq. (8.3). In sample A we estimate $\Gamma_0/2\pi \approx 14$ GHz and at $f = 0.38$ GHz, $\Gamma_1/2\pi = \Gamma_0/2\pi(w/\lambda)^2 \approx 4.7$ GHz. At higher n, $\Gamma_n = \Gamma_1/n^2$ becomes smaller than γ. This is consistent with our observation that the fundamental MPR $n = 1$ is not well resolved, whereas higher order MPRs have similar widths, dominated by γ.

The incoherent scattering rate γ is often associated with the transport scattering rate τ^{-1}, which is about $\tau^{-1}/2\pi \approx 0.2$ GHz in sample A. However, there exist no exact relation between the two quantities; for the electron density of sample A, [173] has found γ to be about 5 times larger than τ^{-1}, giving a conservative estimate of $\gamma/2\pi \simeq 1$ GHz. This value is in good agreement with $\delta\omega_n/2\pi \simeq 1$ GHz obtained from our experimental data.

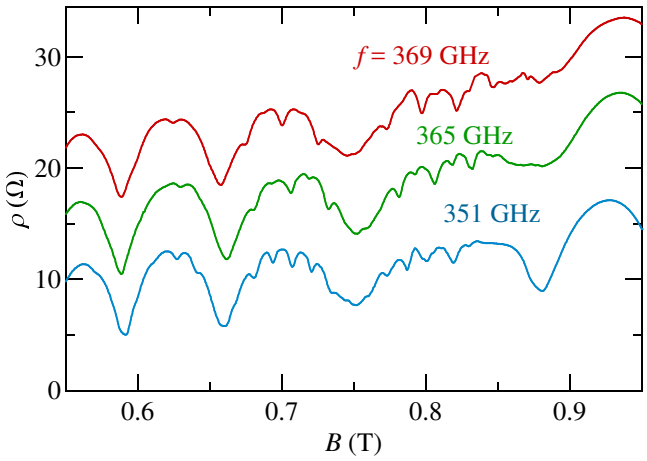

Figure 8.5: $\rho(B)$ at $T \approx 0.4$ K and different f, as marked, measured in sample A. Traces are offset for clarity by 7 Ω.

Another interesting feature revealed by our data is the even-odd mode alternating strength. Assuming a uniform electric field distribution, only odd modes are expected [172] and [154, 174] reported observation of only odd modes. Some experiments, however, revealed both odd and even low-order modes, with often comparable, yet random strengths [161, 171]. While we have clearly observed different signal strengths for even and odd modes,

their ratio can vary with the radiation frequency. In Fig. 8.5 we present $\rho(B)$ measured in sample A at different f, 369 GHz, 365 GHz, and 351 GHz. At $f = 369$ GHz (top trace), the even modes are much weaker than the odd, at $f = 365$ GHz (middle trace) they become noticeably stronger, and at $f = 351$ GHz (bottom trace) even modes become comparable to the odd ones. The variation in the strength of even modes with f likely reflects variation in radiation distribution. Since our experiments are performed without using resonant cavities, the radiation field distribution is not controllable. Furthermore, the presence of contacts, metallic pins on the chip carrier, and other metallic parts make random formation of standing waves in the sample space possible. At 0.4 THz, the distance between the nodes of such standing waves is close to or smaller than the sample dimensions. As a result, different parts of the sample are exposed to different radiation intensities. While a more uniform radiation produces weaker even modes, they become more pronounced under nonuniform radiation distribution. Our measurements never revealed even modes which are stronger than the odd ones.

8.5 Summary

In summary, exploiting high mobility 2DEGs, high radiation frequencies, and strong sensitivity to temperature of SdHO, we have detected high-order magnetoplasmon resonances. Extending to orders above $n = 25$, the MPR-induced photoresistance extrema exhibit alternating strength, being less (more) pronounced at even (odd) n. Taken together, our results demonstrate that this experimental technique provides a surprisingly sensitive and elegant means to detect and investigate high-order MPR modes which could be applicable to other 2D systems, such as MgZnO/ZnO heterojunctions [175] and AlAs quantum wells [176].

References

[1] K. von Klitzing, G. Dorda, and M. Pepper. New method for high-accuracy determination of the fine-structure constant based on quantized hall resistance. *Phys. Rev. Lett.*, 45:494, 1980.

[2] D. C. Tsui, H. L. Stormer, and A. C. Gossard. Two-dimensional magnetotransport in the extreme quantum limit. *Phys. Rev. Lett.*, 48:1559, 1982.

[3] R. B. Laughlin. Anomalous quantum hall effect: An incompressible quantum fluid with fractionally charged excitations. *Phys. Rev. Lett.*, 50:1395, May 1983.

[4] A. A. Koulakov, M. M. Fogler, and B. I. Shklovskii. Charge density wave in two-dimensional electron liquid in weak magnetic field. *Phys. Rev. Lett.*, 76:499, 1996.

[5] M. M. Fogler, A. A. Koulakov, and B. I. Shklovskii. Ground state of a two-dimensional electron liquid in a weak magnetic field. *Phys. Rev. B*, 54:1853, 1996.

[6] M. P. Lilly, K. B. Cooper, J. P. Eisenstein, L. N. Pfeiffer, and K. W. West. Evidence for an anisotropic state of two-dimensional electrons in high landau levels. *Phys. Rev. Lett.*, 82:394, 1999.

[7] R. R. Du, D. C. Tsui, H. L. Stormer, L. N. Pfeiffer, K. W. Baldwin, and K. W. West. Strongly anisotropic transport in higher two-dimensional landau levels. *Solid State Commun.*, 109:389, 1999.

[8] I. A. Dmitriev, A. D. Mirlin, D. G. Polyakov, and M. A. Zudov. Nonequilibrium phenomena in high landau levels. *Rev. Mod. Phys.*, 84:1709, Nov 2012.

[9] M. A. Zudov, R. R. Du, J. A. Simmons, and J. L. Reno. Shubnikov–de haas-like oscillations in millimeterwave photoconductivity in a high-mobility two-dimensional electron gas. *Phys. Rev. B*, 64:201311(R), 2001.

[10] P. D. Ye, L. W. Engel, D. C. Tsui, J. A. Simmons, J. R. Wendt, G. A. Vawter, and J. L. Reno. Giant microwave photoresistance of two-dimensional electron gas. *Appl. Phys. Lett.*, 79:2193, 2001.

[11] M. P. Lilly, K. B. Cooper, J. P. Eisenstein, L. N. Pfeiffer, and K. W. West. Anisotropic states of two-dimensional electron systems in high landau levels: Effect of an in-plane magnetic field. *Phys. Rev. Lett.*, 83:824, Jul 1999.

[12] W. Pan, R. R. Du, H. L. Stormer, D. C. Tsui, L. N. Pfeiffer, K. W. Baldwin, and K. W. West. Strongly anisotropic electronic transport at landau level filling factor under a tilted magnetic field. *Phys. Rev. Lett.*, 83:820, Jul 1999.

[13] Q. Shi, M. A. Zudov, J. D. Watson, G. C. Gardner, and M. J. Manfra. Reorientation of quantum hall stripes within a partially filled landau level. *Phys. Rev. B*, 93:121404, Mar 2016.

[14] Q. Shi, M. A. Zudov, J. D. Watson, G. C. Gardner, and M. J. Manfra. Evidence for a new symmetry breaking mechanism reorienting quantum hall nematics. *Phys. Rev. B*, 93:121411, Mar 2016.

[15] Q. Shi, M. A. Zudov, Q. Qian, G. C. Watson, and M. J. Manfra. Reorientation of stripe phases by in-plane magnetic fields in a tunable-density two-dimensional electron gas. *submitted*, 2016.

[16] Q. Shi, M. A. Zudov, B. Friess, J. Smet, J. D. Watson, G. C. Gardner, and M. J. Manfra. Apparent temperature-induced reorientation of quantum hall stripes. *Phys. Rev. B*, 95:161404, Apr 2017.

[17] Q. Shi, M. A. Zudov, I. A. Dmitriev, K. W. Baldwin, L. N. Pfeiffer, and K. W. West. Fine structure of high-power microwave-induced resistance oscillations. *Phys. Rev. B*, 95:041403(R), Jan 2017.

[18] Q. Shi, M. A. Zudov, L. N. Pfeiffer, K. W. West, J. D. Watson, and M. J. Manfra. Resistively detected high-order magnetoplasmons in a high-quality two-dimensional electron gas. *Phys. Rev. B*, 93:165438, Apr 2016.

[19] T. Ando, A. B. Fowler, and F. Stern. Electronic properties of two-dimensional systems. *Rev. Mod. Phys.*, 54:437, 1982.

[20] K. S. Novoselov, A. K. Geim, S. V. Morozov, D. Jiang, M. I. Katsnelson, I. V. Grigorieva, S. V. Dubonos, and A. A. Firsov. Electric field effect in atomically thin carbon films. *Science*, 306:666, 2004.

[21] A. K. Geim and K. S. Novoselov. The rise of graphene. *Nature Mat.*, 6:183, 2007.

[22] Michael J. Manfra. Molecular beam epitaxy of ultra-high-quality algaas/gaas heterostructures: Enabling physics in low-dimensional electronic systems. *Annu. Rev. Condens. Matter Phys.*, 5(1):347–373, 2014.

[23] V. Umansky, R. de Picciotto, and M. Heiblum. Extremely high-mobility two-dimensional electron gas: Evaluation of scattering mechanisms. *Appl. Phys. Lett.*, 71:683, 1997.

[24] Geoffrey C. Gardner, Saeed Fallahi, John D. Watson, and Michael J. Manfra. Modified mbe hardware and techniques and role of gallium purity for attainment of two dimensional electron gas mobility ¿35106cm2/vs in algaas/gaas quantum wells grown by mbe. *Journal of Crystal Growth*, 441(Supplement C):71 – 77, 2016.

[25] Nianpei Deng, G. C. Gardner, S. Mondal, E. Kleinbaum, M. J. Manfra, and G. A. Csáthy. $\nu = 5/2$ fractional quantum hall state in the presence of alloy disorder. *Phys. Rev. Lett.*, 112:116804, Mar 2014.

[26] S. Das Sarma and E. H. Hwang. Mobility versus quality in two-dimensional semiconductor structures. *Phys. Rev. B*, 90:035425, Jul 2014.

[27] M. Samani, A. V. Rossokhaty, E. Sajadi, S. Lüscher, J. A. Folk, J. D. Watson, G. C. Gardner, and M. J. Manfra. Low-temperature illumination and annealing of ultrahigh quality quantum wells. *Phys. Rev. B*, 90:121405, Sep 2014.

[28] Q. Qian, J. Nakamura, S. Fallahi, G. C. Gardner, J. D. Watson, S. Lüscher, J. A. Folk, G. A. Csáthy, and M. J. Manfra. Quantum lifetime in ultrahigh quality gaas quantum wells: Relationship to $\Delta_{5/2}$ and impact of density fluctuations. *Phys. Rev. B*, 96:035309, Jul 2017.

[29] Q. Qian, J. Nakamura, S. Fallahi, G. C. Gardner, J. D. Watson, and M. J. Manfra. High-temperature resistivity measured at $\nu = \frac{5}{2}$ as a predictor of the two-dimensional electron gas quality in the $n = 1$ landau level. *Phys. Rev. B*, 95:241304, Jun 2017.

[30] I. L. Aleiner and L. I. Glazman. Two-dimensional electron liquid in a weak magnetic field. *Phys. Rev. B*, 52:11296, Oct 1995.

[31] M. M. Fogler and B. I. Shklovskii. Collapse of spin splitting in the quantum hall effect. *Phys. Rev. B*, 52:17366, Dec 1995.

[32] T. Ando and Y. Uemura. Theory of quantum transport in a two-dimensional electron system under magnetic fields. i. characteristics of level broadening and transport under strong fields. *J. Phys. Soc. Jpn.*, 36:959, 1974.

[33] M. E. Raikh and T. V. Shahbazyan. High landau levels in a smooth random potential for two-dimensional electrons. *Phys. Rev. B*, 47:1522, 1993.

[34] T. P. Smith, B. B. Goldberg, P. J. Stiles, and M. Heiblum. Direct measurement of the density of states of a two-dimensional electron gas. *Phys. Rev. B*, 32:2696, Aug 1985.

[35] R.C. Ashoori and R.H. Silsbee. The landau level density of states as a function of fermi energy in the two dimensional electron gas. *Solid State Communications*, 81(10):821 – 825, 1992.

[36] J. P. Eisenstein, H. L. Stormer, V. Narayanamurti, A. Y. Cho, A. C. Gossard, and C. W. Tu. Density of states and de haas¯van alphen effect in two-dimensional electron systems. *Phys. Rev. Lett.*, 55:875, Aug 1985.

[37] Daw-Wei Wang, Eugene Demler, and S. Das Sarma. Spontaneous symmetry breaking and exotic quantum orders in integer quantum hall systems under a tilted magnetic field. *Phys. Rev. B*, 68:165303, Oct 2003.

[38] D. B. Chklovskii, B. I. Shklovskii, and L. I. Glazman. Electrostatics of edge channels. *Phys. Rev. B*, 46:4026, Aug 1992.

[39] V. J. Goldman, M. Shayegan, and D. C. Tsui. Evidence for the fractional quantum hall state at $\nu = \frac{1}{7}$. *Phys. Rev. Lett.*, 61:881, Aug 1988.

[40] R. L. Willett, H. L. Stormer, D. C. Tsui, L. N. Pfeiffer, K. W. West, and K. W. Baldwin. Termination of the series of fractional quantum hall states at small filling factors. *Phys. Rev. B*, 38:7881, Oct 1988.

[41] V. J. Goldman and B. Su. Resonant tunneling in the quantum hall regime: Measurement of fractional charge. *Science*, 267(5200):1010, 1995.

[42] R. de Picciotto, M. Reznikov, M. Heiblum, V. Umansky, G. Bunin, and D. Mahalu. Direct observation of a fractional charge. *Nature*, 389(6647):162–164, Sep 1997.

[43] L. Saminadayar, D. C. Glattli, Y. Jin, and B. Etienne. Observation of the $e/3$ fractionally charged laughlin quasiparticle. *Phys. Rev. Lett.*, 79:2526, Sep 1997.

[44] Jens Martin, Shahal Ilani, Basile Verdene, Jurgen Smet, Vladimir Umansky, Diana Mahalu, Dieter Schuh, Gerhard Abstreiter, and Amir Yacoby. Localization of fractionally charged quasi-particles. *Science*, 305(5686):980–983, 2004.

[45] R. L. Willett, M. A. Paalanen, R. R. Ruel, K. W. West, L. N. Pfeiffer, and D. J. Bishop. Anomalous sound propagation at ν=1/2 in a 2d electron gas: Observation of a spontaneously broken translational symmetry? *Phys. Rev. Lett.*, 65:112–115, Jul 1990.

[46] V. J. Goldman, B. Su, and J. K. Jain. Detection of composite fermions by magnetic focusing. *Phys. Rev. Lett.*, 72:2065, 1994.

[47] J. H. Smet, D. Weiss, R. H. Blick, G. Lütjering, K. von Klitzing, R. Fleischmann, R. Ketzmerick, T. Geisel, and G. Weimann. Magnetic focusing of composite fermions through arrays of cavities. *Phys. Rev. Lett.*, 77:2272, Sep 1996.

[48] R. L. Willett, R. R. Ruel, K.W. West, and L. N. Pfeiffer. Experimental demonstration of a fermi surface at one-half filling of the lowest landau level. *Phys. Rev. Lett.*, 71:3846, 1993.

[49] W. Kang, H. L. Stormer, L. N. Pfeiffer, K. W. Baldwin, and K. W. West. How real are composite fermions? *Phys. Rev. Lett.*, 71:3850, 1993.

[50] Dam Thanh Son. Is the composite fermion a dirac particle? *Phys. Rev. X*, 5:031027, Sep 2015.

[51] Wanli Li, D. R. Luhman, D. C. Tsui, L. N. Pfeiffer, and K. W. West. Observation of reentrant phases induced by short-range disorder in the lowest landau level of $\mathrm{al}_x\mathrm{ga}_{1-x}\mathrm{As}/\mathrm{al}_{0.32}\mathrm{ga}_{0.68}\mathrm{As}$ heterostructures. *Phys. Rev. Lett.*, 105:076803, Aug 2010.

[52] Rodney Price, Xuejun Zhu, S. Das Sarma, and P. M. Platzman. Laughlin-liquid˘wigner-solid transition at high density in wide quantum wells. *Phys. Rev. B*, 51:2017, Jan 1995.

[53] Yang Liu, C. G. Pappas, M. Shayegan, L. N. Pfeiffer, K. W. West, and K. W. Baldwin. Observation of reentrant integer quantum hall states in the lowest landau level. *Phys. Rev. Lett.*, 109:036801, Jul 2012.

[54] I. V. Kukushkin, S. V. Meshkov, and V. B. Timofeev. Two-dimensional electron density of states in a transverse magnetic field. *Phys. Usp.*, 31(6):511–534, 1988.

[55] Michael Seul and David Andelman. Domain shapes and patterns: The phenomenology of modulated phases. *Science*, 267(5197):476, 1995.

[56] M. M. Fogler and A. A. Koulakov. Laughlin liquid to charge-density-wave transition at high landau levels. *Phys. Rev. B*, 55:9326, Apr 1997.

[57] E. H. Rezayi, F. D. M. Haldane, and Kun Yang. Charge-density-wave ordering in half-filled high landau levels. *Phys. Rev. Lett.*, 83:1219, Aug 1999.

[58] F. D. M. Haldane, E. H. Rezayi, and Kun Yang. Spontaneous breakdown of translational symmetry in quantum hall systems: Crystalline order in high landau levels. *Phys. Rev. Lett.*, 85:5396, Dec 2000.

[59] Naokazu Shibata and Daijiro Yoshioka. Ground-state phase diagram of 2d electrons in a high landau level: A density-matrix renormalization group study. *Phys. Rev. Lett.*, 86:5755, Jun 2001.

[60] J. Zhu, W. Pan, H. L. Stormer, L. N. Pfeiffer, and K. W. West. Density-induced interchange of anisotropy axes at half-filled high landau levels. *Phys. Rev. Lett.*, 88:116803, Mar 2002.

[61] Yang Liu, D. Kamburov, M. Shayegan, L. N. Pfeiffer, K. W. West, and K. W. Baldwin. Spin and charge distribution symmetry dependence of stripe phases in two-dimensional electron systems confined to wide quantum wells. *Phys. Rev. B*, 87:075314, Feb 2013.

[62] J. Pollanen, K. B. Cooper, S. Brandsen, J. P. Eisenstein, L. N. Pfeiffer, and K. W. West. Heterostructure symmetry and the orientation of the quantum hall nematic phases. *Phys. Rev. B*, 92:115410, Sep 2015.

[63] Sunanda P. Koduvayur, Yuli Lyanda-Geller, Sergei Khlebnikov, Gabor Csathy, Michael J. Manfra, Loren N. Pfeiffer, Kenneth W. West, and Leonid P. Rokhinson. Effect of strain on stripe phases in the quantum hall regime. *Phys. Rev. Lett.*, 106:016804, Jan 2011.

[64] M. A. Mueed, Md. Shafayat Hossain, L. N. Pfeiffer, K. W. West, K. W. Baldwin, and M. Shayegan. Reorientation of the stripe phase of 2d electrons by a minute density modulation. *Phys. Rev. Lett.*, 117:076803, Aug 2016.

[65] R. M. Lewis, P. D. Ye, L. W. Engel, D. C. Tsui, L. N. Pfeiffer, and K. W. West. Microwave resonance of the bubble phases in 1/4 and 3/4 filled high landau levels. *Phys. Rev. Lett.*, 89:136804, 2002.

[66] R. M. Lewis, Y. Chen, L. W. Engel, D. C. Tsui, P. D. Ye, L. N. Pfeiffer, and K. W. West. Evidence of a first-order phase transition between wigner-crystal and bubble phases of 2d electrons in higher landau levels. *Phys. Rev. Lett.*, 93:176808, 2004.

[67] G. Sambandamurthy, R. M. Lewis, Han Zhu, Y. P. Chen, L. W. Engel, D. C. Tsui, L. N. Pfeiffer, and K. W. West. Observation of pinning mode of stripe phases of 2d systems in high landau levels. *Phys. Rev. Lett.*, 100:256801, Jun 2008.

[68] Han Zhu, G. Sambandamurthy, L. W. Engel, D. C. Tsui, L. N. Pfeiffer, and K. W. West. Pinning mode resonances of 2d electron stripe phases: Effect of an in-plane magnetic field. *Phys. Rev. Lett.*, 102:136804, Mar 2009.

[69] Benedikt Friess, Vladimir Umansky, Lars Tiemann, Klaus von Klitzing, and Jurgen H. Smet. Probing the microscopic structure of the stripe phase at filling factor 5/2. *Phys. Rev. Lett.*, 113:076803, Aug 2014.

[70] T. D. Rhone, L. Tiemann, and K. Muraki. Nmr probing of spin and charge order near odd-integer filling in the second landau level. *Phys. Rev. B*, 92:041301, Jul 2015.

[71] I. V. Kukushkin, V. Umansky, K. von Klitzing, and J. H. Smet. Collective modes and the periodicity of quantum hall stripes. *Phys. Rev. Lett.*, 106:206804, May 2011.

[72] B. Friess, Y. Peng, B. Rosenow, F. von Oppen, V. Umansky, K. von Klitzing, and J. H. Smet. Negative permittivity in bubble and stripe phases. *Nat Phys*, advance online publication, Jul 2017. Article.

[73] R. Willett, J. P. Eisenstein, H. L. Störmer, D. C. Tsui, A. C. Gossard, and J. H. English. Observation of an even-denominator quantum number in the fractional quantum hall effect. *Phys. Rev. Lett.*, 59:1776–1779, Oct 1987.

[74] N. Samkharadze, K. A. Schreiber, G. C. Gardner, M. J. Manfra, E. Fradkin, and G. A. Csathy. Observation of a transition from a topologically ordered to a spontaneously broken symmetry phase. *Nat. Phys.*, 12:191, 2016.

[75] J. P. Eisenstein, K. B. Cooper, L. N. Pfeiffer, and K. W. West. Insulating and fractional quantum hall states in the first excited landau level. *Phys. Rev. Lett.*, 88:076801, Jan 2002.

[76] Nianpei Deng, J. D. Watson, L. P. Rokhinson, M. J. Manfra, and G. A. Csáthy. Contrasting energy scales of reentrant integer quantum hall states. *Phys. Rev. B*, 86:201301, Nov 2012.

[77] M. Khodas and M. G. Vavilov. Effect of microwave radiation on the nonlinear resistivity of a two-dimensional electron gas at large filling factors. *Phys. Rev. B*, 78:245319, 2008.

[78] I. A. Dmitriev, M. G. Vavilov, I. L. Aleiner, A. D. Mirlin, and D. G. Polyakov. Theory of microwave-induced oscillations in the magnetoconductivity of a two-dimensional electron gas. *Phys. Rev. B*, 71:115316, 2005.

[79] W. Kohn. Cyclotron resonance and de haas-van alphen oscillations of an interacting electron gas. *Phys. Rev.*, 123:1242, 1961.

[80] S. A. Mikhailov. Microwave-induced magnetotransport phenomena in two-dimensional electron systems: Importance of electrodynamic effects. *Phys. Rev. B*, 70:165311, 2004.

[81] J. H. Smet, B. Gorshunov, C. Jiang, L. Pfeiffer, K. West, V. Umansky, M. Dressel, R. Meisels, F. Kuchar, and K. von Klitzing. Circular-polarization-dependent study of the microwave photoconductivity in a two-dimensional electron system. *Phys. Rev. Lett.*, 95:116804, 2005.

[82] T. Herrmann, I. A. Dmitriev, D. A. Kozlov, M. Schneider, B. Jentzsch, Z. D. Kvon, P. Olbrich, V. V. Bel'kov, A. Bayer, D. Schuh, D. Bougeard, T. Kuczmik, M. Oltscher, D. Weiss, and S. D. Ganichev. Analog of microwave-induced resistance oscillations induced in gaas heterostructures by terahertz radiation. *Phys. Rev. B*, 94:081301, Aug 2016.

[83] R. G. Mani, J. H. Smet, K. von Klitzing, V. Narayanamurti, W. B. Johnson, and V. Umansky. Zero-resistance states induced by electromagnetic-wave excitation in gaas/algaas heterostructures. *Nature (London)*, 420:646, 2002.

[84] M. A. Zudov, R. R. Du, L. N. Pfeiffer, and K. W. West. Evidence for a new dissipationless effect in 2d electronic transport. *Phys. Rev. Lett.*, 90:046807, 2003.

[85] C. L. Yang, M. A. Zudov, T. A. Knuuttila, R. R. Du, L. N. Pfeiffer, and K. W. West. Observation of microwave-induced zero-conductance state in corbino rings of a two-dimensional electron system. *Phys. Rev. Lett.*, 91:096803, 2003.

[86] S. I. Dorozhkin. Giant magnetoresistance oscillations caused by cyclotron resonance harmonics. *JETP Lett.*, 77:577, 2003.

[87] S. I. Dorozhkin, L. Pfeiffer, K. West, K. von Klitzing, and J. H. Smet. Random telegraph photosignals in a microwave-exposed two-dimensional electron system. *Nat. Phys.*, 7:336, 2011.

[88] S. I. Dorozhkin, V. Umansky, L. N. Pfeiffer, K. W. West, K. Baldwin, K. von Klitzing, and J. H. Smet. Random flips of electric field in microwave-induced states with spontaneously broken symmetry. *Phys. Rev. Lett.*, 114:176808, May 2015.

[89] A. V. Andreev, I. L. Aleiner, and A. J. Millis. Dynamical symmetry breaking as the origin of the zero-dc-resistance state in an ac-driven system. *Phys. Rev. Lett.*, 91:056803, 2003.

[90] A. Auerbach, I. Finkler, B. I. Halperin, and A. Yacoby. Steady states of a microwave-irradiated quantum-hall gas. *Phys. Rev. Lett.*, 94:196801, 2005.

[91] J. Alicea, L. Balents, M. P. A. Fisher, A. Paramekanti, and L. Radzihovsky. Transition to zero resistance in a two-dimensional electron gas driven with microwaves. *Phys. Rev. B*, 71:235322, 2005.

[92] I. A. Dmitriev, M. Khodas, A. D. Mirlin, and D. G. Polyakov. Emergence of domains and nonlinear transport in the zero-resistance state. *Phys. Rev. Lett.*, 111:206801, Nov 2013.

[93] Klaus von Klitzing. Metrology in 2019. *Nat Phys*, 13(2):198–198, Feb 2017. Measure for Measure.

[94] A Yacoby, H.F Hess, T.A Fulton, L.N Pfeiffer, and K.W West. Electrical imaging of the quantum hall state. *Solid State Communications*, 111(1):1 – 13, 1999.

[95] E. Ahlswede, P. Weitz, J. Weis, K. von Klitzing, and K. Eberl. Hall potential profiles in the quantum hall regime measured by a scanning force microscope. *Physica B: Condensed Matter*, 298(1):562 – 566, 2001. International Conference on High Magnetic Fields in Semiconductors.

[96] T. Sajoto, Y. P. Li, L. W. Engel, D. C. Tsui, and M. Shayegan. Hall resistance of the reentrant insulating phase around the 1/5 fractional quantum hall liquid. *Phys. Rev. Lett.*, 70:2321–2324, Apr 1993.

[97] A. H. MacDonald and Matthew P. A. Fisher. Quantum theory of quantum hall smectics. *Phys. Rev. B*, 61:5724–5733, Feb 2000.

[98] Felix von Oppen, Bertrand I. Halperin, and Ady Stern. Conductivity tensor of striped quantum hall phases. *Phys. Rev. Lett.*, 84:2937, Mar 2000.

[99] Michael M. Fogler. *Stripe and Bubble Phases in Quantum Hall Systems*, pages 98–138. Springer Berlin Heidelberg, Berlin, Heidelberg, 2001.

[100] Steven H. Simon. Comment on evidence for an anisotropic state of two-dimensional electrons in high landau levels. *Phys. Rev. Lett.*, 83:4223, Nov 1999.

[101] B. W. Alphenaar, P. L. McEuen, R. G. Wheeler, and R. N. Sacks. Selective equilibration among the current-carrying states in the quantum hall regime. *Phys. Rev. Lett.*, 64:677, Feb 1990.

[102] T. Jungwirth, A. H. MacDonald, L. Smrčka, and S. M. Girvin. Field-tilt anisotropy energy in quantum hall stripe states. *Phys. Rev. B*, 60:15574, Dec 1999.

[103] Tudor D. Stanescu, Ivar Martin, and Philip Phillips. Finite-temperature density instability at high landau level occupancy. *Phys. Rev. Lett.*, 84:1288, Feb 2000.

[104] K. B. Cooper, M. P. Lilly, J. P. Eisenstein, L. N. Pfeiffer, and K. W. West. Onset of anisotropic transport of two-dimensional electrons in high landau levels: Possible isotropic-to-nematic liquid-crystal phase transition. *Phys. Rev. B*, 65:241313, Jun 2002.

[105] J. D. Watson, G. A. Csáthy, and M. J. Manfra. Impact of heterostructure design on transport properties in the second landau level of *In Situ* back-gated two-dimensional electron gases. *Phys. Rev. Applied*, 3:064004, Jun 2015.

[106] K. B. Cooper, M. P. Lilly, J. P. Eisenstein, T. Jungwirth, L. N. Pfeiffer, and K. W. West. An investigation of orientational symmetry-breaking mechanisms in high landau levels. *Solid State Commun.*, 119:89, 2001.

[107] I. Sodemann and A. H. MacDonald. Theory of native orientational pinning in quantum hall nematics. *arXiv:1307.5489*, 2013.

[108] C. Wexler and Alan T. Dorsey. Disclination unbinding transition in quantum hall liquid crystals. *Phys. Rev. B*, 64:115312, Aug 2001.

[109] I. V. Kukushkin, J. H. Smet, D. Schuh, W. Wegscheider, and K. von Klitzing. Dispersion of the composite-fermion cyclotron-resonance mode. *Phys. Rev. Lett.*, 98:066403, 2007.

[110] J. Gores, G. Gamez, J. H. Smet, L. Pfeiffer, K. West, A. Yacoby, V. Umansky, and K. von Klitzing. Current-induced anisotropy and reordering of the electron liquid-crystal phases in a two-dimensional electron system. *Phys. Rev. Lett.*, 99:246402, 2007.

[111] N. Deng, A. Kumar, M. J. Manfra, L. N. Pfeiffer, K. W. West, and G. A. Csáthy. Collective nature of the reentrant integer quantum hall states in the second landau level. *Phys. Rev. Lett.*, 108:086803, Feb 2012.

[112] K. B. Cooper, J. P. Eisenstein, L. N. Pfeiffer, and K. W. West. Metastable resistance-anisotropy orientation of two-dimensional electrons in high landau levels. *Phys. Rev. Lett.*, 92:026806, Jan 2004.

[113] J. Eom, H. Cho, W. Kang, K. L. Campman, A. C. Gossard, M. Bichler, and W. Wegscheider. Quantum hall ferromagnetism in a two-dimensional electron system. *Science*, 289(5488):2320–2323, 2000.

[114] J. H. Smet, R. A. Deutschmann, W. Wegscheider, G. Abstreiter, and K. von Klitzing. Ising ferromagnetism and domain morphology in the fractional quantum hall regime. *Phys. Rev. Lett.*, 86:2412–2415, Mar 2001.

[115] Daniel G. Barci and Zochil González Arenas. Metastable anisotropy orientation of nematic quantum hall fluids. *Phys. Rev. B*, 78:085303, Aug 2008.

[116] E. W. Carlson, K. A. Dahmen, E. Fradkin, and S. A. Kivelson. Hysteresis and noise from electronic nematicity in high-temperature superconductors. *Phys. Rev. Lett.*, 96:097003, Mar 2006.

[117] Ekhard K.H. Salje and Karin A. Dahmen. Crackling noise in disordered materials. *Annual Review of Condensed Matter Physics*, 5(1):233–254, 2014.

[118] S. Basak and E. W. Carlson. Distinguishing xy from ising electron nematics. *Phys. Rev. B*, 96:081303, Aug 2017.

[119] J. A. Bonetti, D. S. Caplan, D. J. Van Harlingen, and M. B. Weissman. Electronic transport in underdoped $yba_2cu_3o_{7-\delta}$ nanowires: Evidence for fluctuating domain structures. *Phys. Rev. Lett.*, 93:087002, Aug 2004.

[120] I. A. Dmitriev, A. D. Mirlin, and D. G. Polyakov. Oscillatory ac conductivity and photoconductivity of a two-dimensional electron gas: Quasiclassical transport beyond the boltzmann equation. *Phys. Rev. B*, 70:165305, 2004.

[121] Y. M. Beltukov and M. I. Dyakonov. Microwave-induced resistance oscillations as a classical memory effect. *Phys. Rev. Lett.*, 116:176801, Apr 2016.

[122] V. A. Volkov and A. A. Zabolotnykh. Bernstein modes and giant microwave response of a two-dimensional electron system. *Phys. Rev. B*, 89:121410, Mar 2014.

[123] A. D. Chepelianskii and D. L. Shepelyansky. Microwave stabilization of edge transport and zero-resistance states. *Phys. Rev. B*, 80:241308, Dec 2009.

[124] S. A. Mikhailov. Theory of microwave-induced zero-resistance states in two-dimensional electron systems. *Phys. Rev. B*, 83:155303, Apr 2011.

[125] V. I. Ryzhii. Photoconductivity characteristics in thin films subjected to crossed electric and magnetic fields. *Sov. Phys. Solid State*, 11:2078, 1970.

[126] A. C. Durst, S. Sachdev, N. Read, and S. M. Girvin. Radiation-induced magnetoresistance oscillations in a 2d electron gas. *Phys. Rev. Lett.*, 91:086803, 2003.

[127] X. L. Lei and S. Y. Liu. Radiation-induced magnetoresistance oscillation in a two-dimensional electron gas in faraday geometry. *Phys. Rev. Lett.*, 91:226805, 2003.

[128] M. G. Vavilov and I. L. Aleiner. Magnetotransport in a two-dimensional electron gas at large filling factors. *Phys. Rev. B*, 69:035303, 2004.

[129] V. Ryzhii, A. Chaplik, and R. Suris. Absolute negative conductivity and zero-resistance states in two-dimensional electron systems: A plausible scenario. *JETP Lett.*, 80:363, 2004.

[130] I. A. Dmitriev, A. D. Mirlin, and D. G. Polyakov. Cyclotron-resonance harmonics in the ac response of a 2d electron gas with smooth disorder. *Phys. Rev. Lett.*, 91:226802, 2003.

[131] I. A. Dmitriev, M. Khodas, A. D. Mirlin, D. G. Polyakov, and M. G. Vavilov. Mechanisms of the microwave photoconductivity in two-dimensional electron systems with mixed disorder. *Phys. Rev. B*, 80:165327, 2009.

[132] A. T. Hatke, M. Khodas, M. A. Zudov, L. N. Pfeiffer, and K. W. West. Multiphoton microwave photoresistance in a high-mobility 2d electron gas. *Phys. Rev. B*, 84:241302(R), 2011.

[133] S. I. Dorozhkin. Quantum hall effect in a system with an electron reservoir. *JETP Lett.*, 103(8):513–517, 2016.

[134] V. Umansky and M. Heiblum. *Molecular Beam Epitaxy: From research to mass production*, chapter MBE growth of high-mobility 2DEG, pages 121–137. Elsevier Inc., 2013.

[135] M. A. Zudov. Period and phase of microwave-induced resistance oscillations and zero-resistance states in two-dimensional electron systems. *Phys. Rev. B*, 69:041304(R), 2004.

[136] M. A. Zudov, R. R. Du, L. N. Pfeiffer, and K. W. West. Multiphoton processes in microwave photoresistance of two-dimensional electron systems. *Phys. Rev. B*, 73:041303(R), 2006.

[137] S. I. Dorozhkin, J. H. Smet, K. von Klitzing, L. N. Pfeiffer, and K. W. West. Microwave induced magnetoresistance oscillations at the subharmonics of the cyclotron resonance. *JETP Lett.*, 86:543, 2007.

[138] I. V. Pechenezhskii, S. I. Dorozhkin, and I. A. Dmitriev. Fractional features in radiation-induced oscillations of the magnetoresistance of two-dimensional electron systems. *JETP Lett.*, 85:86, 2007.

[139] S. Wiedmann, G. M. Gusev, O. E. Raichev, A. K. Bakarov, and J. C. Portal. High-order fractional microwave-induced resistance oscillations in two-dimensional systems. *Phys. Rev. B*, 80:035317, 2009.

[140] X. L. Lei and S. Y. Liu. Multiple and virtual photon processes in radiation-induced magnetoresistance oscillations in two-dimensional electron systems. *Appl. Phys. Lett.*, 88:212109, 2006.

[141] I. A. Dmitriev, A. D. Mirlin, and D. G. Polyakov. Theory of fractional microwave-induced resistance oscillations. *Phys. Rev. Lett.*, 99:206805, 2007.

[142] M. Khodas, H. S. Chiang, A. T. Hatke, M. A. Zudov, M. G. Vavilov, L. N. Pfeiffer, and K. W. West. Nonlinear magnetoresistance oscillations in intensely irradiated two-dimensional electron systems induced by multiphoton processes. *Phys. Rev. Lett.*, 104:206801, 2010.

[143] P. K. Tien and J. P. Gordon. Multiphoton process observed in the interaction of microwave fields with the tunneling between superconductor films. *Phys. Rev.*, 129:647, Jan 1963.

[144] M. Moskalets and M. Buttiker. Adiabatic quantum pump in the presence of external ac voltages. *Phys. Rev. B*, 69:205316, 2004.

[145] M. G. Vavilov, I. L. Aleiner, and L. I. Glazman. Nonlinear resistivity of a two-dimensional electron gas in a magnetic field. *Phys. Rev. B*, 76:115331, 2007.

[146] I. A. Dmitriev, A. D. Mirlin, and D. G. Polyakov. Microwave photoconductivity of a two-dimensional electron gas: Mechanisms and their interplay at high radiation power. *Phys. Rev. B*, 75:245320, 2007.

[147] C. L. Yang, J. Zhang, R. R. Du, J. A. Simmons, and J. L. Reno. Zener tunneling between landau orbits in a high-mobility two-dimensional electron gas. *Phys. Rev. Lett.*, 89:076801, 2002.

[148] W. Zhang, H.-S. Chiang, M. A. Zudov, L. N. Pfeiffer, and K. W. West. Magneto-transport in a two-dimensional electron system in dc electric fields. *Phys. Rev. B*, 75:041304(R), 2007.

[149] W. Zhang, M. A. Zudov, L. N. Pfeiffer, and K. W. West. Resistance oscillations in two-dimensional electron systems induced by both ac and dc fields. *Phys. Rev. Lett.*, 98:106804, 2007.

[150] S. Wiedmann, G. M. Gusev, O. E. Raichev, A. K. Bakarov, and J. C. Portal. Nonlinear transport phenomena in a two-subband system. *Phys. Rev. B*, 84:165303, 2011.

[151] S. Chakraborty, A. T. Hatke, L. W. Engel, J. D. Watson, and M. J. Manfra. Multiphoton processes at cyclotron resonance subharmonics in a two-dimensional electron system under dc and microwave excitation. *Phys. Rev. B*, 90:195437, Nov 2014.

[152] E. Vasiliadou, G. Müller, D. Heitmann, D. Weiss, K. von Klitzing, H. Nickel, W. Schlapp, and R. Lösch. Collective response in the microwave photoconductivity of hall bar structures. *Phys. Rev. B*, 48:17145, 1993.

[153] S. Holland, C. Heyn, D. Heitmann, E. Batke, R. Hey, K. J. Friedland, and C.-M. Hu. Quantized dispersion of two-dimensional magnetoplasmons detected by photoconductivity spectroscopy. *Phys. Rev. Lett.*, 93:186804, 2004.

[154] I. V. Kukushkin, V. M. Muravev, J. H. Smet, M. Hauser, W. Dietsche, and K. von Klitzing. Collective excitations in two-dimensional electron stripes: Transport and optical detection of resonant microwave absorption. *Phys. Rev. B*, 73:113310, 2006.

[155] C. L. Yang, R. R. Du, L. N. Pfeiffer, and K. W. West. Influence of a parallel magnetic field on the microwave photoconductivity in a high-mobility two-dimensional electron system. *Phys. Rev. B*, 74:045315, 2006.

[156] S. I. Dorozhkin, A. A. Bykov, I. V. Pechenezhskii, and A. K. Bakarov. Coexistence of collective and single-particle effects in the photoresponse of a 2d electron gas to microwave radiation. *JETP Lett.*, 85:576, 2007.

[157] L.-C. Tung, C. L. Yang, D. Smirnov, L. N. Pfeiffer, K. W. West, R. R. Du, and Y.-J. Wang. Submillimeter wave induced resistance oscillations in ultra-high mobility two-dimensional electron systems. *Solid State Commun.*, 149:1531, 2009.

[158] I. V. Andreev, V. M. Muravev, I. V. Kukushkin, S. Schmult, and W. Dietsche. High-frequency response of a two-dimensional electron system under microwave irradiation. *Phys. Rev. B*, 83:121308(R), Mar 2011.

[159] A. T. Hatke, M. A. Zudov, J. D. Watson, and M. J. Manfra. Magnetoplasmon resonance in a two-dimensional electron system driven into a zero-resistance state. *Phys. Rev. B*, 85:121306(R), Mar 2012.

[160] A. T. Hatke, M. A. Zudov, J. D. Watson, M. J. Manfra, L. N. Pfeiffer, and K. W. West. Evidence for effective mass reduction in gaas/algaas quantum wells. *Phys. Rev. B*, 87:161307(R), Apr 2013.

[161] S. A. Studenikin, A. S. Sachrajda, J. A. Gupta, Z. R. Wasilewski, O. M. Fedorych, M. Byszewski, D. K. Maude, M. Potemski, M. Hilke, K. W. West, and L. N. Pfeiffer. Frequency quenching of microwave-induced resistance oscillations in a high-mobility two-dimensional electron gas. *Phys. Rev. B*, 76:165321, 2007.

[162] Frank Stern. Polarizability of a two-dimensional electron gas. *Phys. Rev. Lett.*, 18:546, Apr 1967.

[163] A. V. Chaplik. Possible crystallization of charge carriers in low-density inversion layers. *Sov. Phys. JETP*, 35:395, 1972.

[164] K. W. Chiu, T. K. Lee, and J. J. Quinn. *Surf. Sci.*, 58:182, 1976.

[165] S. A. Mikhailov. Radiative decay of collective excitations in an array of quantum dots. *Phys. Rev. B*, 54:10335–10338, Oct 1996.

[166] Qi Zhang, Takashi Arikawa, Eiji Kato, John L. Reno, Wei Pan, John D. Watson, Michael J. Manfra, Michael A. Zudov, Mikhail Tokman, Maria Erukhimova, Alexey Belyanin, and Junichiro Kono. Superradiant decay of cyclotron resonance of two-dimensional electron gases. *Phys. Rev. Lett.*, 113:047601, Jul 2014.

[167] Richard P. Leavitt and J. W. Little. Absorption and emission of radiation by plasmons in two-dimensional electron-gas disks. *Phys. Rev. B*, 34:2450, Aug 1986.

[168] V. M. Muravev, I. V. Andreev, S. I. Gubarev, V. N. Belyanin, and I. V. Kukushkin. Fine structure of cyclotron resonance in a two-dimensional electron system. *Phys. Rev. B*, 93:041110(R), Jan 2016.

[169] Q. Shi, P. D. Martin, A. T. Hatke, M. A. Zudov, J. D. Watson, G. C. Gardner, M. J. Manfra, L. N. Pfeiffer, and K. W. West. Shubnikov - de haas oscillations in a two-dimensional electron gas under subterahertz radiation. *Phys. Rev. B*, 92:081405(R), Aug 2015.

[170] I. V. Kukushkin, J. H. Smet, S. A. Mikhailov, D. V. Kulakovskii, K. von Klitzing, and W. Wegscheider. Observation of retardation effects in the spectrum of two-dimensional plasmons. *Phys. Rev. Lett.*, 90:156801, Apr 2003.

[171] I. Baskin, B. M. Ashkinadze, E. Cohen, and L. N. Pfeiffer. Imaging of magneto-plasmons excited in a two-dimensional electron gas. *Phys. Rev. B*, 84:041305, Jul 2011.

[172] S. A. Mikhailov and N. A. Savostianova. Microwave response of a two-dimensional electron stripe. *Phys. Rev. B*, 71:035320, 2005.

[173] I. V. Andreev, V. M. Muravev, V. N. Belyanin, and I. V. Kukushkin. Measurement of cyclotron resonance relaxation time in the two-dimensional electron system. *Appl. Phys. Lett.*, 105:202106, 2014.

[174] M. Bialek, M. Czapkiewicz, J. Wrobel, V. Umansky, and J. Lusakowski. Plasmon dispersions in high electron mobility terahertz detectors. *Appl. Phys. Lett.*, 104(26):–, 2014.

[175] V. E. Kozlov, A. B. Van'kov, S. I. Gubarev, I. V. Kukushkin, V. V. Solovyev, J. Falson, D. Maryenko, Y. Kozuka, A. Tsukazaki, M. Kawasaki, and J. H. Smet. Microwave magnetoplasma resonances of two-dimensional electrons in mgzno/zno heterojunctions. *Phys. Rev. B*, 91:085304(R), Feb 2015.

[176] V. M. Muravev, A. R. Khisameeva, V. N. Belyanin, I. V. Kukushkin, L. Tiemann, C. Reichl, W. Dietsche, and W. Wegscheider. Magnetoplasma excitations of two-dimensional anisotropic heavy fermions in alas quantum wells. *Phys. Rev. B*, 92:041303(R), Jul 2015.

Appendix A

Sample parameters

Table A.1: Samples used in this thesis

Name	Mobility ($\times 10^6$ cm^2/Vs)	Density ($\times 10^{11}$ cm^{-2})	Wafer name and source
A1	16	2.85	01-02-12.1 (Purdue)
A2	5	2.89	11-17-11.1 (Purdue)
A4	4.1	2.81	11-03-11.1 (Purdue)
A6	3.6	2.91	12-01-11.1 (Purdue)
A8	2.2	2.77	01-05-12.1 (Purdue)
A10	1.3	2.75	09-29-11.1 (Purdue)
N1	>30	3	01-27-15.2 (Purdue)
Z1	>30	3.1	07-20-00.1 (Princeton)
B1	>30	2.98	06-29-10.1 (Princeton)
H1	27	3.6	05-31-17.3 (Princeton)
H2	19	3.8	05-31-17.1 (Princeton)
B27-LHB	25	2.5	05-20-11.1 (Princeton)